Ph.D's Thesis

Meso-scale modelling of fluid dynamics in a colloidal system: Monte Carlo simulation and lattice Boltzmann method

Hae Won Seo

Department of Mechanical Engineering

Graduate School of UNIST

2019

Meso-scale modelling of fluid dynamics in a colloidal system: Monte Carlo Simulation and Lattice Boltzmann Method

Hae Won Seo

Department of Mechanical Engineering

Graduate School of UNIST

Meso-scale Modelling of Fluid Dynamics in a Colloidal System: Monte Carlo Simulation and Lattice Boltzmann Method

A thesis/dissertation
submitted to the Graduate School of UNIST
in partial fulfillment of the
requirements for the degree of
Doctor of Philosophy

Hae Won Seo

05. 21. 2019
Approved by

Advisor
Chun Sang Yoo

Meso-scale Modelling of Fluid Dynamics in a Colloidal System: Monte Carlo Simulation and Lattice Boltzmann Method

Hae Won Seo

This certifies that the thesis/dissertation of Hae Won Seo is approved.

05. 21. 2019

Advisor: Chun Sang Yoo

Sung Youb Kim

Taesung Kim

Jaesung Jang

Pilwon Kim

Abstract

Evaporation of a droplet induces an outward capillary flow, leaving a coffee-ring stain of colloidal particles at the droplet edge. This pattern can be altered by the addition of surfactant that induces Marangoni flows on the surface. To study deposition forming process in evaporating droplets, we develop a coarse-grained lattice gas model. The coupled dynamics between surfactant and droplet evaporation and the consequently oscillatory dynamics at the contact line are elucidated by performing Monte Carlo simulations. It is found that the coupled drop dynamics and the resulting final deposition patterns can be altered by adsorption kinetics. For slow adsorption rates, surfactant molecules are recirculated with the colloidal particles and the covered surface area by the surfactant grows from the contact line to the bulk of droplet as the initial concentration of the surfactant increases. This leaves coffee-ring patterns with wide rim areas upon evaporating or to multi-ring patterns depending on the surfactant concentration. For fast adsorption rates, a surfactant skin covers the entire surface area during the early phase of evaporation. This suppresses the coffee ring effect, and uniform patterns are obtained independent of surfactant concentration. The results suggest that the distribution of surfactant on the surface is critical in determining final deposition patterns and that understanding of the skin-forming process of the surfactant on the surface can help in manipulating the delicate pattern forming process of particles in evaporating drops.

The mechanism of the back and forth oscillatory dynamics of colloidal particles in a drying droplet containing surfactant is also investigated using a coarse grained lattice model. It is found that during the evaporation, aggregation and depletion zones of colloidal particles form close to the contact line, where the capillary and Marangoni flows are comparable in the opposite directions. These colloidal particle patterns are highly dependent on the contact angle, surfactant concentration, and evaporation rate. Under such evaporation conditions that particle aggregation occurs, surfactant is found to be accumulated in both contact line and aggregation zones, inducing two types of Marangoni

flows, called 'outer' and 'inner' Marangoni flows, respectively. The outer Marangoni flow is responsible for the oscillatory motions of colloidal particles by periodically changing its relative strength with time, while the inner Marangoni flow induces the swirling movement of colloidal particles from aggregation zone toward center of the droplet.

In the present Monte Carlo simulations, the velocity field inside the droplet is given from an analytic solution. To overcome this limitation, we propose a novel pseudo-potential lattice Boltzmann method to simultaneously simulate the internal flow of droplet together with colloidal particle distribution. The velocity field induced by evaporation is obtained by the pseudo-potential lattice Boltzmann method and the concentration of particles are modeled by the forced advection-diffusion lattice Boltzmann method. The deposition process of colloidal particles is described by the macroscopic fluid model rather than a particle-based method to reduce the computational cost. It is found that the new model, which combines the pseudo-potential LB model for evaporation of a droplet and the advection-diffusion LB model for colloids, describes well the evaporation of a droplet and the distribution of colloidal particles depending on the Peclet number.

The lattice Boltzmann method is a suitable method for simulating multi-phase flow. In general, the rate of evaporation is controlled by using the boundary conditions when simulating evaporation droplets. In this study, hence, open boundary conditions in LBM were previously studied. Based on the characteristic analysis, a two-dimensional(2D) characteristic boundary condition (CBC) is formulated for the Lattice Boltzmann method (LBM). This approach improves classical locally-one dimensional inviscid (LODI) relations by restoring multidimensional effects on flow at open boundaries. In this study, the two-dimensional characteristic boundary condition are extended to a general subsonic flow configuration in the LBM and the transverse effect become clear. From the test of vortex convection and vortex shedding problems, the improved CBC was found to be more accurate than the conventional CBC approach.

Contents

List of Figures

Chapter I

Introduction

1.1 Basic principles and theoretical background of droplet evaporation

Deposit patterns of particles in evaporating droplet on a substrate are commonly observed in daily life, which plays an crucial role in surface patterning techniques such as painting, coating and inkjet printing. In recent years, evaporation-inducing pattern formation has been applied to polymer printing and coating, micro / nano systems, electronic devices and sensors, drug delivery, biological information, and the like as a non-lithographic technique of nanoparticle assembly [1–7].

Droplet evaporation, including non-volatile materials, for instance colloidal particles, often leaves various deposit patterns associated with internal flow stress induced by evaporation and the characteristics of the involved materials. If the droplet contains a biological material, such as blood, the pattern may provide significant biological information. Therefore, droplet evaporation is one of the actively studied field. For instance, various methods for controlling droplet dynamics such as concentration, temperature, and relative humidity have been extensively discussed.

When a droplet evaporates on a substrate, coffee ring patterns at the pinned contact line is developed. Pattern formation induced by evaporation has been studied by Deegan *et al.* [8], who found the "coffee-ring" effect, which is the formation of ring-like deposit left

after the evaporation of a particle-laden liquid droplet. Since the evaporation is the fastest near the edge of the drying droplet, the solvent lost due to evaporation around should be replenished when the contact line is fixed; this leads to capillary flow of the droplets that transport the colloidal particles to the edge of the droplet resulting in ring-like stain. The coffee-ring pattern can be a multiple rings or regular patterns by a pinning and depinning sequences. However this does not always happen; for highly volatile solvents, the coffee ring effect has been reported to be reversible by the flow of thermal Marangoni flows [9].

A liquid with a high surface tension pulls a liquid around it that is stronger than a liquid with a low surface tension, so if there is a gradient of the surface tension, the liquid will flow out naturally at a region of low surface tension. These surface tension gradient can be caused by a temperature or concentration gradient. Many studies have been conducted on the deposition patterns resulting from the effect of the temperature induced Marangoni effect [10–13]. Consequently, it has been reported that the thermal conductivity of the substrate can change the direction of the Marangoni flow and corresponding the deposition pattern.

Marangoni flows can also develop inward by concentration gradients of the surfactant on the surface. These Marangoni flows typically leave uniform patterns after evaporation. Among recent experiments, Still *et al.* [14] reported that as the initial surfactant concentration increases, the deposit morphology dramatically changes to homogeneous patterns while the pinned contact line persists. Using biosurfactants, Sempels *et al.* [15] also observed the transition of coffee ring patterns to homogeneous deposition patterns. However, it is important to note the difference between flows developed due to the temperature and concentration gradients. The surfactant concentration field should be computed simultaneously with the flow velocity field because surfactant molecules are redistributed by the capillary flow in a drop during evaporation. In this case, the Marangoni flow is fully coupled to the surfactant concentration field. Due to this two-way coupling, recent studies reported more complex behavior of particles during evaporation prior to leaving homogeneous patterns on the substrate.

Therefore, in this study, we develop a new coarse-grained lattice model applicable to the Monte-Carlo method to describe the process of pattern formation of colloidal particles

when the surfactant is contained in the drying droplet. The details of mathematical formulation for this model and algorithm of Monte-Carlo method are described in Chapter II. Using this model, we can provide better understanding the dynamic competition of the capillary and Marangoni flows and corresponding process of deposition pattern.

In addition, we propose a method using the lattice Boltzmann method to simulate evaporative droplet with pinned contact line and conduct a study on the open boundary condition related to it. More information on this is provided in Chapter III and IV.

Finally, the main conclusions of the dissertation are summarized in Chapter V and additional challenging issues that need to be tackled as future work are discussed.

1.2 Monte-Carlo method for evaporation process of droplet simulation

Monte Carlo methods have been widely used to obtain equilibrium configurations of Ising-type lattice models. This models simplify the reality, and enables simulation of phase transitions. Ising model was first proposed by the Wilhelm Lenz [16], but later handed over to his disciple as a problem. The early one-dimensional Ising model was impossible conducting phase transition, but Ising himself solved in his paper [17]. The two-dimensional square lattice Ising model is much complicated, and eventually Lars Onsager provide an analytic description [18].

The lattice model is a simple energy model in which a Hamiltonian is defined in each configuration. The Monte Carlo method is used to calculate the energy of the equilibrium configuration by using random numbers to allow for configurational changes that can both increase and decrease the energy. Because of the randomness inherent in the model, Monte Carlo methods are often applied to systems where evolution depends on diffusion, adsorption or aggregation.

In general, Rabani's model [19] is widely used as a 2D Ising type lattice model for predicting the self-assembly of colloidal particles and dynamics of the evaporative droplet. Jung *et al.* simulated unstable deposition patterns of an evaporative droplet includ-

ing both evaporative convection and the Browian motion of weakly interacting particles within the model [20]. Zhang *et al.* conducted a modeling for the self-assembly nanoparticles into branched aggregates from a sessile nanofluid droplet in a circular domain. These two studies were performed by developing a Monte Carlo approach based on the 2D Ising model proposed by Rabani *et al.*

In this study, we begin by modeling the evaporation process in the model. Unlike the Rabani model in which the convective transport of particles is ignored, we investigate cases where particles of drying droplet are transported by convection, and in particular those containing adsorption kinetics in the case of surfactant. We use the evaporation induced velocity fields as obtained by Deegan *et al.*, and sorption kinetics from Langmuir's isotherm [21]. To simulate such cases, we modify the lattice model to include both the convection and ad/desorption.

1.3 Lattice Boltzmann method for evaporation process of droplet

Recently, lattice Boltzmann method has suggested as a powerful alternative computational fluid dynamics method for solving fluid flow problem and transport processes. The LBM is a mesoscopic method for the description of fluids. While it originated from the Cellular Automata models, it can also be considered as a discrete form of the Boltzmann's equation [22].

The pseudopotential LB model, which has been extensively applied to solve the multiphase flow problem for the last 20 years, was first developed by Shan and Chen [23]. The basic concept of this model is to consider the molecular interaction in micro-scale at the meso-scale using a pseudopotential. The pseudopotential is often represented as a effective mass that depends on local density. Such interaction below critical point allows a single component and a single fluid to spontaneously separate into two phases, high and low densities. This automatic phase separation no longer makes the phase interface as a mathematical boundary, which eliminates the need for interface tracking or capture

techniques. The advantage of pseudopotential model is that, despite its simplicity, it includes non-ideal equation of state and surface tension, which are essential component of multiphase flows [24–26]. Due to its superior computational efficiency and advantages of meso-scale, this model is accepted as a suitable method for simulating and investigating multiphase flows, especially for these flows with changing of the interface. Hence, it has been successfully applied to a wide range of field [25, 27]. Despite the numerical and theoretical studies for the multiphase flow in LBM community, a unified method within the LBM to predict the velocity field and the behaviors of drying droplet has not been actively studied.

In this study, hence, the simulation of evaporative droplet using pseudopotential is performed. In addition, we propose a method based on a pseudopotential model to simulate drying droplet containing colloidal particles, and to capture the corresponding behavior of colloidal particles in droplets. In Chapter III, the detailed formulation for the pseudopotential model and model for colloidal particles are described.

It is noted that the evaporation was considered through artificially outfluxing certain amount of mass at the open boundary rather than using a thermal LB model [28]. Appropriate open boundary conditions increase the reliability and stability of evaporative droplet simulations. In the lattice Boltzmann methods, most recent researches on the boundary conditions have focused on developing high-order boundary schemes for various configurations [29, 30], while little attention was paid on the treatment of spurious reflections at the open boundaries [31]. For instance, it was found from Izquierdo *et al.* [31] that solutions with commonly-used LBM boundary conditions suffer from artificial reflections at the open boundaries. To solve this problem, a study was performed to implement the conventional characteristic boundary conditions (CBC) to LBM [32] for spurious reflections. The result show better performance than those from the conventional LBM boundary condition. However, the previous study [32] is restricted to the 1-D case because the conventional CBC which is based on a local one-dimensional inviscid (LODI) assumption are restricted to being applied in the direction normal to the boundary. Improved characteristic boundary conditions were proposed to extend into multi dimensional flow, which are widely used to solve various counter flow problems in

CFD [33, 34].

In Chapter IV, we introduce the improved CBC to LBM community and to discuss the importance of the CBC in the LBM simulations. These implementation is validated by performing a comprehensive set of test problems, including vortex-convection and vortex shedding.

Chapter II

Surfactant effects on droplet dynamics and deposition patterns: a lattice gas model

2.1 Introduction

When a droplet evaporates on a substrate, a capillary flow toward its pinned contact line is developed to minimize the surface energy of the droplet [8]. Since Deegan et al. have first proposed the capillary flow as the main cause of the coffee-ring stains, numerous studies have been conducted for predicting and controlling the deposition patterns by effectively manipulating the evaporation-induced flows. For instance, the coffee ring pattern can be altered by Marangoni flows caused by either temperature or surfactant concentration [35–44]. Hu and Larson [8, 35, 36, 45] obtained a numerical solution of the evaporation-induced flow in the spherical cap droplet under the lubrication approximation. They first solved the velocity field in a droplet with the Marangoni flows induced by temperature gradients, and then, extended their solution by including the generalized Marangoni flows, for example, caused by surfactant gradients. Their models have been widely used to predict the deposition patterns of functional materials under the influence of Marangoni flows for various practical applications in printing and coating [1, 46–51]. Unlike the temperature induced Marangoni flows, however, the effects

of surfactant-induced Marangoni flows on the deposition patterns have rarely been investigated numerically. This is primarily attributed to the fact that the distribution of surfactant on the surface should be simultaneously computed with the velocity field to numerically obtain surfactant-induced Marangoni flows using the Hu and Larson's model and as such, it becomes more complicated to investigate the phenomena that involve the surfactant kinetics and the drying dynamics in a droplet at the same time.

The control of Marangoni flows is one of the common methods to remove the undesirable coffee-ring effect. Marangoni flows are usually generated on free surfaces where surface tension gradients are developed either by temperature or by concentration difference [35–44]. Temperature-induced Marangoni flows are developed during non-uniform evaporation due to evaporation cooling. The direction of the flow is from the relatively hot contact line region to the cooler central region depending on the relative conductivity of the substrate to the liquid [10–13, 52]. Hu and Larson numerically computed the temperature field on the free surface due to the latent heat of evaporation [35, 36]. In their computation, the temperature field is considered independent of the flows from the assumption that heat is transported by diffusion rather than convection. They showed that Marangoni flows are developed inward, resulting in uniform patterns. This phenomenon is called the Marangoni effect as opposed to the coffee ring effect. Xu et al. further obtained the coupled field of temperature and flow velocity using a combined field approach [38]. Huang et al. proposed the height-averaged velocity field and investigated the resulting deposition patterns in the presence of Marangoni flows [53].

Marangoni flows can also develop inward by concentration gradients of the surfactant on the surface because the surface concentration increases with radius due to the outward evaporation-induced convection. These Marangoni flows typically leave uniform patterns after evaporation. Among recent experiments, Still et al. reported that as the initial surfactant concentration increases, the deposit morphology dramatically changes to homogenous patterns while the pinned contact line persists [14]. Using bio-surfactants, Sempels et al. also observed the transition of coffee ring patterns to homogeneous deposition patterns [15]. However, it is important to note the difference between flows developed due to the temperature and concentration gradients. The surfactant concentration field should

be computed simultaneously with the flow velocity field because surfactant molecules are redistributed by the capillary flow in a drop during evaporation. In this case, the Marangoni flow is fully coupled to the surfactant concentration field. Due to this two-way coupling, recent studies reported more complex behavior of particles during evaporation prior to leaving homogeneous patterns on the substrate [54, 55]. For example, Still et al. first identified the temporal evolution of surfactant-induced Marangoni vortices due to the coupling effects [14]. Sempels et al. also observed Marangoni vortices and recurrent back and forth movements of colloidal particles before homogeneous deposition patterns are finally formed [15]. To adjust the role of the surface surfactant on the oscillatory motions of the particles, they controlled the amount of adsorbed bio-surfactant through the substrate temperature, which changes its solubility in the bulk [15].

In the presence of surfactant, the dynamics of colloidal particles dramatically change due to the coupling of the capillary flow and the surfactant-induced flow on the droplet surface. Interestingly, the surfactant concentration on the surface periodically changes: initially, the outward capillary flow transports surfactant molecules to the droplet edge, increasing the concentration in the bulk and subsequently on the surface via adsorption; then, Marangoni flows on the surface develop from the edge to the center, counteracting the capillary flow [9]; as a result, the surfactant concentration gradient decreases with the Marangoni flows, and hence, their strength vanishes as at the initial time. Since the directions of Marangoni flows are generally from the edge (high concentration) to the center (low concentration), a uniform pattern can be obtained in a drying droplet.

Although these results indicate the importance of sorption kinetics in the formation of the surface skin of the surfactant and thus in the manipulation of final deposition patterns, little attention has been paid to deposition formation with the coupling dynamics of the surfactant. This is likely due to the complexity of the problem, which involves the different time scales of the evaporation of a droplet and sorption kinetics of the surfactant, and the different length scales of surfactant molecules and colloidal particles [53, 56, 57]. To the best of our knowledge, there are few realistic simulation models to simultaneously describe deposition formation with the spatial variation of the surfactant at the free surface.

During the process, strong (weak) capillary flows induce strong (weak) Marangoni flows and vice versa due to the coupling effect, and this interplay of the flows induces time-dependent motions of colloidal particles close to the contact line. For instance, Still et al. first observed surfactant-induced Marangoni eddies that counteract the outward capillary flow, preventing the formation of a coffee ring at the contact line [14]. However, it has been reported that the particle dynamics can be more complex depending on the characteristics of surfactant. Sempels et al. observed experimentally time-dependent back-and-forth oscillations and vortices of E. coli bacteria in a drop containing surfactant [15]. They correlated the surfactant concentration and the strength of the inward Marangoni flows induced by bio-surfactant; when the surfactant concentration is low, the back-and-forth oscillatory motions first occur and then gradually change to the Marangoni eddies (swirling motions). A similar oscillatory movement of particles was observed together with particle aggregation by Carreon et al. [58]. However, the mechanisms of surfactant dynamics suggested by Still et al. cannot precisely explain the occurrence of such oscillatory dynamics of colloidal particles. Although the interplay between the capillary and Marangoni flows plays a critical role in determining the oscillatory dynamics of colloidal particles, only few studies have been conducted to investigate the dynamic competition between the two flows due to difficulties to obtain the temporal evolution of surfactant concentration on the surface.

In the present study, therefore, we develop a new coarse-grained lattice model to describe pattern forming processes of colloidal particles when a drying drop contains surfactant in section 2.3 [19, 59]. The sorption kinetics of surfactant to the interface is described by the Langmuir's isotherm, controlling the strength of Marangoni flows and the amount of transported surfactant to the surface. By performing Monte Carlo (MC) simulations of different particle transport processes governed by configurational Hamiltonians, the alternation of coffee-ring patterns to uniform or multi-ring coatings is investigated due to different Marangoni flows coupled with surfactant dynamics. We focus on the effects of the adsorption rates and the initial numbers of surfactant molecules on the final deposition patterns. Understanding the spatio-temporal evolution of the surfactant on the free surface will provide new insights into the dynamic processes of

pattern formation in a drying drop containing surfactant.

Furthermore, in section 2.4, we also investigate the time-dependent motions of colloidal particles in a drying droplet containing surfactant to better understand the dynamic competition of the capillary (Ca) and Marangoni flow (Ma) during evaporation. Specifically, we focus on the underlying mechanism to generate the back-and-forth oscillatory motions of colloidal particles. For this purpose, we simulate the intricate transport processes of surfactant both in a droplet and on its surface. To analyze the effect of flow pattern on the dynamics of colloidal particles, the relative strengths of Ma flow to Ca flow corresponding to surfactant concentration were computed. In addition, we find that the conditions under which unique patterns of colloidal particles are obtained are related to the contact angle and the concentration of surfactant. Finally, we describe the mechanism of the occurrence of the oscillations, which has not been explained precisely in previous studies.

2.2 Model

In this section, we introduce a two-dimensional coarse-grained lattice model that uses a Monte Carlo method to simulate particle behavior in a drying droplet containing surfactant. For simulations of this model, we assume that the evaporation of the droplet with surfactant occurs in a quasi-steady state at room temperature and the temperature difference along the surface by evaporative cooling is negligible [60]. To focus on surfactant dynamics [61, 62], we also assume that the contact line of the drop is pinned, and hence, there is no movement of the contact line along the radial direction [63–66]. One practical advantage of this assumption is that the effects of stick-slip motions or contact line movements that make the system more complicated to analyze can be separated out [8, 14, 41]. In general, the contact line can be pinned by chemical heterogeneities or surface roughness without the aid of ring deposits [45, 63–66]. Experimentally, a bank structure could be introduced for the pinned contact line as in ref. [41].

2.2.1 Langmuir's isotherm for sorption kinetics

The Langmuir's isotherm model is used to describe the adsorption-desorption kinetics between subsurface and surface such that the adsorption and desorption rates, η_{a} and η_{d}, are given by: [67]

$$\eta_{\mathrm{a}} = \omega_{\mathrm{a}}(\Gamma_{\infty} - \Gamma)c_s \exp(-E_{\mathrm{a}}/\bar{R}T), \tag{2.1}$$

$$\eta_{\mathrm{d}} = \omega_{\mathrm{d}}\Gamma \exp(-E_{\mathrm{d}}/\bar{R}T), \tag{2.2}$$

where ω_{a} and ω_{d} are pre-exponential factors, Γ is the surface coverage, Γ_{∞} is the maximum surface coverage, c_s is the subsurface concentration, and E_{a} and E_{d} are activation energies for adsorption and desorption.

The equation of the surface tension from the Langmuir's isotherm is given by: [21, 67, 68]

$$\sigma = \sigma_0 + \Gamma_{\infty}\bar{R}T\left[\ln\left(1 - \frac{\Gamma(c)}{\Gamma_{\infty}}\right)\right], \tag{2.3}$$

where σ_0 is the surface tension of pure solvent, $c = c(r, z, t)$ is the concentration of the surfactant.

2.2.2 Velocity field with non-zero Marangoni flow

In this study, we consider an axisymmetric droplet on a substrate, and as such, there exist only the radial and axial movements of particles and flows. Using the contact line radius, R_0, the contact angle, θ_0, and the maximum droplet height, h_0, the initial droplet shape is represented as a spherical cap. Moreover, when $\theta_0 \ll 1$, the droplet height, h, can be assumed to depend only on time, t, and radial position, r, and thus, it can be approximated by [69]:

$$h(r, t) \approx h_0(t_f - t)\left(1 - \left(\frac{r}{R_0}\right)^2\right), \tag{2.4}$$

where t_f denotes the final drying time. We wish to track both colloidal particles and surfactant particles in the cross-section owing to evaporative flow and Marangoni flow. In section 2.2.3 we discuss the coarse graining used to track both colloidal particle and surfactant simultaneously [61, 62]. Fig. 2.1 shows the cross section of a spherical cap shaped drop, where the $r-$ and $z-$axes represent its radial and axial directions, respectively.

During evaporation of a drop containing surfactant, Marangoni flows are developed due to the non-zero surface tension gradients. For description of the flow in a droplet, we adopt dimensionless velocity proposed by Hu and Larson [36]:

$$\begin{aligned}\tilde{u}_r =&\frac{3}{8}\frac{1}{1-\tilde{t}}\frac{1}{\tilde{r}}\left[(1-\tilde{r}^2)-(1-\tilde{r}^2)^{-\lambda(\theta)}\right]\left(\frac{\tilde{z}^2}{\tilde{h}^2}-2\frac{\tilde{z}}{\tilde{h}}\right)\\ &-\frac{g(R_0\tilde{r},t_f\tilde{t})t_f h_0\tilde{h}}{2R_0}\left(\frac{\tilde{z}}{\tilde{h}}-\frac{3}{2}\frac{\tilde{z}^2}{\tilde{h}^2}\right),\end{aligned} \tag{2.5}$$

$$\begin{aligned}\tilde{u}_z =&\frac{3}{4}\frac{1}{1-\tilde{t}}\left[1+\lambda(\theta)(1-\tilde{r}^2)^{-\lambda(\theta)-1}\right]\left(\frac{\tilde{z}^3}{3\tilde{h}^2}-\frac{\tilde{z}^2}{\tilde{h}}\right)\\ &+\frac{3}{2}\frac{1}{1-\tilde{t}}\left[(1-\tilde{r}^2)-(1-\tilde{r}^2)^{-\lambda^\theta}\right]\left(\frac{\tilde{z}^2}{2\tilde{h}^2}-\frac{\tilde{z}^3}{3\tilde{h}^3}\right)\tilde{h}(0,\tilde{t})\\ &+\frac{g(r,t)t_f h_0}{4\tilde{r}R_0}\left(\tilde{z}^2-\frac{\tilde{z}^3}{\tilde{h}}\right)+\frac{g'(r,t)t_f h_0}{4R_0}\left(\tilde{z}^2-\frac{\tilde{z}^3}{\tilde{h}}\right)\\ &-\frac{\tilde{r}g(r,t)t_f h_0\tilde{z}^3}{2R_0\tilde{h}^2}\tilde{h}(0,\tilde{t}),\end{aligned} \tag{2.6}$$

where the tilde represents dimensionless variables: $\tilde{t}=t/t_f, \tilde{r}=r/R_0$ and $\tilde{h}=h/h_0$. $\lambda(\theta)=\frac{1}{2}-\frac{\theta}{\pi}$ and $g'(r,t)$ is the derivative of $g(r,t)$ with respect to $\tilde{r}$. The equation for $g(r,t)$ is obtained from Hu and Larson [36]:

$$g(R_0\tilde{r},t_f\tilde{t})=-\frac{2h_0\tilde{r}}{t_f R_0}\left(1+J_0(\theta)\lambda(\theta)\left(1-\tilde{r}^2\right)^{-\lambda(\theta)-1}\right)+\frac{1}{\eta_m}\left.\frac{\mathrm{d}\sigma}{\mathrm{d}r}\right|_{z=h}, \tag{2.7}$$

where η_m is the solvent viscosity and $J_0(\theta)$ is the evaporation flux at the free surface of the droplet [70]. Note that the surface tension gradient can be produced either by the temperature gradient or by the surfactant concentration gradient at the free surfaces. When $\mathrm{d}\sigma/\mathrm{d}r = 0$, the Marangoni flow becomes zero and the velocity fields are simplified to the outward convective flows [36].

Here, we will only consider the surfactant-induced surface tension gradient. Through the second term in eqn (2.7), surfactant dynamics and the evaporation-induced flows are coupled. To compute $g(r,t)$, we introduce the nonlinear equation of the surface state for the surface tension s from the Langmuir's isotherm model [21]. The logarithmic function in eqn (2.3) implies that surface tension decreases with increasing surface concentration of the surfactant. Hence, substituting eqn (2.3) into eqn (2.7) yields:

$$g(R_0\tilde{r}, t_f\tilde{t}) = -\frac{2h_0\tilde{r}}{t_f R_0}\left(1 + J_0(\theta)\lambda(\theta)\left(1-\tilde{r}^2\right)^{-\lambda(\theta)-1}\right) - \frac{\Gamma_\infty \bar{R}T}{\eta_m}\left(\frac{\Gamma'}{\Gamma_\infty - \Gamma}\right), \tag{2.8}$$

$$\begin{aligned} g'(R_0\tilde{r}, t_f\tilde{t}) = &-\frac{4h_0\tilde{r}}{t_f R_0} J_0(\theta)\lambda(\theta)(1+\lambda(\theta))\left(1-\tilde{r}^2\right)^{-\lambda(\theta)-1} \\ &- \frac{\Gamma_\infty R_0 RT}{\eta_m}\left(\frac{\Gamma'^2 + (\Gamma_\infty - \Gamma)\Gamma''}{(\Gamma_\infty - \Gamma)^2}\right), \end{aligned} \tag{2.9}$$

where Γ' is the derivative of Γ with respect to r. It is important to note that the maximum concentration, c_{max}, that correspond to the value of Γ_{max} can be much higher than the critical micelle concentration in bulk, c_{cmc}. Although the surface tension is supposed to be constant in the regime well above c_{cmc}, surface flow changes are still observed [14,15]. This is because a hydrodynamic flow in a drying drop can push more particles into the surface much enough to accommodate particles large than those corresponding to c_{cmc}.

Since Γ is controlled by the flow field, $\vec{u}$, and *vice versa*, $\vec{u}$ must be calculated simultaneously with the surfactant distribution at each time step. This is a major difference from the studies carried out by Hu and Larson [9, 36], where Marangoni stresses are induced by temperature gradients, and the flow field and specified $-u$ are separated assuming heat diffusion rather than heat convection [9].

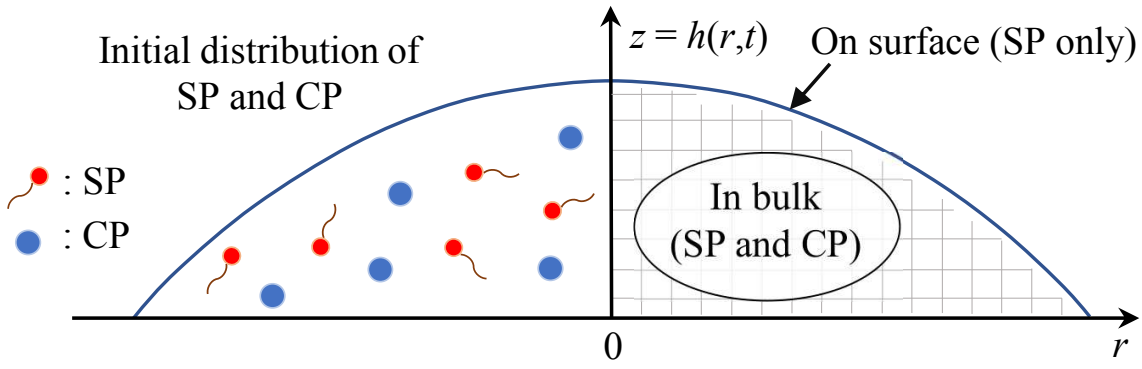

Figure 2.1: Schematic of initial distribution of colloidal and surfactant particles (CP and SP, respectively).

2.2.3 A coarse-grained lattice model

The coarse-grained lattice model adopted in this study uses a two-dimensional lattice for the cross-section of the droplet to assign the configurational energy, H_ν, to each cell that represents the movement of the particles in an evaporating solvent [20, 50]. The initial domain size is $R_0 \times h_0$ and the number of grids is $n_z \times n_r$ in the $rz-$plane. Cells on the lattice are indexed as (i, j) and at each i, the surface cell locates at $(i, j = si)$. During evaporation, the size of each cell, $\mathrm{d}r \times \mathrm{d}z$, is constant, buy the number of grids in the $z-$direction, s_i, vanishes with the droplet height. Fig. 2.1 shows a schematic of the cross section of a droplet and the initial distribution of particles.

Each cell is filled with two types of particles: colloidal particles(CP) and surfactant particles(SP). Here, we introduce a concept of a surfactant particle containing N_{pk} surfactant molecules to resolve difficulties caused by the significant disparity in the physical scales between surfactant molecules and colloidal particles in modeling [50]. In the present study, the radius of a single molecule of surfactant is assumed to be $R_m = 10^{-6}$ mm and that of colloid is $R_{CP} = 10^{-3}$ mm. By adopting the packed surfactant particles instead of surfactant molecules, we can simultaneously simulate the hydrodynamic movement of surfactant and colloidal particles in a coarse-grained lattice model. For this purpose, we choose N_{pk} of 10^9 as a unit number, which is equal to the ratio of a colloid to a surfactant molecule in volume.

This packing number is identical to that reported by Hu *et al.* [36] as an approximate minimum number of surfactant molecules on the surface of a water drop of 1 mm radius to overcome a radial surface flow. Then, the radius of a single surfactant particle consisting of 109 molecules falls into the same length scale of a lattice cell or a colloid. For example, when the radius of a single molecule of surfactant is approximately $R_m = 10^{-6}$ mm, the corresponding radius of a single surfactant particle (*i.e.*, one package of 10^9 molecules) becomes $R_{SP} = 10^{-3}$ mm, which is the same scale of CP considered in the present model. In addition, on the basis of the Stokes number for the present system ($<< 10^{-10}$), we can assume that both CP and SP are passive tracers of the flow. It represents the average surfactant concentration at the given length scale of a lattice cell [50].

The total number of CP and SP, N_{CP} and N_{SP}, are given by $N_{CP} = \sum n_{ij}$ and $N_{SP} = \sum m_{ij}$ where n_{ij} and m_{ij} are the number of CP and SP in each cell, respectively. These particles are convected along with evaporation-induced flows $\vec{u}(r,t)$. At the same time, SP can be transported through the adsorption kinetics occurring between the surface and subsurface. Since we allow only SP to be adsorbed to or desorbed from the surface cells, we set the number of CP on the surface to be always zero: $n_{ij} \equiv 0$ at $j = s_i$. Thus, the surface tension gradient that determines the Marangoni flows on the surface is produced only by the distribution of SP. Although we simulate the movements of CP and SP individually, the transport of CP cannot be described separately from the motion of SP. The distribution of CP and SP on a lattice defines one configurational state, $\nu = \{n_{ij}, m_{ij}|\vec{u}\}$.

Note that surfactant in the bulk can be transported to the subsurface layer through convection and diffusion prior to surface adsorption [71]. In a droplet with fast evaporation, however, surfactant is mainly transported to the subsurface by bulk convection [72]. We assume two different transport mechanisms of surfactant based on locations in a droplet [73–76]: (i) surfactant below the subsurface is transported only by the bulk convection, and (ii) surfactant between the subsurface and the free surface is transported both by the sorption kinetics and the bulk convection. In the present model the surfactant transport by convection in the bulk is defined by the capillary flow induced by evaporation.

2.2.4 Configurational Hamiltonian

To simulate the behavior of particles using a Monte Carlo method, we define the lattice gas model Hamiltonian as: [50]

$$H_\nu = -\sum_{i,j} q_{ij} m_{ij} - \sum_{i,j} f_{ij} m_{ij} - \sum_{i,j} f_{ij} n_{ij}, \tag{2.10}$$

where q_{ij} is the energy for the adsorption or desorption of surfactant, and f_{ij} is the energy due to the external velocity field $\overrightarrow{u}$. The amount of particles captured by the moving interface during evaporation is ignored for simplicity. We use Boltzmann probabilities for the sorption kinetics of surfactant. In other words, adsorption or desorption attempts are accepted with Metropolis probabilities as follows:

$$p_{\mathrm{a}} = \exp(-\Delta q_{\mathrm{a}}/\bar{R}T), \tag{2.11}$$

$$p_{\mathrm{d}} = \exp(-\Delta q_{\mathrm{d}}/\bar{R}T), \tag{2.12}$$

where the subscripts a and d represent adsorption and desorption, respectively, $\Delta q_{\mathrm{a,d}}$ are the energy changes due to sorption, and $\bar{R}T = N_{pk} k_B T$. The adsorption rate is proportional to the subsurface surfactant concentration, c_s, while the desorption rate to the surface coverage of surfactant, Γ. Therefore, $p_{\mathrm{a,d}}$ can be expressed in terms of $\eta_{\mathrm{a,d}}$, c_s, and Γ:

$$p_{\mathrm{a}} c_s \propto \eta_{\mathrm{a}}, \tag{2.13}$$

$$p_{\mathrm{d}} \Gamma \propto \eta_{\mathrm{d}}. \tag{2.14}$$

From eqn (2.1), (2.2), (2.13) and (2.14), we have:

$$-\Delta q_{\mathrm{a}}/\bar{R}T \propto \log((\omega_{\mathrm{a}}\Gamma_\infty)(1-\Gamma/\Gamma_\infty)) - E_{\mathrm{a}}/\bar{R}T, \tag{2.15}$$

$$-\Delta q_{\mathrm{d}}/\bar{R}T \propto \log(\omega_{\mathrm{d}}) - E_{\mathrm{d}}/\bar{R}T. \tag{2.16}$$

To adjust acceptance rate for simplicity, we take $E_{\mathrm{a}} = 0$ and $\omega = 1$. Also we set $E_{\mathrm{d}} = k_{\mathrm{d}}$ and $\omega_{\mathrm{a}}\Gamma_{\infty} = k_{\mathrm{a}}$. Since the adsorption and desorption are conduced by a random walk in the z-direction, eqn (2.15) and eqn (2.16) is obtained:

$$\Delta q_{\mathrm{a}} \propto -\bar{R}T \log\left(k_{\mathrm{a}}\left(1 - \frac{\Gamma}{\Gamma_{\infty}}\right)\right) \tag{2.17}$$

$$\Delta q_{\mathrm{d}} \propto k_{\mathrm{d}} \tag{2.18}$$

We discretize this result by pointing out that adsorption and desorption occur as a random walks in the z-direction: for adsorption,

$$q_{ij}^{+z} = -\bar{R}T \log\left(k_{\mathrm{a}}\left(1 - \frac{\Gamma_i}{\Gamma_{\infty}}\right)\right) I_j, \tag{2.19}$$

and for desorption,

$$q_{ij}^{-z} = k_{\mathrm{d}} I_j, \tag{2.20}$$

for all i. The superscripts $+z$ and $-z$ denote the direction of random walks, and Γ_i is the number surface coverage of SP at (i, s_i). I_j is a surface locator function defined by:

$$I_j = \begin{cases} 1, \text{ if } j = s_i, \\ \\ 0, \text{ if } j \neq s_i. \end{cases}$$

In the simulation, $k_{\mathrm{a}} = \exp(k_{\mathrm{d}}/\bar{R}T)$ is taken because the energy loss due to adsorption and the gain due to desorption are the same when $\Gamma_i = 0$. Therefore, k_{d} plays a critical role in determining the sorption process. [21] Since k_{d} is related to the desorption energy barrier, the value of k_{d} determines the probability that the surface SP remains on the surface: that is, high values of k_{d} indicate that desorption is limited and SP are likely to remain on the surface when it is on the surface. We assume that the surfactant does not have a time delay to overcome the adsorption barrier under the surface. It is noted that

the surfactant in the bulk can be transported to the subsurface layer *via* both convection and diffusion prior to its adsorption to the surface [71]. When the transport is dominated by diffusion, it takes time for the surfactant to accumulate well at the subsurface layer to overcome the adsorption energy barrier [71]. In a drying drop, however, the surfactant in the bulk is mainly transported to the subsurface by convection, which significantly reduces the adsorption delay of the surfactant to the surface compared to diffusion.

Based on the previous study, the energy f_{ij} accounts for a convection of particles in either axis direction [20]. For a movement in the r-direction, we compute

$$f_{ij}^{r} = 6\pi\eta_m R_p \sqrt{(a_0)_r} \sum_{k=i}^{i'} u_r(i,j), \tag{2.21}$$

where $(a_0)_r = (\mathrm{d}r)^2$; for a movement in the z-direction, we compute

$$f_{ij}^{z} = 6\pi\eta_m R_p \sqrt{(a_0)_z} \sum_{k=j}^{j'} u_z(i,j), \tag{2.22}$$

where $(a_0)_z = (\mathrm{d}z)^2$. Because it is assumed that the random walk always proceeds with a move in either the horizontal or vertical direction, each attempt of movement needs to compute either eqn.2.21 or eqn.2.22, but not both. That is, the convection of CP or SP on the entire lattice is simulated as the biased random walks due to the convection velocity by either u_r or u_z. In this way, particle movements in a flow $\vec{u}(r,t)$ will be captured by the effective potential f_{ij} in the framework of the lattice gas model. The field f_{ij} is obtained for a particle of radius R_p to resist the Stoke's flow of a solvent with prescribed velocity $u_x(x = r, z)$ and viscosity of the solvent η_m.

The Hamiltonian can be written as a notation for tiled dimensionless variables by non-dimensionalizing the variables with appropriate reference scales (using R_0, R_0/t_f, $\mathrm{d}z$, and $k_\mathrm{d}R_0$ for scales of length, velocity, lattice length and energy, respectively):

$$\begin{aligned} H_\nu = &- (6\pi\eta_m R_{\mathrm{CP}}(R_0/t_f)\mathrm{d}z)\sum \tilde{f}_{ij}n_{ij} \\ &- (6\pi\eta_m R_{\mathrm{SP}}(R_0/t_f)\mathrm{d}z)\sum \tilde{f}_{ij}m_{ij} - (k_{\mathrm{d}}R_0^2\Gamma_\infty dz)\sum \tilde{q}_{ij}m_{ij} \end{aligned} \tag{2.23}$$

H_ν can be written in a non-dimensional form by normalizing $6\pi\eta_m R_{\mathrm{SP}}(R_0/t_f)\mathrm{d}z$:

$$\tilde{H}_\nu = \left(\frac{R_{\mathrm{CP}}}{R_{\mathrm{SP}}}\right)\sum \tilde{f}_{ij}n_{ij} - \sum \tilde{f}_{ij}m_{ij} - \frac{1}{Q}\sum \tilde{q}_{ij}m_{ij} \tag{2.24}$$

where a dimensionless number, Q, is defined as the ratio of the characteristic values of the convection field to the sorption field,

$$Q = \frac{6\pi\eta_m R_{\mathrm{SP}}}{t_f k_{\mathrm{d}} R_0 \Gamma_\infty} \tag{2.25}$$

By implementing $\Gamma_\infty = \phi^S_{\max}/R^2_{\mathrm{SP}}$, Q can be rewritten as

$$Q = \frac{6\pi\eta_m R^3_{\mathrm{SP}}}{t_f k_{\mathrm{d}} R_0 \phi^S_{\max}} \tag{2.26}$$

where $\phi^S_{\max}$ is the maximum surfactant area fraction at the surface.

In this study, the effect of Q on the deposition pattern is investigated. Q indicates the competition between convective effect (where $f_{ij} \gg q_{ij}$) and sorption effect (where $q_{ij} \gg f_{ij}$) of SP to the surface. The ratio of R_{CP}/R_{SP} is constant for all simulations. Since $Q \sim k_{\mathrm{d}}^{-1}$, SP skin on surface is not formed when $Q = \infty$, and $Q \gg 1$ and $Q \ll 1$ correspond to relatively weak and relatively strong adsorption rates (of skin-formations) of SP, respectively. Thus, k_{d} and Q can be used interchangeably as the main parameter. For the value of k_{d}, we use a positive constant value associated with hydrophobicity of the surfactant (*i.e.* the tendency of the SP to remain adsorbed). In fact, desorption kinetics is rarely a research topic, and the value of k_{d} in experiment is used as one of the fitting parameters to determine dynamics surface tension [21].

It should be noted that in addition to Q, the initial number of SP, N_{SP}, can also affect the final deposition patterns because it influence potential energies through Γ_∞ and Γ_i

in the Hamiltonian (see eqn (2.10)). In fact, adsorption rates are proportional to the SP number concentration in the bulk, c. Therefore, the characteristics of the deposition process are explained by systematically changing both Q and N_{SP}. However, even at constant Q and N_{SP}, the increase of the surfactant number with evaporation also varies the values of the Hamiltonian through Γ_∞ due to the dynamic nature of the pattern formation process. Here, evaporation rates and Γ_∞ are fixed to constant in simulations and then change N_{SP} to investigate the effects of the initial surfactant number.

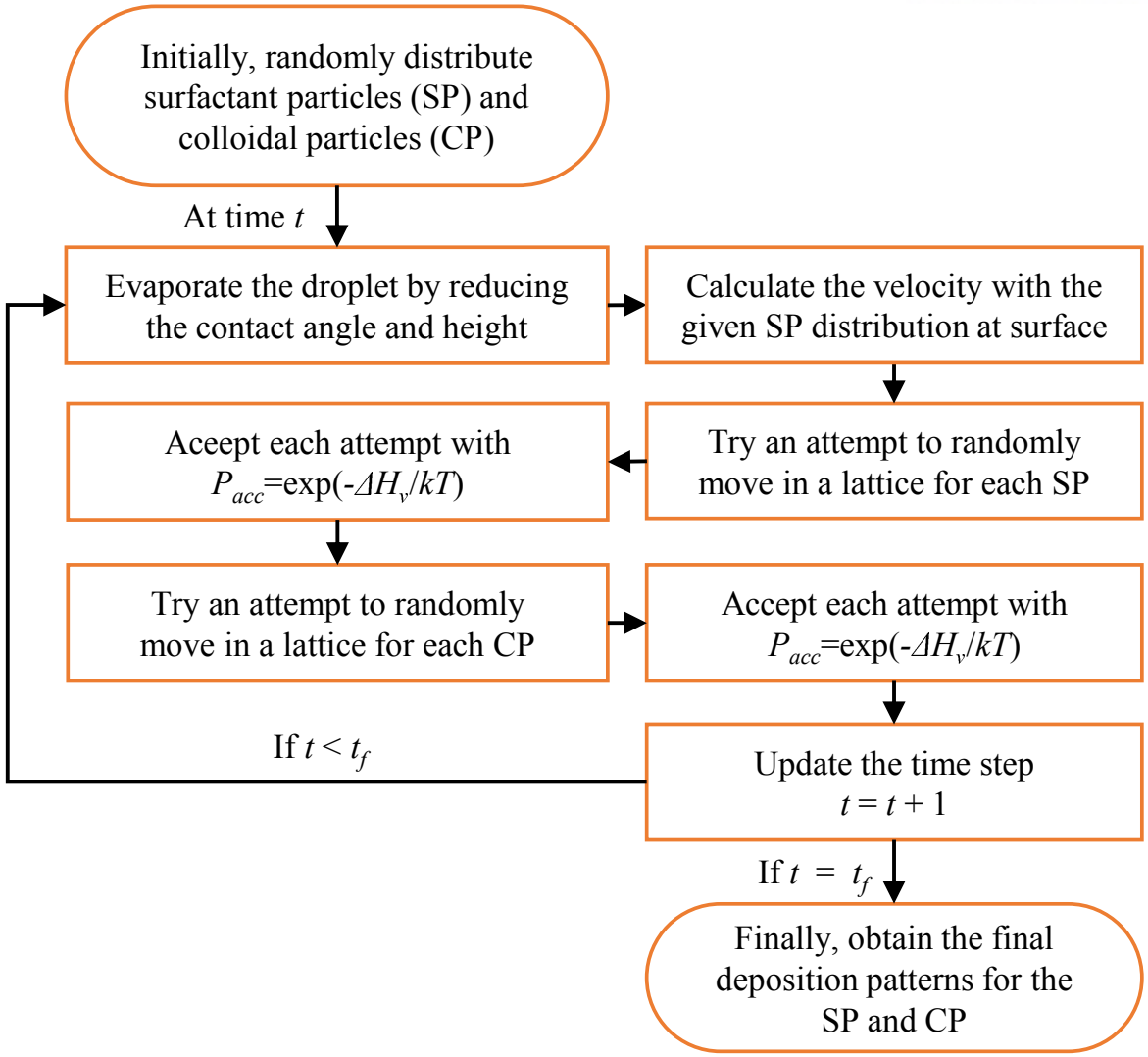

Figure 2.2: The algorithm of the Monte Carlo simulation.

2.2.5 Evolution by the Monte Carlo method

We introduce a Monte Carlo method to simulate the transport of CP and SP in an evaporating droplet. Briefly, the present method consists of three interrelated parts: (i) modeling the droplet evaporation in the context of the MC simulation, (ii) evolving configurations for both CP and SP using the coupled Hamiltonian in eqn (2.10), and (iii) describing the pattern forming process of colloidal particles as the flow pattern evolves. The algorithm of the MC simulation is presented in Fig. 2.2 [20].

First, we model the evaporation process for the MC method. The total drying time, t_f, is divided into m_c MC steps (MCS). At each MCS, we attempt N_{move} trials of SP

and CP movements using a MC procedure described below. For random walks in a drop, the drop height is prescribed at this time step and the velocity field is obtained from the previous time step. Upon the completion of each MC step, we "evaporate" the drop by decreasing the contact angle θ. According to the decrease of θ, the drop height, $h(r,t)$, is computed. Although θ can be computed directly from the mass loss of the drop by evaporation [20], we assume that θ decreases linearly with each MC step, which is the first-order solution for θ. The linear decrease of θ in time is consistent with the full drop dynamics when the initial contact angle is small enough [69]. At each MC step, therefore, we update the drop height, the corresponding cell numbers in the z-direction, and the solvent velocity. In addition, particles outside of the drop at a new MC step due to the decrease of drop height, are forced to move only downward to simulate the downward movement of particles pushed by the drop surface.

In principle, the evaporation rate can be controlled by varying either N_{move} or m_c, or by changing capillary flow velocity through the velocity scale R_0/t_f in eqn 2.23. Increasing N_{move} increases the number of attempts of particle motions in a given MC cycle; hence more particles move toward the contact line during the MCS, leading to an effective increase of the evaporation rate. On the other hand, increasing m_c increases the MC time to fully dry the drop, which effectively decreases the evaporation rate. In practice, we take $N_{\text{move,CP}} = N_{CP}$ and $N_{\text{move,SP}} = N_{SP}$ so that all particles have at least one chance to move during Δ. The MC dynamics at each MCS are as follows: since the distribution of SP affects the dynamics of CP, a single move of one SP is supposed to change the velocity field $\vec{u}$ and subsequently the moves of all CP. However, all individual SP move at the same time per MCS rather than sequentially. Therefore, we do not update the flow $\vec{u}$ until all SP have a chance to move based on H_ν; then, the dynamics of all CP is computed by using the updated velocity $\vec{u}$ at the MC step. Since the velocity $\vec{u}$ is not affected by the concentration of CP, moves of CP mimic the simple tracers of the velocity flow and the dynamics evolve only via convection. In the absence of SP, the process of CP self-assembly is related to classical coffee ring effects due to the decoupling between the convection of CP and the flow field. Our model should reflect this basic phenomenon.

The dynamics of our model is stochastic both for convection of CP and SP and

for sorption of SP. Initially, the lattice cells except on the surface are randomly filled with CP and SP (Fig. 2.1). The evolution of the configurations computed by Monte Carlo dynamics: the random walk of each particle is conducted in either the horizontal or vertical direction (see Fig. 2.2). During each cycle, the total number of particles is conserved. We attempt to move a randomly-chosen particle at a cell (i, j) to the nearest neighbor (i', j'), resulting in $A_{ij} \to A_{ij} - 1$ and $A_{i'j'} \to A_{i'j'} + 1$, where A_{ij} is either n_{ij} or m_{ij}. In particular, SP random walks on the surface may be attempted into the nearest neighbors on the surface: a randomly-chosen particle at a surface cell $(i, j = s_i)$ attempts a move to a nearest neighbor $(i', j' = s_{i'})$ on the surface, resulting in $M_i \to M_i - 1$ and $M'_i \to M'_i + 1$. These attempts are accepted with Metropolis criteria with a Boltzmann probability, $p_{acc} = \exp(-\Delta H_\nu / k\mathrm{B}T)$, where ΔH_ν is the resulting change in Hamiltonian in eqn (2.10).

Finally, the deposition of CP or SP is modeled by introducing a maximum number of particles that can be filled in a cell (i, j):

$$n_{\max} = \text{the integer rounded down from} \left(\phi^{\mathrm{b}}_{\max} \frac{V_{ij}}{V_{\mathrm{P}}} \right), \tag{2.27}$$

where $0 \leq \phi^{\mathrm{b}}_{\max} \leq 1$ is the given maximum volume fraction of CP or SP, the volume of a particle is $V_{\mathrm{P}} = 4\pi R^3{}_{\mathrm{P}}/3$, and R_{P} is the radius of the particle, CP or SP. The volume of a cell at (i, j) is $V_{ij} = \mathrm{d}r^2\mathrm{d}z$ and $\mathrm{d}z$ are the unit lengths of a lattice cell. The deposition phase of a cell (i, j) is defined when $n_{ij} > n_{\max}$. Hence, no MC move may put more CP or SP into the cells above the deposition phases. As discussed above, we also limit the number of SP on the surface by the maximum value to simulate different adsorption characteristics of the surfactant:

$$M_{\max} = \text{the integer rounded down from} \left(\phi^{\mathrm{s}}_{\max} \frac{A_{sj}}{A_{\mathrm{SP}}} \right), \tag{2.28}$$

where $0 \leq \phi^{\mathrm{s}}_{\max} \leq 1$ is the maximum surface area fraction of SP, A_{s_i}, is the surface area at a cell (i, s_i), $A_{\mathrm{SP}} = \pi R^2_{\mathrm{SP}}$, and R_{SP} is the radius of SP. We assume that in the model the surface area A_{s_i} depends only on the contact angle, making it constant with

radius but decreasing with time. Then the maximum number concentration of SP on the surface, Γ_∞, used in eqn (2.3), becomes

$$\Gamma_\infty = \frac{M_{\max}}{A_{s_i}} = \frac{\phi^{\mathrm{s}}_{\max}}{A_{\mathrm{SP}}} \tag{2.29}$$

2.3 Surfactant effects on droplet dynamics and deposition patterns

The evolution of colloidal and surfactant particles in an evaporating drop is simulated by using the configurational Hamiltonian and the MC method as described above. In the simulations, we assume that the contact line is pinned during evaporation. We also fix the evaporation rate for all simulations. Note that the velocity field induced by the coffee ring effect is inversely proportional to the drop height ($u \sim 1/h$) and therefore it increases during evaporation and becomes strongest at the final stage of evaporation (so-called "rush-hour" effects) [60, 77, 78].

The following physical parameters are fixed for MC simulations in sec.2.3: the initial contact angle is $y\theta = 0.698$ and the contact line is pinned at $R_0 = 1$ mm during the entire drying time of $t_f = 360s$. The initial numbers of cells are $n_r = 200$ for the radius and $n_z = 72$ for the height. The radii of CP and SP are given as $R_{\mathrm{CP}} = R_{\mathrm{SP}} = 10^{-3}$mm. The number of CP is $N_{\mathrm{CP}} = 500$ and the number of SP varies from N_{SP}=100 to 800. In addition, $\phi^{\mathrm{b}}_{\mathrm{max}} = 0.7, \phi^{\mathrm{s}}_{\mathrm{max}} = 0.9$, and MCS = 5000 are used. The number of SP, $N_{\mathrm{SP}} =$ 250, accords with the typical order of the molar concentration reported in experiments, which is approximately 1mM [14, 15, 41]. The total MC steps of MCS=5000 for the total drying time roughly correspond to the characteristic value of evaporation induced velocity, which is approximately $10\,\mu\mathrm{m}s^{-1}$. Table II.1 summarizes the simulation parameters.

We first show that the addition of surfactant to the drop induces different Marangoni flows, altering the final deposition patterns. In particular, we can change the surfactant distribution on the surface by varying the initial SP number (Cases A–E) and the adsorption rates (Cases 2–3). Case 1 without surfactant is also included to compare to other cases. All simulation results are provided in full cross-sectional views and/or in full top views. In particular, in the side views, the left and right half sides represent the distributions of SP and CP, respectively, while the top views are snapshots of CP only.

Case	N_{SP}	N_{CP}	k_d	Q
1	0	500	-	-
2	250	500	10^{-22}	2×10^5
3	250	500	10^{-10}	2×10^{-7}
A	100	500	10^{-22}	2×10^5
B	Case 2 reused			
C	350	500	10^{-22}	2×10^5
D	450	500	10^{-22}	2×10^5
E	800	500	10^{-22}	2×10^5

Table II.1: Physical parameters of Cases 1-3 and Cases A-E

2.3.1 Effects of surfactant on dried patterns

The effect of the parameter Q on the deposited patterns is studied through the simulations with and without surfactant. Fig. 2.3 demonstrates the deposition patterns of CP without surfactant (Case 1) and with weak (Case 2, $Q = 2\times10^5$) and strong (Case 3, $Q = 2\times10^7$) adsorption rates. Fig. 2.3(a) shows a typical ring-shaped deposition pattern (the ring in blue at the contact line in the top view and bars in black in the side view), ensuring the capability of the present model to reproduce coffee-ring patterns without surfactant. In Fig. 2.3(b) and (c), as expected, the addition of surfactant to the drop induces more distributed particles inside the domain. At the high adsorption rate, the outer ring becomes thinner and the inner particles are more distributed. These uniform distributions owing to the surfactant addition have been observed in many previous studies [14,15,41].

The effects of N_{SP} on the final CP deposition patterns are also investigated. Fig. 2.4 shows the final deposition patterns of CP and the radial CP distribution profiles with different N_{SP} from 100 to 800. Note that the result of Case 2 is duplicated by Case B. As N_{SP} increases, the width of the outer ring increases (from Case A to B), after which multi-rings develop (for Cases C–E). The final multi-ring pattern is quite different from the more uniformly-distributed pattern of Case 3 shown in Fig. 2.3(c). This distinction

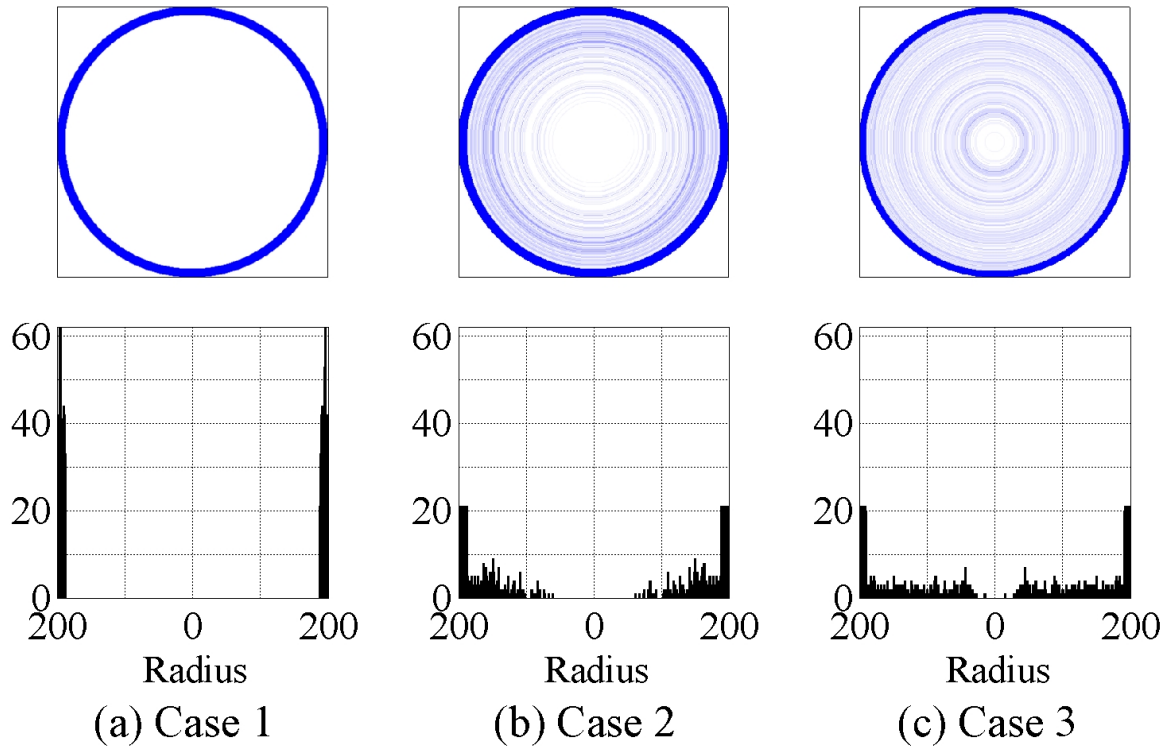

Figure 2.3: Top view of final CP deposition (top) and its corresponding particle-number distribution profile along the r-direction (bottom) for (a) Case 1 with $N_{\mathrm{SP}} = 0$, (b) Case 2 with $N_{\mathrm{SP}} = 250$ & $Q = 2 \times 10^{5}$, and (c) Case 3 with $N_{\mathrm{SP}} = 250$ & $Q = 2 \times 10^{-7}$.

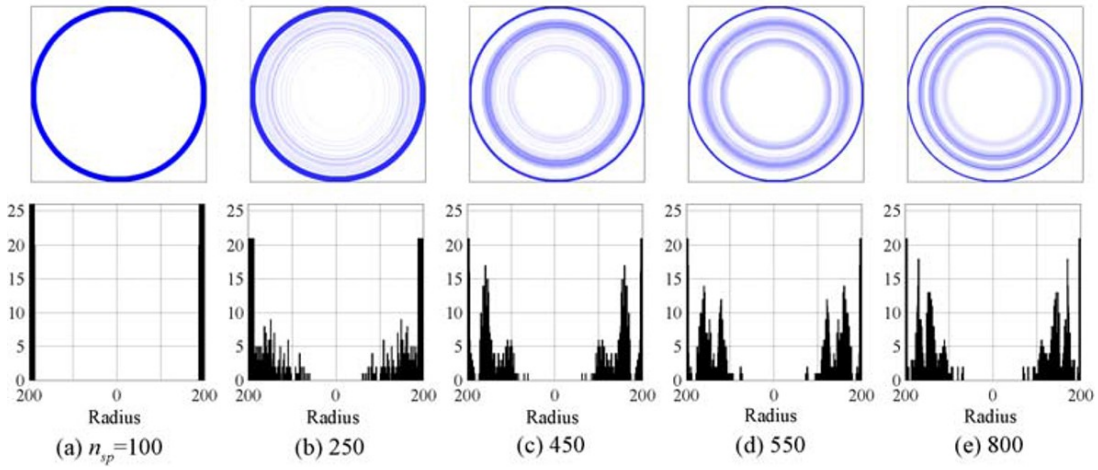

Figure 2.4: Top view of final CP deposition (top) and its corresponding particle-number distribution profile along the r-direction (bottom) for (a) Case A with $N_{\mathrm{SP}} = 100$, (b) Case B with $N_{\mathrm{SP}} = 250$, (c) Case C with $N_{\mathrm{SP}} = 450$, (d) Case D with $N_{\mathrm{SP}} = 550$, and (e) Case E with $N_{\mathrm{SP}} = 800$.

indicates the different roles of N_{SP} and Q in the surfactant dynamics even though both large N_{SP} and small Q strengthen the Marangoni flows, as will be discussed in the next section. It is also observed that the central regions of the depositions are empty of CP in Cases B–E, which is primarily attributed to enhanced outward convection during the final stage of evaporation. A similar rush-hour effect was reported in experiments by Marin *et al.* [55], where particles are always dragged toward the contact line due to mass conservation at the last stages of evaporation. The details of the effect are discussed in the following section.

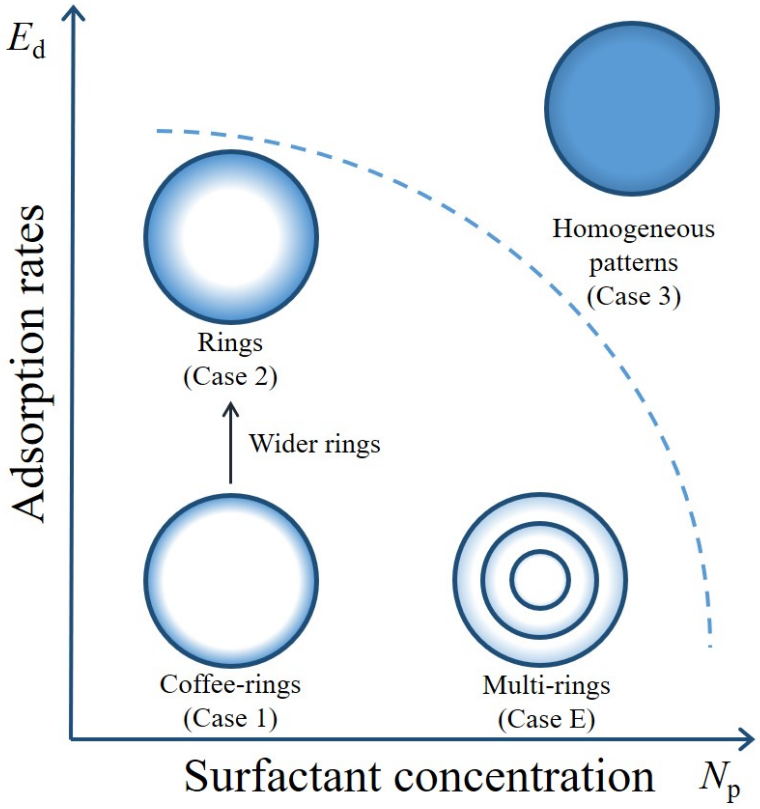

Figure 2.5: Schematic regime map for the dried patterns varying the initial surfactant number and the adsorption rate.

2.3.2 Effects of surfactant on flow patterns

In this section, we further investigate how different SP can change the temporal evolution of CP before the CP deposition patterns are formed on the substrate. Fig. 2.5 shows a summary of the different deposition patterns presented in Fig. 2.3 and 2.4 as functions of the initial number concentration and the adsorption rate of SP. Although Marangoni flows are enhanced by both increasing the initial number concentration of SP and the adsorption rate, the distribution of SP on the surface and thus the flows induced by these two features may be quite different, consequently leading to different pattern forming processes. We consider these differences in more detail below.

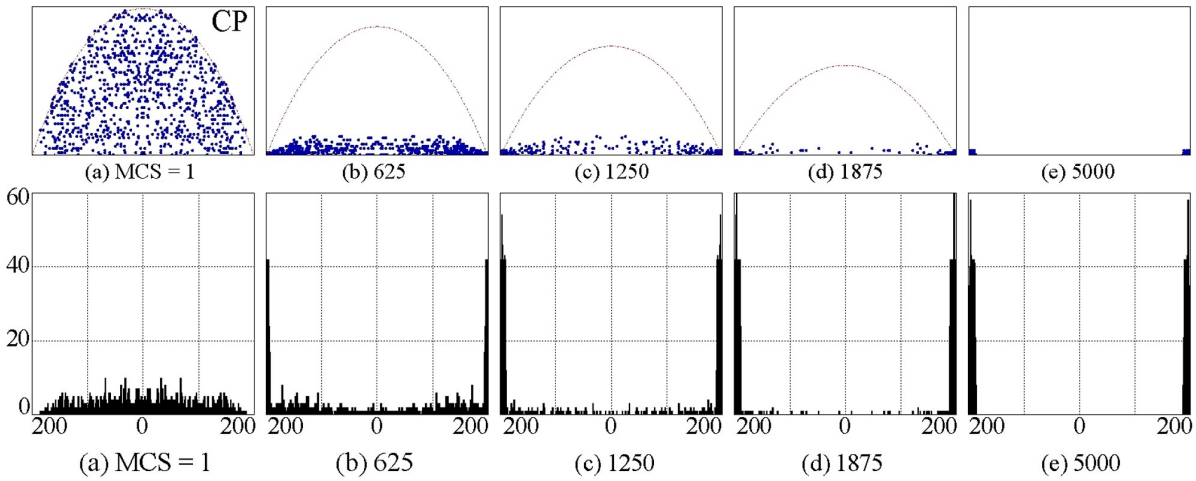

Figure 2.6: Temporal evolution of the colloidal particle distribution in the $r - z$ plane (top) and its radial profile (bottom) for Case 1 with $N_{\mathrm{SP}} = 0$ at different MCS: from left to right, (a)MCS=1, (b)625, (c)1250, (d)1875, and (e)5000. The (red) dash-dot lines in the top panels represent the drop surfaces. At the final stage of evaporation (e), the height of a drop is zero.

2.3.2.1 Surfactant addition: coffee-rings with wider rims.

Without surfactant, the common coffee-ring pattern is observed, as in Case 1 shown in Fig. 2.3(a). During the early stages of evaporation (Fig. 2.6(b) and (c)), particles near the contact line are deposited in a ring-shaped pattern, while particles near the center move gradually toward the contact line through convection (Fig. 2.6(c)–(e)). The number of particles deposited at the contact line increases until all particles are swept toward the contact line, and finally they merge with the ring at the edge. During evaporation, the drop height gradually decreases and the colloidal particles accordingly move downward to the substrate as well as outward to the contact line. This behavior is further illustrated in Fig. 2.7 by the pathlines of three representative colloidal particles, which agrees well with the flow patterns observed in the experiments in a drying drop [52].

Next, we investigate how the addition of surfactant to the drop changes the dynamics of SP and CP prior to the formation of the homogeneous patterns, as in Case 2 with $N_{\mathrm{SP}} = 250$ and $Q = 2 \times 10^5$ shown in Fig. 2.3(b) and 2.5. As shown in Fig. 2.8, CP now follow the dynamics of SP except on the surface layer where only SP are allowed

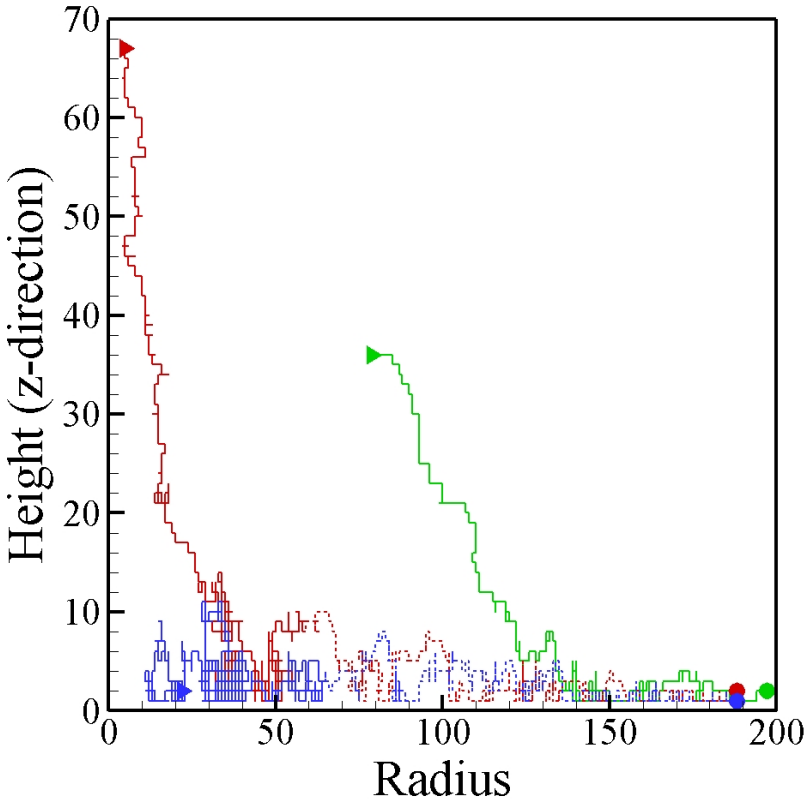

Figure 2.7: Traces of three representative particles in Case 1. Solid and dashed lines represent their movements during the first and second half times, respectively

to transport. During the time regimes shown in Fig. 2.8(d) and (e) (side views), the arch-shaped distribution of SP and CP suggests that there is a stratification of dominant flows in the z-direction. Two cavities without particles are formed: one is near the surface where the inward Marangoni flow is developed due to the SP adsorbed to the surface; and the other near the substrate where the outward coffee-ring flow is developed and the surface effect is minimal. The cavities near the surface and the substrate are gradually reduced and filled with SP toward the final stage of evaporation, thereby increasing the transport rates of surfactant to the surface.

Even at fixed Q and N_{SP}, the most frequent adsorption locations change with time, making the skin-forming process complicated. During the early stage of evaporation (Fig. 2.8(a)–(c) in side views), the adsorption of SP mainly occurs at the contact line where the SP number concentration increases with the coffee ring effect. However, it takes time for the particles adsorbed at the contact line to fully develop an inward Marangoni flow. Due to the Marangoni flow, the adsorbed SP recirculate along the surface toward the center and generate a skin layer of SP growing from the contact line (Fig. 2.8(c)). During the intermediate stages of evaporation (Fig. 2.8(c)–(f) in side views), the main adsorption locations move inward where particles aggregate due to the balance of the outward coffee-ring effect and the enhanced inward Marangoni effect. Finally, adsorption occurs over the entire domain (Fig. 2.8(g) and (h) in side views) as the overall number concentration of SP increases with evaporation.

The dynamics of CP shows unique oscillatory motions at the contact line due to the coupling between the surfactant and droplet dynamics. To analyze the coupled dynamics, we divide the evolution of Fig. 2.8(a)–(h) (in top views) into several time regimes during which either Marangoni or coffee-ring effect flow is in turn dominant. In detail, (a) and (b) is a coffee-ring-effect dominant (CRED) regime during which CP move toward the edge, resulting in the growth of the coffee ring. (c) is a Marangoni-effect-dominant (MED) regime (primarily at the edge) during which CP move inward, first broadening the width of the coffee ring at the contact line and then pushing the particles toward the center without leaving particles at the contact line. (d) is a CRED regime during which the outer coffee ring is reformed. In this time, however, the growth rate of the ring is reduced

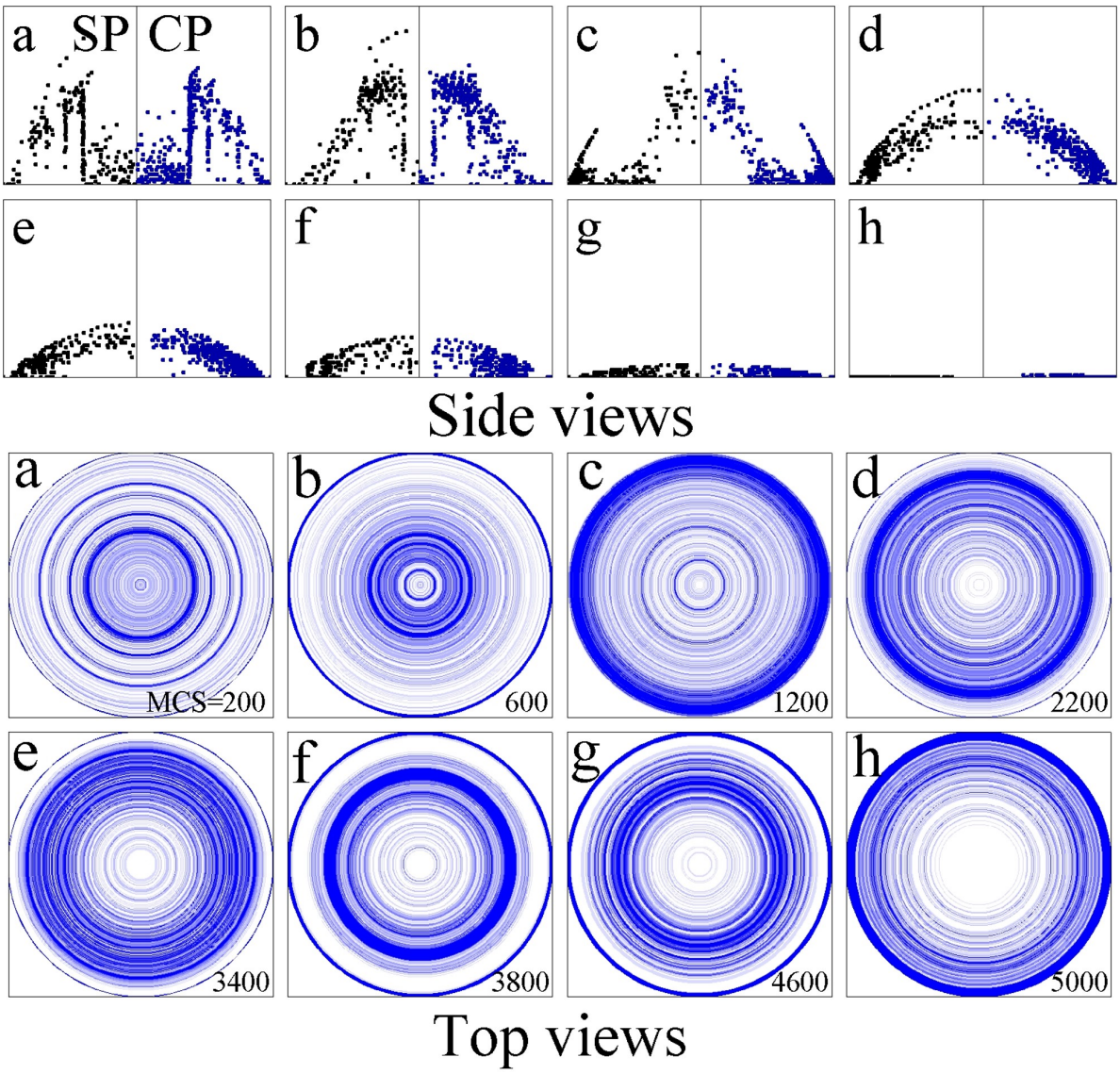

Figure 2.8: Temporal evolution of Sp and CP for Case 2 with $N_{\mathrm{SP}} = 250$ and $Q = 2 \times 10^5$ from (a) MCS=200 to (h) MCS=5000 with even intervals. The side views include both SP (left) and CP (right) and the top views are only for CP.

due to the presence of the Marangoni flows. (e) is a MED regime during which particles are pushed inward but some particles remain at the edge (unlike in regime (c)) because evaporation-induced outward flows there become stronger because of the smaller droplet height. At the same time, Marangoni flows are lessened due to the smaller aggregation of SP at the edge compared to the regime (d). Next, (f) and (g) is a CRED regime at the edge but a MED regime inside the domain, where particles near the edge move to the outer ring and those inside the domain are pushed inward at the same time, leading to segregation of the pattern. Similar segregation of particles during evaporation has also been observed in the experiments by Still *et al.* [14] The distance between the outer ring and the inner disk increases with time and partly resembles a broad corona area that appears at the time scale of $\sim 0.5t_f$ [14]. Finally, (h) is a CRED regime due to the decreased drop height and associated high outward flow. Because there is not enough time for all particles inside to arrive at the contact line, the rim area of the dried pattern becomes wider (as in Fig. 2.3(b)) than in the case without surfactant (Case 1).

These alternations of the dominant flows during evaporation are a unique feature of a drying drop containing surfactant: the described behavior clearly shows how one strong (or weak) flow induces the other strong (or weak) flow and describes the different edge dynamics of the particles depending on the spatial strength of the Marangoni flow [15]. The result also indicates that recirculation of adsorbed SP along the surface from the contact line to the center is essential for the dramatic contact line dynamics. The time and length scales of oscillation depends on the relative strength of Marangoni flows, which will be investigated in the following sections.

2.3.2.2 Adsorption rates: uniform-disk patterns.

Now we investigate how adsorption rates of SP at a fixed N_{SP} affect the spatial distribution of CP over time and the deposition pattern. Fig. 2.9 demonstrates the pattern forming process of Case 3, where $Q = 2 \times 10^{-7}$ and $N_{\mathrm{SP}} = 250$ are used as in Fig. 2.3(c) and 2.5. With the increased adsorption rate, the transport of SP to the surface occurs over the entire surface rather than in the limited contact line region where particles are aggregated by outward hydrodynamic flows. The SP skin on the surface forms during

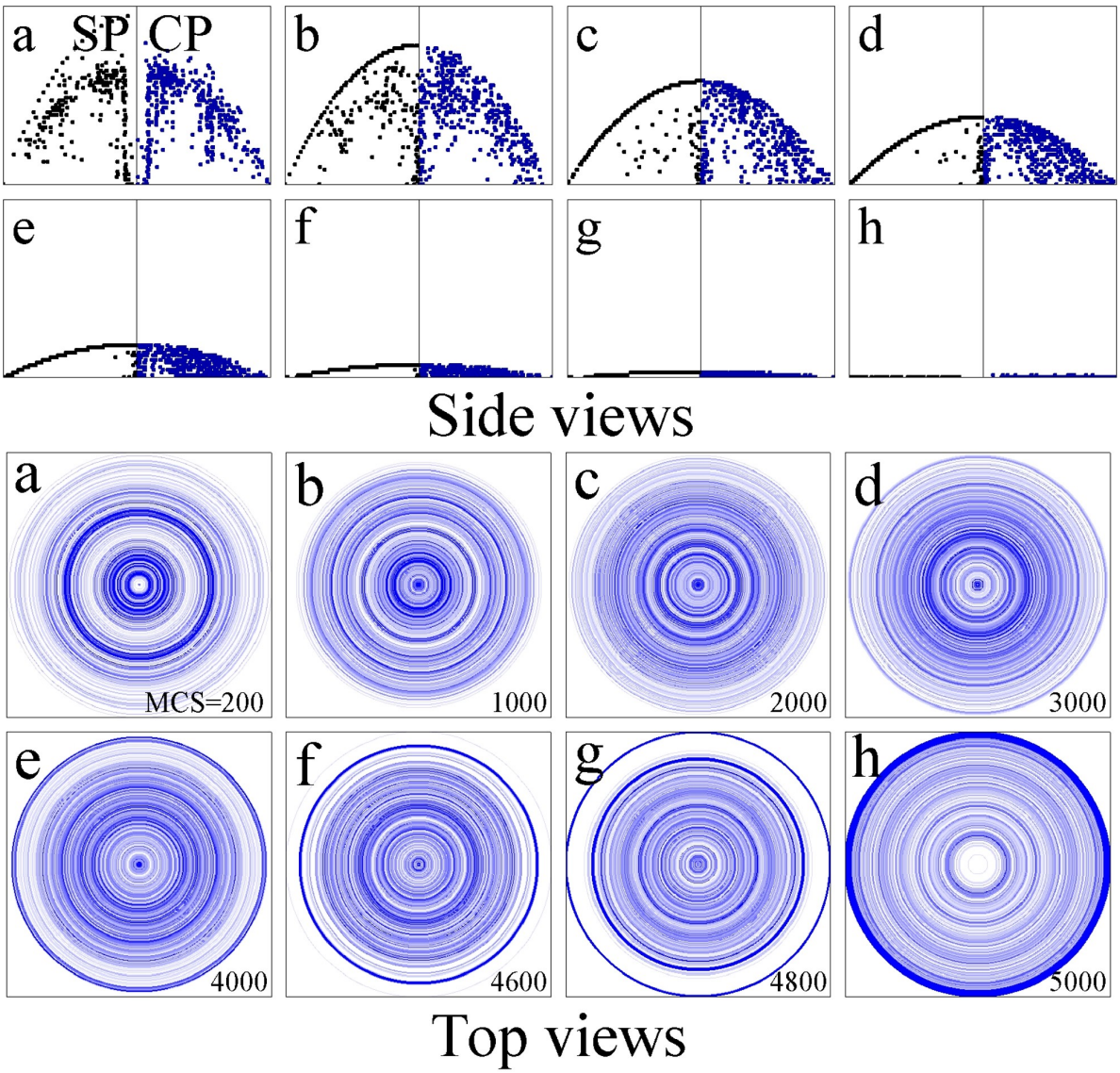

Figure 2.9: Temporal evolution of Sp and CP for Case 3 with $N_{\mathrm{SP}} = 250$ and $Q = 2\times10^{-7}$ from (a)MCS=200 to (h)MCS=5000 with even intervals. The side views include both SP (left) and CP (right) and the top views are only for CP.

the early stages of evaporation and lasts throughout evaporation. Due to the SP skin, inward Marangoni flows develop, and the coffee-ring effect at the edge and subsequent contact line dynamics of CP are significantly suppressed (Fig. 2.9(a)–(e) in top views). Thus most particles stay inside the domain away from the contact line and a clear coffee-ring pattern at the pinned line does not form until the coffee-ring effect overwhelms the Marangoni effect near the terminal drying time (Fig. 2.9(f)). During the final stage of evaporation (Fig. 2.9(h)), there is not enough time for CP to transport to the edge, and so an interior uniform deposition (with a deposit at the contact line) is generated as shown in Fig. 2.9(c). From additional MC simulations (not shown here), it is found that uniform deposition patterns are prevalent for cases with the same adsorption rates ($Q = 2 \times 10^{-7}$) independent of N_{SP}. This result indicates that uniform patterns can be obtained when the adsorption rate rather than the flow dynamics (or evaporation rate) determines the spatial distribution of the surfactant on the surface.

Note that in the present model, the desorption of SP occurs mostly near the center where SP are saturated. However, a desorption mechanism different from the current one can further change the surfactant dynamics and the resultant deposition patterns. As such, we can suppose that a desorption mechanism including the electrostatic repulsion of the ionic surfactant may capture the relevant time and length scales of stable particle circulation reported in previous experiments by providing different SP distributions on the surface [14].

2.3.2.3 Initial surfactant numbers:multi-ring patterns

This section presents the effects of N_{SP} on the droplet dynamics of Case E, where N_{SP} is larger than Case 2 while Q is the same ($Q = 2 \times 10^5$ and $N_{\mathrm{SP}} = 800$ as shown in Fig. 2.4(e) and 2.5). Fig. 2.10 shows a skin layer of SP formed on the surface and temporal arch-shaped patterns of SP and CP, which are also observed in Case 2. However, due to the increased NSP, adsorption occurs over a larger area in an early time regime (Fig. 2.10(a)–(c)). The SP skin induces Marangoni flows which suppress the early development of the coffee-ring effects. Thus the clear formation of a coffee ring is delayed to the intermediate time regime (Fig2.10(d)), which is followed by the consequent Marangoni

effects (Fig. 2.10(e) and (f)). It is noted that the SP skin in the early time regime is not as dense as in Case 3 (studied in Fig. 2.9), and therefore the early suppression of coffee ring effects is not as strong as in Case 3. Based on the comparison of CP dynamics between Case 3 and Case E, we illustrate the different roles of N_{SP} and Q in the SP skin forming process. A quantitative discussion on the different roles of the parameters is also presented in the next section. In the late time regime (Fig. 2.10(g)), the particles tend to separate into an outer ring and an inner disk, where coffee-ring flows and Marangoni flows are dominant at the contact line and in the interior, respectively. However, the overall magnitudes of the two flows are weakened compared to those in Case 2 mainly because of the stronger suppression of the early coffee-ring effects. During the final regimes of evaporation (Fig. 2.10(g)), the remaining SP in the bulk are forced to transport to the free surface as the overall number concentration of SP increases with evaporation. Due to the larger number of SP adsorbed to the surface compared to Case 2, stronger Marangoni flows are induced. That is, Marangoni effects locally compete with the rush-hour coffee ring effects, leading to the formation of a multi-ring pattern as shown in Fig. 2.4(e).

The number of multi-rings increases with N_{SP} as shown in Fig. 2.4. The results suggest that multi-ring patterns can form when N_{SP} is large enough that the induced Marangoni effect is locally in balance with the strong rush-hour effect during the final stage of evaporation. In addition, Q should be large enough to suppress the coffee ring effects during the early stage of evaporation. Note that multi-ring patterns induced by the surfactant have not yet been reported from experiments while coffee-ring and uniform patterns have been found in pinned systems [9, 41]. One possible explanation is that, for most cases in real situations, coffee-ring effects are dominant over the entire domain during the late stage of evaporation (as in Case 2). It is also possible that Marangoni effects during the early stages of evaporation may dominate over the entire area of the surface even in the presence of a small amount of surfactant (as in Case 3).

2.3.2.4 Quantitative comparison

The coffee ring flows are enhanced during evaporation since the flows are inversely proportional to the droplet height. Evaporation also enhances SP concentration and therefore

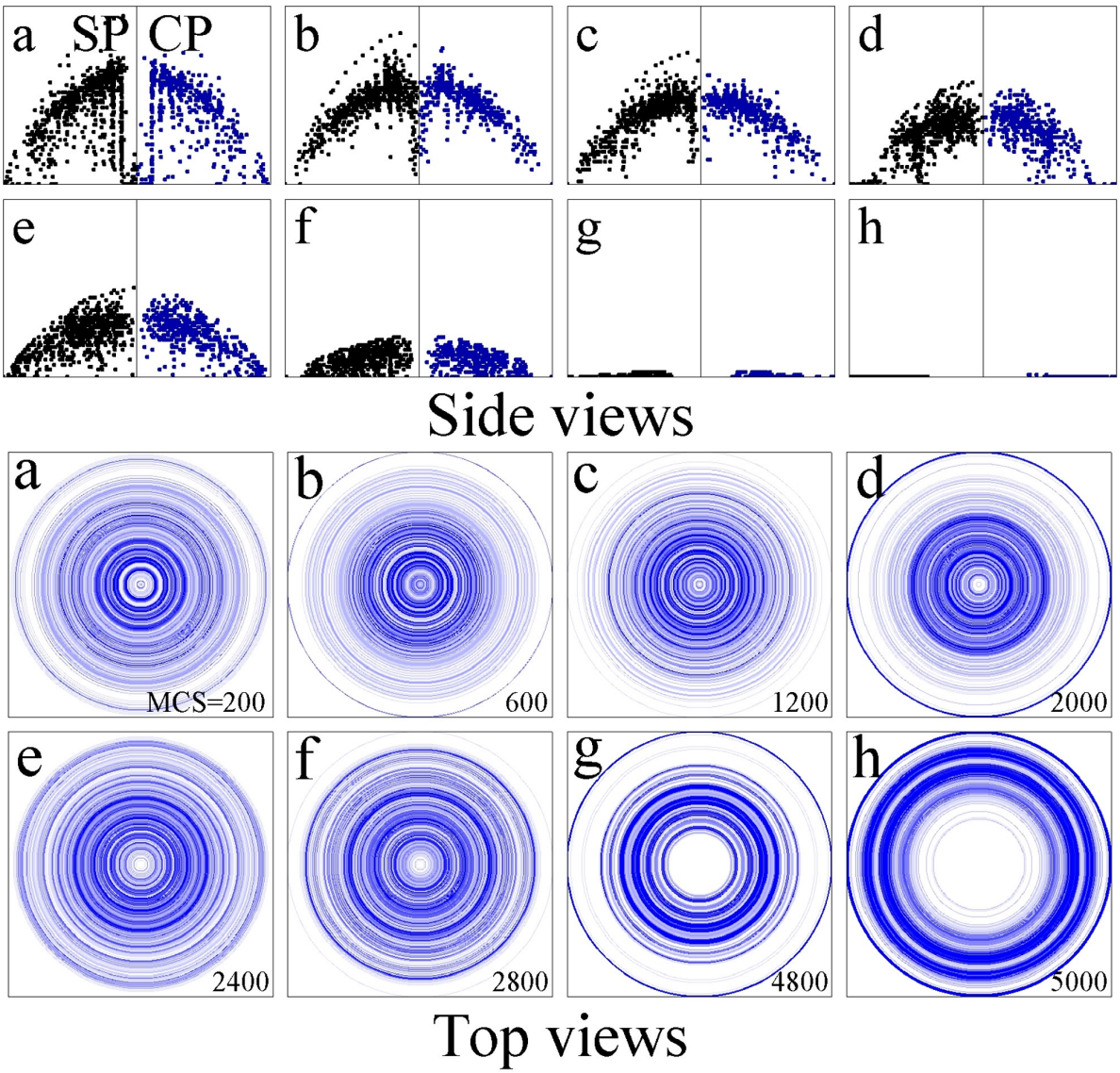

Figure 2.10: Temporal evolution of Sp and CP for Case E with $N_{SP} = 800$ and $Q = 2 \times 10^5$ from (a)MCS=200 to (h)MCS=5000 with even intervals. The side views include both SP (left) and CP (right) and the top views are only for CP.

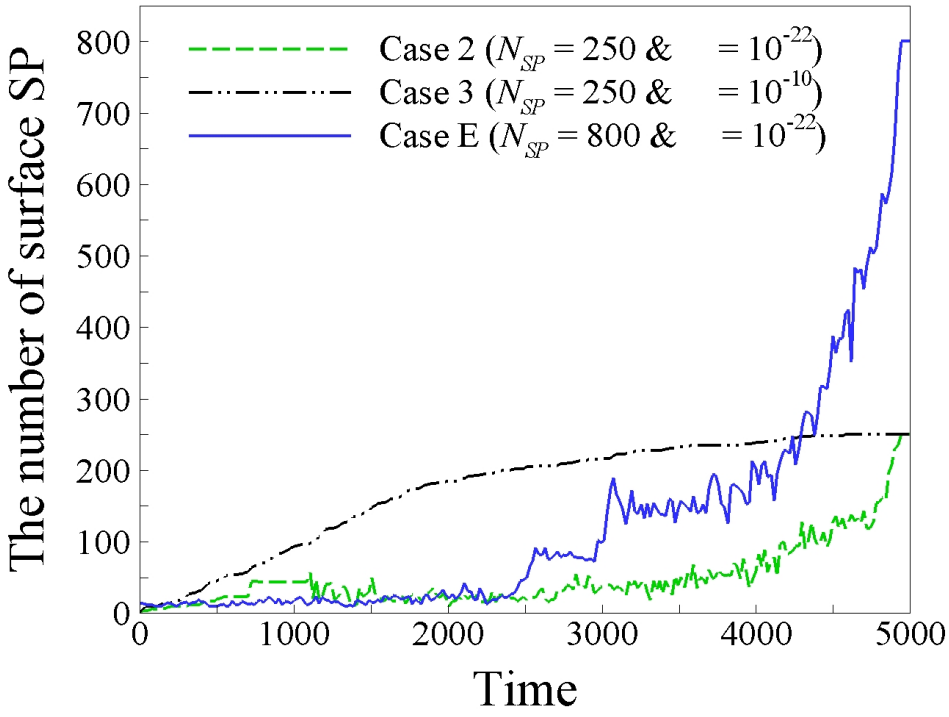

Figure 2.11: Temporal evolution of the total number of SP on the surface for Cases 2, 3, and E.

the Marangoni flows. In the previous section, it is observed that deposition patterns sensitively depend on the concentration of SP on the surface of the droplet. Here, we quantitatively evaluate various skin-forming processes and the corresponding relative strength of the Marangoni flows.

Fig. 2.11 shows the changes of the SP number on the surface during evaporation. For all cases considered, it is readily observed that the number of SP on the surface grows monotonically as the concentration of SP increases with evaporation. In particular, at the final stage of drying, the surface touches the substrate and adsorbs all the remaining particles from the bulk almost at once, which dramatically increases the SP number. Case 3 (studied in Fig. 2.9) has the same N_{SP} as Case 2 (studied Fig. 2.8), but more SP are on the surface at a given time due to the higher adsorption rate. Case E (studied in Fig. 2.10) has significantly large N_{SP}, which causes more frequent adsorption over an extended area. However, the number of SP which the surface adsorb during 1–2400 MCS is nearly the same as in Case 2, despite the significant difference in N_{SP}. This is because the transport rate of SP to the surface is limited by the adsorption rate rather than the

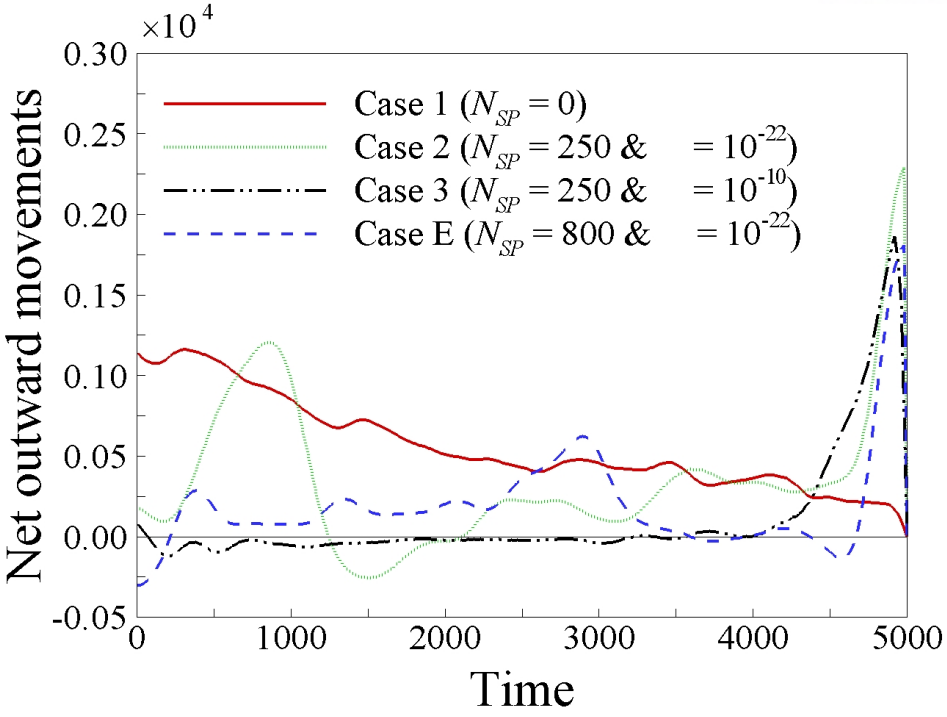

Figure 2.12: Temporal evolution of net outward movements of CP for Cases 1, 2, 3, and E. The value at each time is the sum of all accepted signed random walks: the sign is positive if accepted in the positive r-direction and negative if accepted in the negative r-direction.

overall concentration in the bulk. As the overall bulk concentration further increases during 2400–5000 MCS, the transport rate to the surface grows proportionally. This implies that the rate is limited by the bulk SP concentration in this time regime.

Now we introduce a simple measure of the net outward movement (NOM) of CP to qualitatively evaluate the relative strength of Marangoni flow and to correlate them with the surface SP. At each MC step, we make a summation of all accepted Monte Carlo attempts for CP in the r-direction by counting +1 for each motion in the positive r-direction and -1 in the negative r-direction. A positive NOM indicates that outward movement of CP from coffee-ring flow occurs more often; conversely a negative value means that the inward movement of CP from Marangoni flow dominates.

Fig. 2.12 illustrates the competitions of the two flows over time in terms of NOM. Case 1 is the coffee-ring flow without surfactant and hence NOM holds positive during the entire evaporation process. It is notable that there is no rush-hour effect based on

the monotonic decrease of NOM; fewer CP are transported to the edge since CP are immediately deposited on arrival at the contact line. Surfactant addition to the drop can cause Marangoni flows, which significantly change the NOM dynamics and capture oscillatory dynamics of CP at the contact line. Initially, NOM of Cases 2, 3 and E are smaller than those of Case 1 (and can even be negative, as in Case E). For Case 2 (studied in Fig. 2.8), NOM shows large oscillations, which suggests a strong coupling between the surfactant dynamics and the droplet dynamics. This corresponds to the back and forth motions of CP at the contact line shown in Fig. 2.8. At early stages of evaporation (1–1500 MCS), strong coffee-ring flows (indicated by the sharp increase in NOM) are seen after a short initial period with little outward flow. Subsequently, strong Marangoni flows are induced by SP transported to the contact line along with the coffee ring flow, which is displayed by the decrease in NOM. Due to the Marangoni effects, the subsequent coffee ring effects are weakened. Thus, as time goes on, smaller oscillations follow, illustrating that weak coffee-ring flows induce weak Marangoni flows, and vice versa. At the late stages of evaporation (4500–5000 MCS), there is an increase in NOM because of the rush-hour effect. Although the number of CP is the same as Case 1, the oscillatory motions of CP due to surfactant delay their outward convection, resulting in the rush-hour effect at the final stage of evaporation.

Case 3 (studied in Fig. 2.9) has a higher adsorption rate than Case 2 and shows more frequent adsorption over a larger area. Such intensive adsorption prevents early development of coffee-ring flows and hence suppresses any oscillatory dynamics of CP. In particular, NOM stays near zero with no oscillation for most of the drying time and then surges at the last minute of drying due to the rush-hour effect. Case E (studied in Fig. 2.10) contains more SP than Case 2, while the adsorption rate is the same. The higher surface concentration of SP suppresses the coffee-ring flows especially at the early time, resulting in smaller oscillations in NOM. Considering that at early times, the number of SP on the surface in Case E is roughly the same as in Case 2 (Fig. 2.11), it is reasonable to infer that the difference in the surface distribution of SP causes the difference in NOM behaviors. Thus the control of skin-forming processes would be essential in altering the droplet dynamics and the associated deposition patterns.

2.3.3 Conclusions

In this study, we have investigated deposition patterns that arise from a competition between evaporation-induced 'coffee-drop' flows and surfactant-induced Marangoni flows, using a new lattice gas model. This model uses a Monte Carlo method to find the coupled dynamics of surfactant and colloid motion occurring in a pinned drying drop, and simulates the deposition formation of colloidal particles. At a fixed evaporation rate, we study the effects of adsorption rates and the initial number of SP on the strength of the coffee-ring and Marangoni flows. The effects result from the different dynamics of the surfactant skin formation on the drop, and cause different deposition patterns. The recirculation of SP is essential to have oscillatory motions of CP at the contact line.

For slow adsorption rates, a transition from coffee-ring patterns with wider rim areas to multi-ring patterns are obtained in the evaporated drops as the initial number of SP increases. On the other hand, for fast adsorption rates, homogeneous patterns (combined with the outer ring deposits at the contact lines) are observed independent of N_{SP}. The simulation results show that although the Marangoni effect overall increases with both adsorption rate ($\sim Q^{-1}$) and the initial number of SP, N_{SP}, the role of each parameter induces different coupled dynamics and resulting patterns. In fact, the higher Q^{-1} suppresses the earlier development of coffee-ring effects, and the larger N_{SP} induces locally strong Marangoni flows competing with coffee ring flows, especially during the final stage of evaporation.

The results suggest that understanding of the spatial and temporal distribution of SP on the surface over time is critical to the development of self-assembly techniques for various applications that require a fine control of particle deposition from an evaporating drop [15, 79].

2.4 Oscillation dynamics of colloidal particles caused by surfactant in an evaporating droplet

During the evaporation of a droplet, both colloidal particles (CP) and surfactant particles (SP) convect via the evaporation-induced capillary flow toward the contact line. SP in the high concentration region or with high adsorption rate can easily adsorb to the surface, creating Ma flows on the surface. We compute the surfactant concentration gradients at the interface using the Langmuir's isotherm and obtain the relative strength of Marangoni flows to the capillary flow, Q, which is defined by:

$$Q = -u_r^{Ma}/u_r^{Ca}, \tag{2.30}$$

where u_r^{Ca} and u_r^{Ma} are radial velocities computed from Eq. 2.5 using the first and second terms of $g(r,t)$ in Eq. 2.8, respectively.

$$u_r^{Ca} = \frac{3}{8}\frac{1}{1-\tilde{t}}\frac{1}{\tilde{r}}\left[(1-\tilde{r}^2)-(1-\tilde{r}^2)^{-\lambda(\theta)}\right]\left(\frac{\tilde{z}^2}{\tilde{h}^2}-2\frac{\tilde{z}}{\tilde{h}}\right), \tag{2.31}$$

$$u_r^{Ma} = -\frac{g(R_0\tilde{r},t_f\tilde{t})t_f h_0\tilde{h}}{2R_0}\left(\frac{\tilde{z}}{\tilde{h}}-\frac{3}{2}\frac{\tilde{z}^2}{\tilde{h}^2}\right), \tag{2.32}$$

We take $\tilde{z} = 5/6\tilde{h}$ which is vertical location of droplet near the surface. By examining the spatial and temporal evolution of Q value, we can quantitatively measure the dynamic motions of colloidal particles during the evaporation: the change of Q shows the time and the length scales of oscillatory motions of CP, which will be discussed later.

We first investigate the aggregation characteristics of colloidal particles using Monte Carlo (MC) simulations as in previous studies [20, 50]. Here, the aggregation of colloidal particles represents a phenomenon that develops next to the coffee ring during the evaporation [15, 58]. From a series of MC simulations with different surfactant concentrations, we found that the surfactant concentration can significantly change the flow pattern in the droplet, and hence, we adopt two different surfactant concentrations (relatively high

and low) for the present simulations. We also found from MC simulations with different initial contact angles that the accumulation of particles occurs only when vertical movement of particles is restricted near the droplet edge, and as such, we choose very low initial contact angle of droplet. For all MC simulations, we adopt the following physical parameters: the initial contact angle is $\theta_0 = 0.1047$ and the contact line is pinned at $R_0 = 4$ mm during the entire evaporation time of $t_f = 600$ s. The number of cells in the radial and axial directions are $n_r = 600$ and $n_z = 31$, respectively. The radii of CP and SP are specified as $R_{CP} = R_{SP} = 10^{-3}$ mm. The number of CP, N_{CP}, is set to 500 and the number of SP, N_{SP}, varies depending on cases. The total MC steps (MCS) of 10000 is used as the total drying time, which is approximately consistent with the characteristic value of evaporation-induced velocity of $5\,\mu m s^{-1}$. Note that all simulation results are presented in top and side views of the portion of the droplet near the edge.

2.4.1 Particle dynamics and flow patterns

We start by presenting the typical pattern forming process of colloidal particles during the evaporation. Fig. 2.13 shows the top views of Case A with small N_{SP} of 250, Case B with N_{SP} of 750 and Case C with large N_{SP} of 1500. The sequence of images in time illustrate different phases of the formation of particle aggregation and depletion zones close to the contact line as well as the growth of a coffee ring at the contact line. !!(1)Here, we separate the whole drying time into three different periods, depending on what the dominant flow is: 1. the early phase (capillary flow dominant); 2. the oscillatory phase (Ma flow becomes comparable to Ca flow); 3. the final phase (capillary flow dominant).!!

For Case A with small N_{SP}, it is readily observed that the particle aggregation and depletion zones develop near the droplet edge during the early phase of evaporation (see Fig. 2.13 A1). As the droplet evaporation starts, both SP and CP are transported to the edge by the outward capillary flow. Subsequently, SP transported to the edge generate Marangoni flow at the contact line. Henceforth, we call this flow as an 'outer' Marangoni flow. In the oscillatory phase, since the outer Ma flow prevents the particles from approaching the edge, the aggregation of CP close to the contact line starts to occur (see Fig. 2.13 A2–A4). We found that the relative strength of the outer Ma flow to the Ca flow determines the location of particle aggregation, repeating the periodic increase during the evaporation. Therefore, the oscillatory motion of CP following the flow can be also observed. In the final phase, the aggregation of CP is released so that these are transported to the droplet edge due to the divergence of the capillary flow, called 'rush hour effect' (see Fig. 2.13 A5).

For Case B and C with larger N_{SP}, the formation of the aggregation and depletion zones during the early phase of evaporation also occurs as in Case A. For these case, however, not only the CP but also the SP are accumulated in the aggregation zone (now shown here), which consequently creates an additional Marangoni flow in the oscillatory phase. We refer to this flow as an 'inner' Marangoni flow, which renders accumulated particles to swirl at the aggregation zone(see Fig. 2.13 B2–B4 and C2–C4). By comparing Fig. 2.13 A2–A4 with Fig. 2.13 B2–B4 and Fig. 2.13 C2–C4, we can identify that the

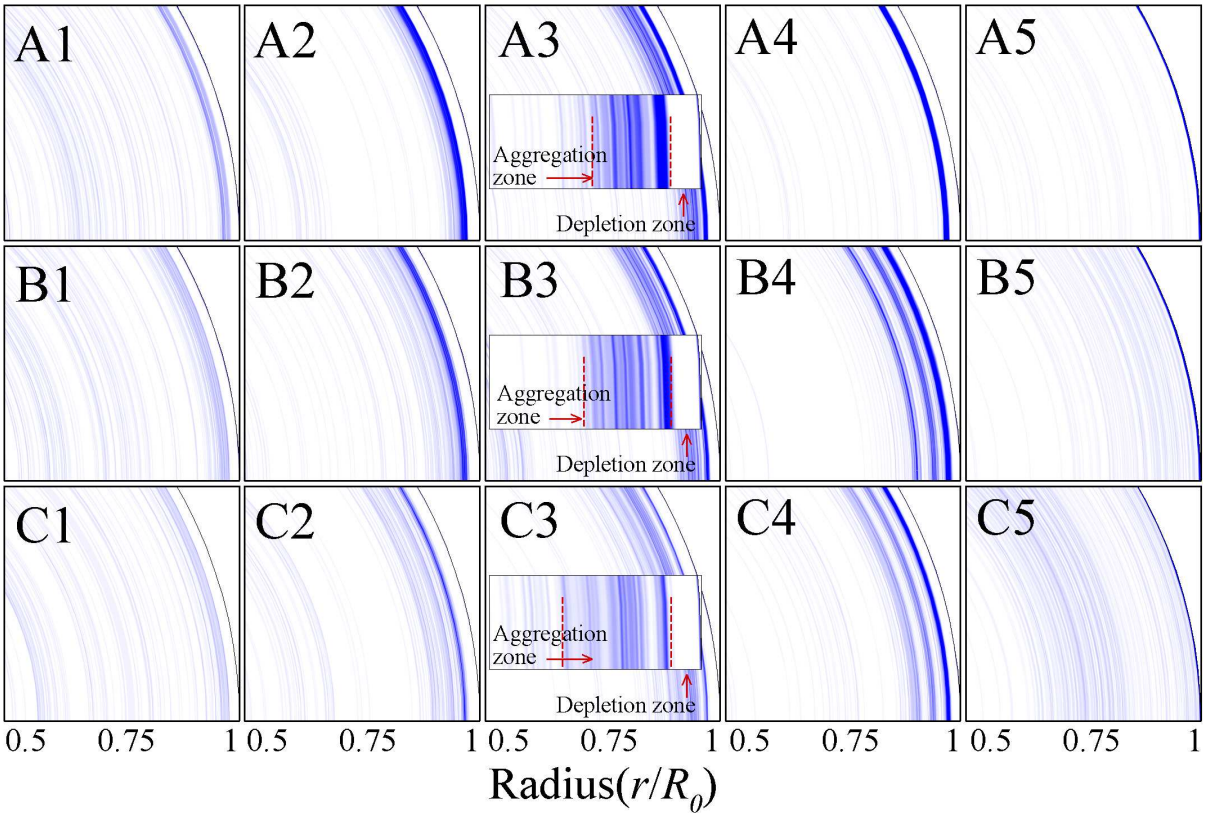

Figure 2.13: Temporal evolution of CP for Case A with $N_{SP} = 250$ (top), Case B with $N_{SP} = 750$ and Case C with $N_{SP} = 1500$ (bottom). From left to right, MCS = 1200 $\sim$ 6000 with even intervals.

swirling of the particles occurs within a wider region in Case of larger N_{SP} than in Case of smaller N_{SP}. We also find that the amount of accumulated CP in Case of larger N_{SP} in aggregation zone is relatively small compared to that in Case of smaller N_{SP}. This is because a large amount of SP creates local Marangoni flow over the entire droplet, which consequently weakens the overall coffee ring effect.

To verify the occurrence of the inner and outer Marangoni flows, the CP patterns and the profiles of u_r^{Ma} and u_r^{Ca} along the radial direction are shown in Fig. 2.14. From Fig. 2.14 A2, B2 and C2, it is readily observed that u_r^{Ma} is slightly greater than u_r^{Ca} very next to the droplet edge. This implies that the inward Marangoni flow dominates over the capillary flow, leading to inward particle movements. This verifies the occurrence of the outer Marangoni flow induced by the SP at the droplet edge. It is of interest to note that the location of the aggregation zone is determined by the relative strength of the outer Marangoni flow. The velocity profiles for each pattern identify that the aggregation zone is formed at the inner end of the region dominated by the outer Marangoni flow. The flow repeats the periodic increase during a certain period, in which either the Marangoni flow or the Capillary flow is in turn dominant. Therefore, it is possible to capture the oscillatory motion of the particle by examining the temporal evolution of the outer Marangoni flow, which will be discussed later.

For Case B and C, we can find a wide region (Marked as a green box) where u_r^{Ma} is much greater than u_r^{Ca}. At this region, the inward Marangoni flow dominates over the capillary flow such that as the evaporation proceeds, we can observe swirling vortices of particles in the aggregation zone, which verifies the formation of the inner Marangoni flow induced by the SP accumulated in the aggregation zone.!!(2,3)Since the height of the droplet in the aggregation zone is sufficiently low for SP to adsorb on surface, the surface coverage of SP is proportional to the SP concentration in the droplet bulk. From the Eq.(2.8) and Eq.(2.32), note that u_r^{Ma} is proportional to the terms of Γ in g, i.e.

$$u_r^{Ma} \propto \Gamma'/(\Gamma_\infty - \Gamma), \tag{2.33}$$

Therefore, the strength of the inner and outer Ma flows is proportional to the SP

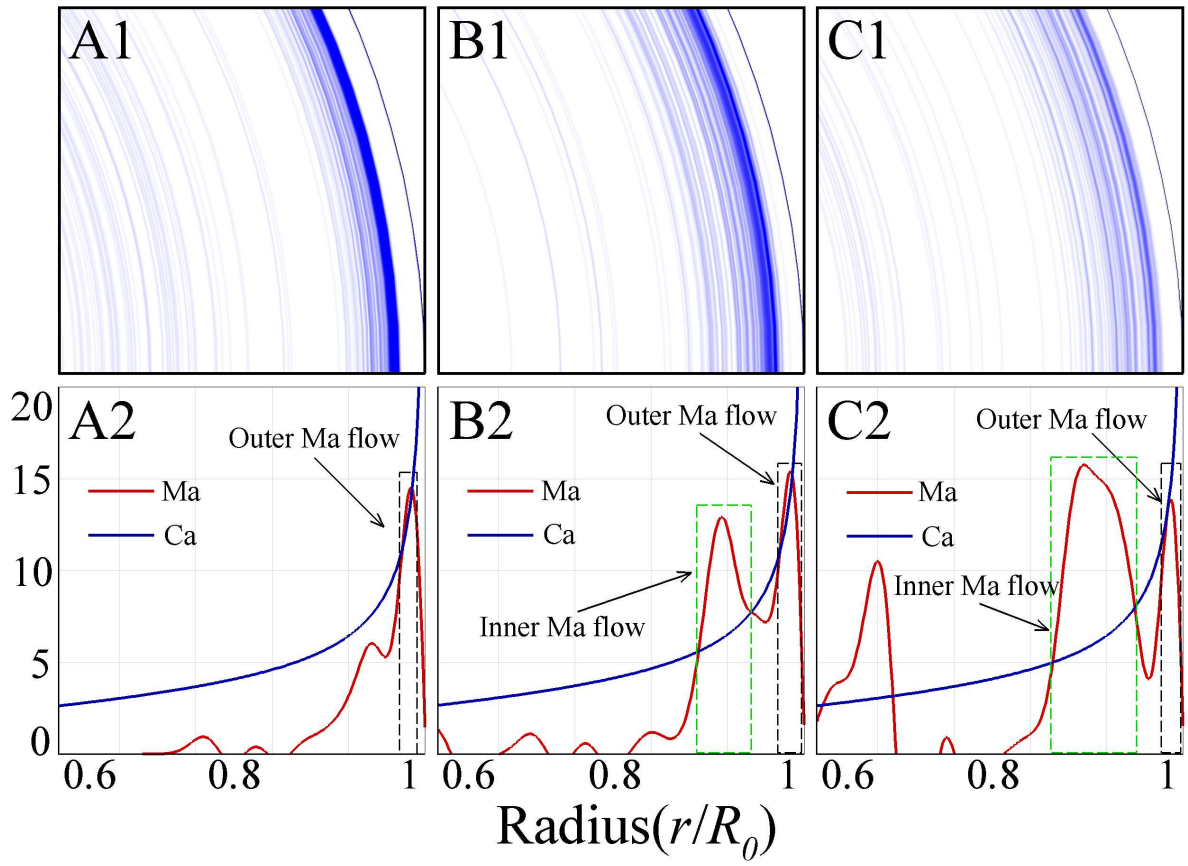

Figure 2.14: The colloidal particle patterns (top) and the profiles of u_r^{Ma} and u_r^{Ca} (bottom) for Case A with $N_{SP} = 250$ (left) and Case B with $N_{SP} = 1500$ (right) at 2700 MCS.

concentration at their locations.!! For Case A with small N_{SP} of 250, the SP concentration is not high enough at the region where the inner Ma flow can develop such that we cannot observe any inner Ma flows. For Case B and C with larger N_{SP}, however, there exist enough SP such that the inner Marangoni flow can develop to move the CP accumulated in the aggregation zone inward. Also, comparing Case B and C, it can be seen that stronger inner Ma is induced in C because the SP concentration of C is higher.

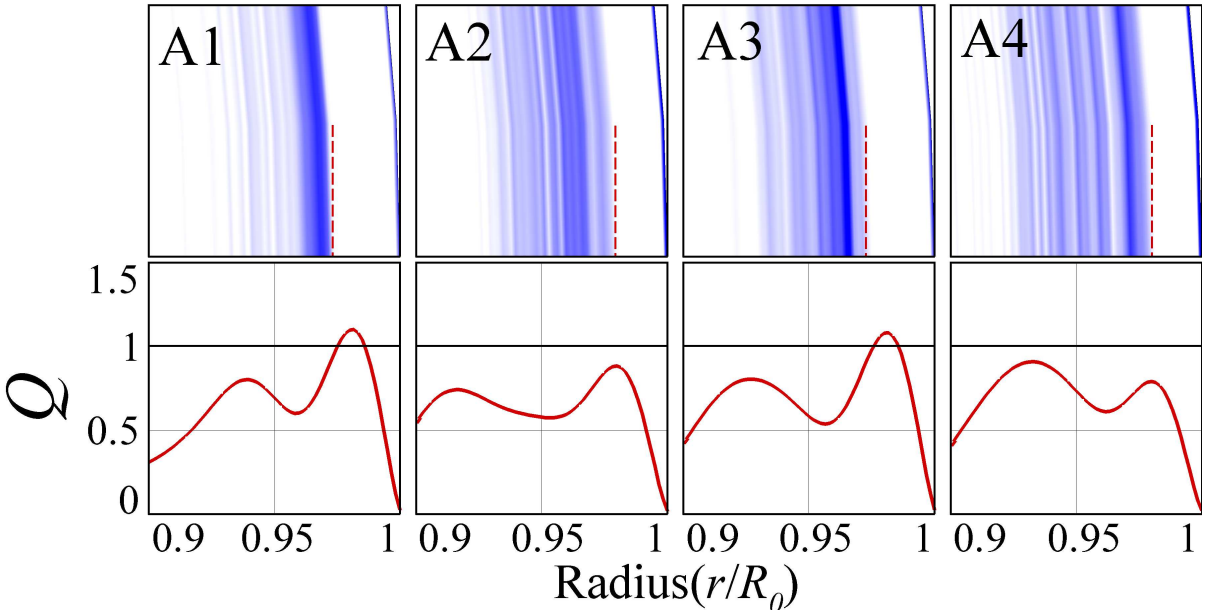

Figure 2.15: The CP patterns and the profiles of Q value for Case A with $N_{SP} = 250$. From left to right, MCS = 2665, 3015, 3050, 3380.

2.4.2 Time-dependent oscillatory movement of particles

In this section, we further investigate the influence of the flow patterns on the characteristics of CP dynamics such as its back-and-forth movement. To explicitly identify which flow is dominant for a given CP pattern at a specific time, we present four typical CP distributions and the corresponding Q profile during oscillatory phases.

Fig. 2.15 shows CP patterns together with the radial profile of Q for Case A to clarify the dependency of the CP pattern on the flow pattern. As mentioned in the previous section, the outermost peak of Q near the droplet edge represents the strength of the outer Ma flow. When Q is greater than unity as in Fig. 2.15 A1 and A3, the particles move inward by the Marangoni flow, which can be confirmed by the increase of the depletion zone. In Fig. 2.15 A2 and A4, however, $Q < 1$ indicates that the outward capillary flow induced by the evaporation overwhelms the inward Marangoni flow, which causes the aggregation zone to move outward, narrowing the depletion zone. Such alternating Q value lasts up to about $0.8t_f$.

To figure out the characteristics of the particle oscillation, the temporal evolution

of the maximum Q value, Q_{max}, near the droplet edge is shown in Fig. 2.16. Since the alternating Q value around unity represents an indirect measure of the oscillating motion of the particles, we can understand the dynamic features of particle movement by examining the characteristics of Q_{max} such as the period and beginning time of its oscillation. As shown in Fig. 2.16, the alternating Q_{max} value in both Cases A and B indicates the presence of oscillatory dynamics of the particles. Note that depending on the overall concentration of particles in the aggregation zone, the characteristics of the oscillatory motions becomes different. When the concentration of CP is low and the width of aggregation zone is relatively small, the back-and-forth movement of CP can be observed, while the CP concentration is high and its width is relatively large, swirling motions in Marangoni eddies occur.

From the simulation results, we can estimate the time scale required for the outer Ma flow to build sufficient strength to overcome the Ca flow, preventing particles from approaching the contact line and generating the aggregation zone close to the droplet edge. Since the value of Q is proportional to the amount of SP located at the of the droplet, the higher the SP concentration is, the earlier the occurrence of aggregation zone is. It is supported by the observation in the simulations that the aggregation initiating time of Cases A,B and C are approximately 420 MCS, 180MCS and 90 MCS, respectively.

To clearly understand the dynamic characteristics of the particle oscillation, we illustrate its mechanism in Fig. 2.17 and 2.18 in terms of the dominant flows of Ca flow and Ma flow in different locations of the droplet. In the axial direction, we separate the droplet into two regions: 1. the top layer where the Ma flow is dominant under the influence of the surface flows; 2. the bottom layer where the Ca flow is dominant regardless of the surface effect. In the radial direction, we also separate the droplet into two regions: 1. the aggregation zone (r_i); 2. the droplet edge (R_0).

Fig. 2.17 shows the dynamics of CP by the outer Ma flow for Case A. During the early stage of the evaporation (see Fig. 2.17a), the occurrence of the aggregation and depletion zones are determined by the early formation of the coffee ring and subsequent development of the Ma flow. During this stage, the evaporation-induced Ca flow carries both CP and SP toward the contact line, and hence, the formation of the coffee-ring

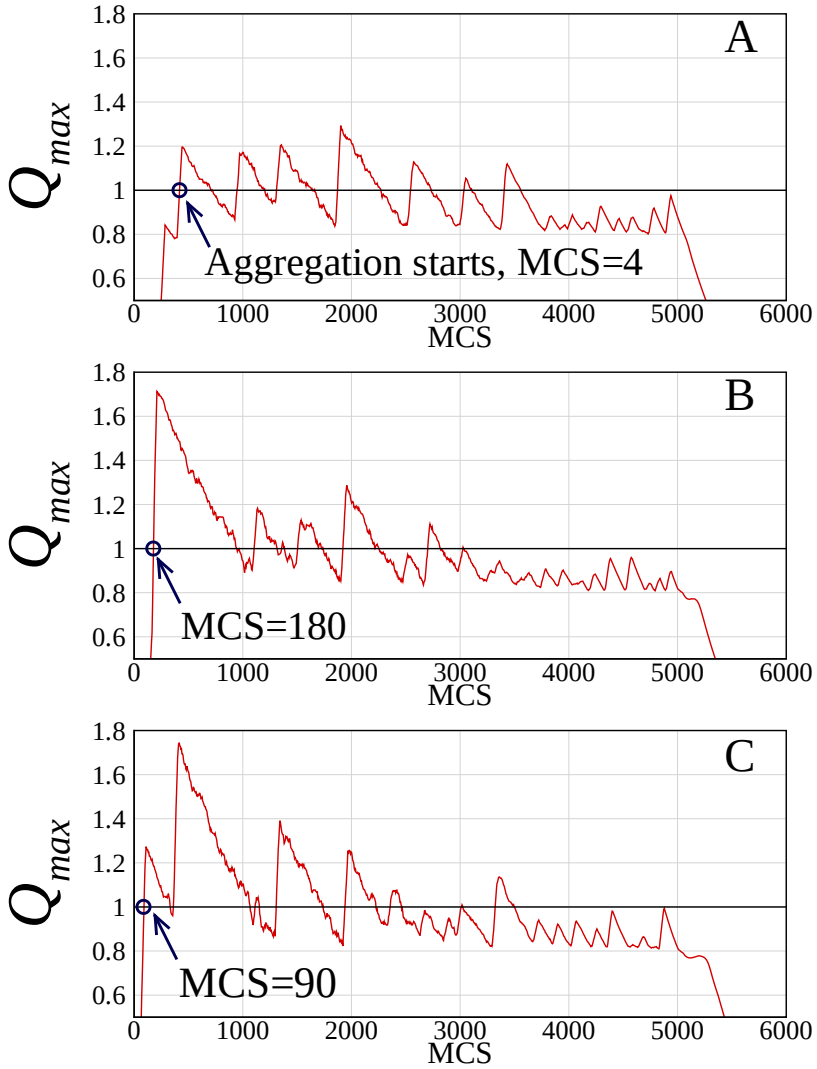

Figure 2.16: Temporal evolution of the maximum Q near the droplet edge for Cases A (top) and B (bottom).

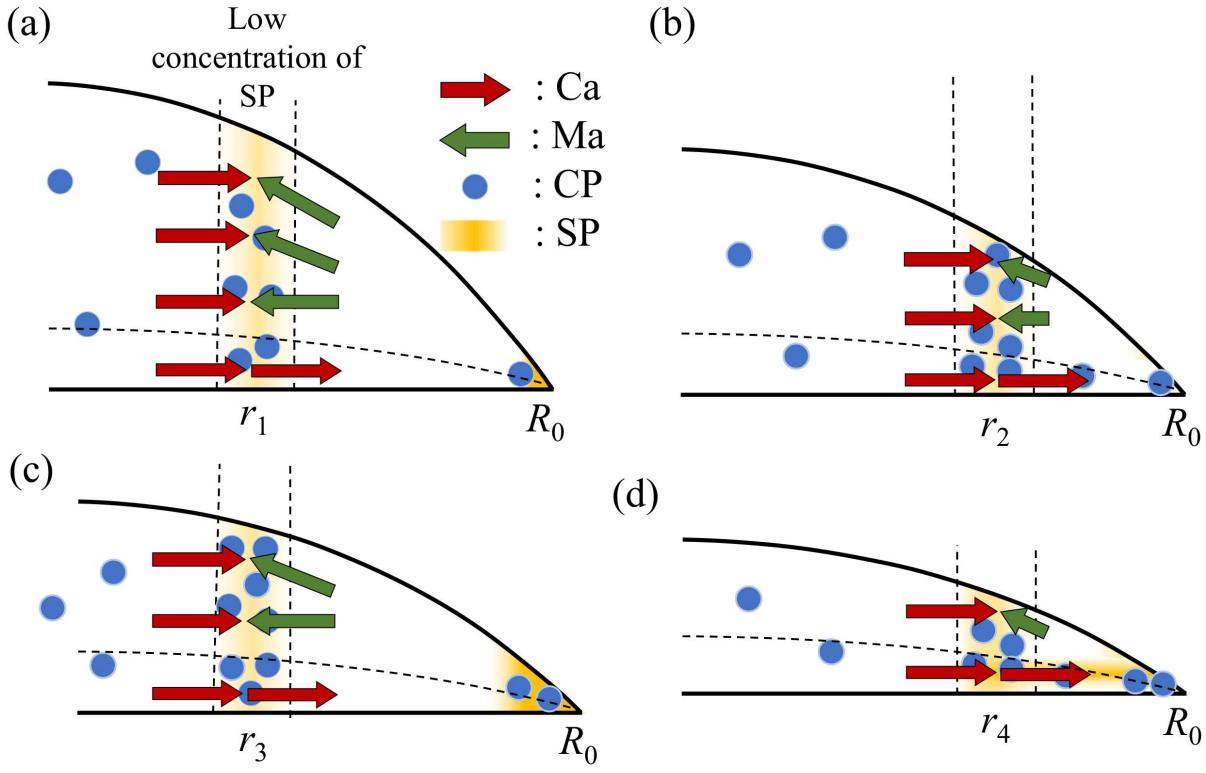

Figure 2.17: A schematic description of the oscillatory movement of CP at different characteristic times.

starts at the edge, similar to that of a drying drop without surfactant. When large enough number of surfactant particles are accumulated at the edge, the outer Ma flow overcoming the Ca flow develop at the top layer. At the same time, both CP and SP start to aggregate in the aggregation zone because a stagnation zone develops due to the opposite flows of the Ma and Ca flows at $r = r_1$.

Since the supply of SP to the coffee ring is significantly reduced by the outer Ma flow, the strength of the flow is maintained for a certain period of time. As the evaporation proceeds, the intensity of the coffee ring effect increases significantly in time. Therefore, after a sufficient time for the Ca flow to overcome the Ma flow (see Fig. 2.17b), the aggregation zone moves outward from r_1 to r_2. At the same time, the Ma effect, a surface effect, is easily overwhelmed by the coffee ring effect at the bottom layer. Therefore, a small of SP fixed at r_1 is carried to the coffee ring along the bottom flow. Afterwards, as shown in Fig. 2.17c, the outer Ma flow is enhanced by the more SP at coffee ring, which moves the aggregation zone inward from r_2 to r_3. This mechanism repeats until the competition of these two effects collapses due to the divergence of the Ma effect causing the particle oscillation.

Fig. 2.18 shows a schematic of the CP dynamics due to the interaction between the outer and inner Ma flows in Case C to describe why the particles are supposed to swirl. For the same reason in Case A, the aggregation and depletion zones develop during the early stage of the evaporation (see Fig. 2.18a). For Case C, however, the amount of SP inducing the sufficient strength of outer Ma flow to overcome the Ca flow is supplied to the droplet edge prior than Case A, moving up the oscillatory phase.

Due to the high initial concentration of SP, a sufficient number of SP is also accumulated in r_2, developing an inner Ma flow between r_1 and r_2 in Fig. 2.18a. Then, as shown in Fig. 2.18b, the inner Ma flow moves the SP located at r_2 to r_1 along the top layer. Subsequently particles transported to the r_1 where the inner Ma flow is relatively weaker than Ca flow move back to r_2 by the Ca flow along the bottom layer. This process is also repeated until the Ca flow diverge, leading the aggregated particles to swirl. At the same time, the temporal evolution of the outer Ma flow follows the mechanism in Fig. 2.17 such that the position of r_2 shifts back and forth periodically.

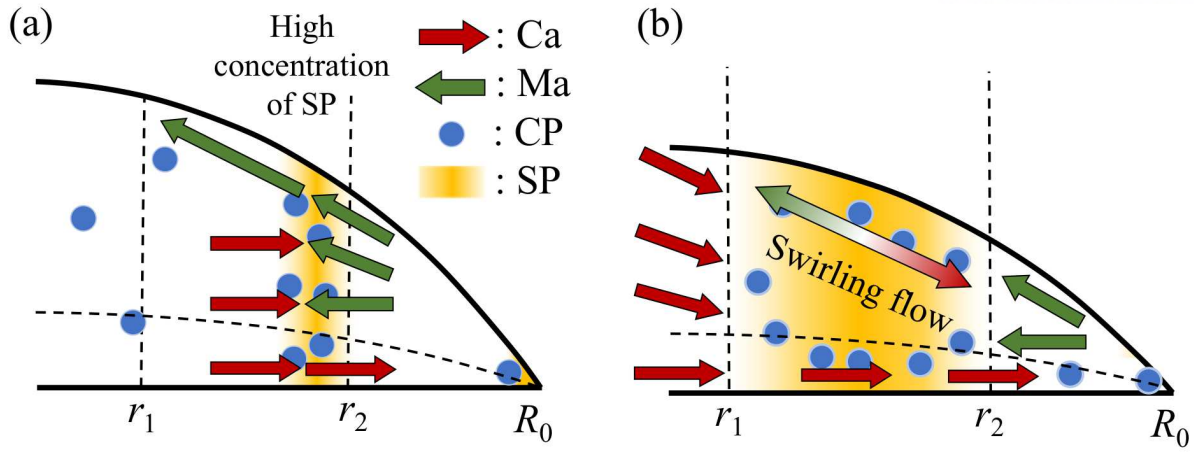

Figure 2.18: A schematic of the swirling pattern of CP for Case B at (a) the early phase of the evaporation and (b) a later time.

2.4.3 Conclusions

We presented the dynamics of colloidal particles in a evaporating drop of certain conditions containing surfactant by computing surfactant-induced Marangoni flows using Langmuir's isotherm in the coarse grained model. This conditions requires an appropriate surfactant concentration and a sufficiently low droplet height. Such flows generate interesting transient motions of colloidal particles near the surface, of which direction depends on the ratio Q, the relative strength of Marangoni(Ma) flows to the evaporation-induced capillary flow(Ca). The Ma flows are divided by the radial position of the droplet, one of which is called the outer Ma flow and the other is the inner Ma flow. We found that as reported in the previous experiments, the outer Ma flow create an aggregation zone close to the contact line. In the droplet containing low concentration of surfactant, only outer Ma flow is significantly generated, whereas in the high concentration, both the outer Ma and consequently inner Ma flow are generated. In the low concentration of surfactant case, the oscillatory back and forth movement of aggregation zone are observed where the competition between the outer Ma and Ca flow occurs, which is quantified by their relative strength Q. Since the flow in the droplet and the motion of particles are consistent, the oscillatory characteristics of the particles can be confirmed through the temporal evolution of the outer Ma flow. The inner Ma flow in the case of high concentra-

tion of surfactant makes the aggregated particles swirl. This is because the particles can move vertically in the region where inner Ma exists. In addition, this study describes the mechanism of particle oscillation and swirling due to interaction between each Marangoni flow and capillary flow.

Chapter III

Extension of pseudopotential lattice Boltzmann method for particle distribution in a evaporating droplet

3.1 Introduction

Multi-phase fluid flows are ubiquitous in our daily life, scientific and industrial processes. A multi-phase system require multiple component with different phases; a liquid water and air system need a multiple components with large density ratios; a liquid water and oil system need a multiple components with small density contrast. Of these systems, coffee ring phenomenon is attracting attention because drying fluids are ubiquitous in nature and industrial processes. When a spilled coffee dries, a ring-shaped pattern remains along the droplet edge, which is commonly referred to as the coffee-ring effect [45]. Since this phenomenon is undesirable in many industrial fields, such as coating [80], nanoassembly [81], nanopatterning [82], and inkjet printing [2], strategies for controlling deposition patterns are needed based on comprehension of the mechanisms for the droplet evaporation and the deposition process. The flow field in an evaporating droplet has been studied since the flow affects the behavior and deposition pattern of particles. In particular, the pioneering study of Deegan et al. [45] elucidated that the outward capillary flow attributes to the coffee-ring effect of the droplet. Hu and Larson [9, 36] numerically

studied the effect of temperature gradient on the droplet surface on the velocity field, and concluded that the coffee ring pattern forms due to both the fixed contact line and the suppression of the counteracting flow. The counteracting flow is commonly referred to as the Marangoni flow that is generated by either temperature gradient or concentration gradient at the liquid interface. Marin et al. [55] experimentally investigated the effect of surfactant on the flow inside a droplet induced by evaporation.

However, few have visualized and quantitatively measured the flow field in an evaporating droplet to predict the final deposition pattern. Due to such limitations of the experimental study, many studies are trying to obtain the flow field either numerically or analytically. Maki and Kumar [83] solved the full convection-diffusion equation of colloid particles by applying the lubrication approximation and elucidated the skin formation by capturing the depth-wise gradient of particle concentration. For numerical studies, Zhao and Yong [84] developed a free-energy-based multiphase lattice Boltzmann model to simulate the evaporation of the colloidal droplet on a solid surface with specified wetting properties. Frijters et al. [85] applied the amphiphile LB model to investigate the effect of surfactant and compared it with the effect of colloids on droplets in the presence of shear flow. Despite the numerical and theoretical studies for the particle-laden droplet evaporation, a unified method within the LBM to predict the velocity field and the behaviors of colloids has not been developed.

The objective of this research is to develop a new lattice Boltzmann (LB) model to simulate the evaporation of a droplet containing colloids and surfactant. Our model consists of the pseudopotential LB model for the evaporation of a droplet and the advection-diffusion LB model for colloids. Here, we propose a new approach to retain colloids within the droplet during the phase change of a droplet caused by solvent evaporation. Our simulation results are two-fold: (1) the velocity fields inside the droplet and the contact angle evolution are achieved and are compared with analytic solutions, (2) the deposition patterns are investigated by varying the Peclet numbers.

3.2 Model

3.2.1 The lattice Boltzmann method

As a framework of the LBM, a 2-D isothermal LBM with the D2Q9 model is adopted. The basic idea of LBM is to treat a statistical group of fluid particles as fictitious particles. By discretizing the Boltzmann equation with the BGK operator [22], we obtain the lattice Boltzmann equation:

$$f_i(\mathbf{x} + \mathbf{c}_i\Delta t, t + \Delta t) - f_i(\mathbf{x}, t) = -\frac{\Delta t}{\tau}[f_i(\mathbf{x}, t) - f_i^{eq}(\mathbf{x}, t)], \tag{3.1}$$

which describes the evolution of the particle distribution function, f_i, toward the neighboring node, $\mathbf{x}+\mathbf{c}_i\Delta t$, with a discrete set of velocities, $\mathbf{c}_i$, and time step, Δt. The collision operator term expresses the relaxation of f_i to the equilibrium distribution function, f_i^{eq}, by the single relaxation time, τ.

The Navier-Stokes equation can be derived through the Chapman-Enskog expansion of Eq. 3.1 at the low Mach number limit and low Knudsen numbers. By integrating the particle distribution function over the microscopic velocity field, macroscopic properties such as density and velocities can be obtained and the speed of sound c_s is given by $c_s = \sqrt{\kappa RT} = 1/\sqrt{3}$, where the specific heat ratio κ is unity for the D2Q9 method. We can also obtain the macroscopic variables from f_i^{eq} since it enforces the mass and momentum conservation during the collision process:

$$\begin{aligned} \sum f_i^{eq} &= \sum f_i = \rho, \\ \sum \mathbf{c}_i f_i^{eq} &= \sum \mathbf{c}_i f_i = \rho\mathbf{u}. \end{aligned} \tag{3.2}$$

3.2.2 The pseudopotential model

We can model multi-component systems by introducing interaction forces in the LBM. For multi-component fluids consisting of K species, the evolution equation for the distribution function of each component, ${f_i}^k(\mathbf{x})$, can be written as:

$$f_i^k(\mathbf{x}+\mathbf{c}_i\Delta t, t+\Delta t) - f_i^k(\mathbf{x},t) = -\frac{\Delta t}{\tau}(f_i^k(\mathbf{x},t) - f_i^{k,eq}(\mathbf{x},t)), \quad k=1,\cdots,K, \tag{3.3}$$

where the equilibrium distribution function, $f_i^{k,eq}$, is given by:

$$f_i^{k,eq}(\rho^k, \mathbf{u}_{eq}^k) = \omega_i \rho^k \left(1 + \frac{\mathbf{c}_i \cdot \mathbf{u}_{eq}^k}{c_s^2} + \frac{(\mathbf{c}_i \cdot \mathbf{u}_{eq}^k)^2}{2c_s^4} - \frac{\mathbf{u}_{eq}^k \cdot \mathbf{u}_{eq}^k}{2c_s^2}\right) \tag{3.4}$$

The macroscopic densities and velocities are defined by:

$$\begin{aligned} \sum f_i^k &= \rho^k, \\ \sum \mathbf{c}_i f_i^k &= \rho^k \mathbf{u}^k. \end{aligned} \tag{3.5}$$

Shan and Chen [23] incorporated the interaction force, $\mathbf{F}$, to make the fluid immiscible:

$$\mathbf{F}^k(\mathbf{x},t) = -G\psi^k(\mathbf{x},t)\sum_{i=1}^{8}\omega_i\psi^{\bar{k}}(\mathbf{x}+\mathbf{c}_i\Delta t, t)\mathbf{c}_i. \tag{3.6}$$

The force includes the interaction between two fluid components, k and $\bar{k}$, at the nearest neighbor and the sign of parameter, G, determines whether the interaction force is attractive (when negative) or repulsive (when positive). In the multicomponent multiphase model, positive G should be chosen to make separation between the components. After equilibration, a denser phase of density ρ_{ma}^k and a lighter phase of density ρ_{mi}^k are formed at each component. In this paper, the effective mass, ψ^k, is defined as:

$$\psi^k(\mathbf{x},t) \equiv \psi(\rho^k(\mathbf{x},t)) = 1 - \exp(-\rho^k(\mathbf{x},t)). \tag{3.7}$$

To include the interaction force to LBM, Shan and Chen [23] introduced the equilibrium velocity u_{eq}^k:

$$\mathbf{u}_{eq}^k(\mathbf{x},t) = \mathbf{u}_{bulk}(\mathbf{x},t) + \frac{\tau^k \mathbf{F}^k(\mathbf{x},t)}{\rho^k(\mathbf{x},t)}, \tag{3.8}$$

where u_{bulk} is the macroscopic velocity of the bulk fluid:

$$\mathbf{u}_{bulk} = \frac{\sum_k \sum_i \mathbf{c}_i f_i^k}{\sum_k \sum_i f_i^k}. \tag{3.9}$$

Since the interaction potential $\mathbf{F}^k$ is imposed, the local momentum is not conserved before and after the collision step [86]. Therefore, the macroscopic fluid velocity, $\mathbf{U}_f$, which expresses the motion of the fluid is defined by averaging momenta before and after the collision step:

$$\rho \mathbf{U}_f = \sum_k \sum_i \mathbf{c}_i f_i^k + \frac{1}{2} \sum_k \mathbf{F}^k. \tag{3.10}$$

where ρ is the sum of densities from each component.

3.2.3 A forced advection-diffusion equation

In this section, we introduce an LB method to obtain the colloidal particle concentration, C, dissolved in a multi-phase fluid. To model the particle concentration in the continuum level, we assume that the diameter of particles is much smaller than the droplet height, and hence, they can be transported by the fluid velocity. Based on the assumption, C can be described by the advection-diffusion equation. We solve the equation using the LB method proposed above. Note that prior to solving the advection-diffusion equation of particle concentration, the lattice Boltzmann equation for the medium fluid is solved separately to obtain the velocity field of the fluid.

The colloidal particle concentration in a single-phase flow can be simulated by the method proposed by Michalis et al. [87]. In the model, the evolution of colloid particle concentration can be described by an LB equation:

$$g_i(\mathbf{x}+\mathbf{c}_i\Delta t, t+\Delta t) - g_i(\mathbf{x}, t) = -\frac{\Delta t}{\tau}(g_i(\mathbf{x}, t) - g_i^{eq}(\mathbf{x}, t)) + \left(1 - \frac{\Delta t}{2\tau}\right) F_i^{\text{int}} \Delta t, \quad i = 1, \cdots, 8. \tag{3.11}$$

The truncation of the forcing term and its velocity moments are expressed by [88]:

$$F_i^{\text{int}} = \omega_i \left(\frac{c_{i\alpha}}{c_s^2} + \frac{(c_{i\alpha}c_{i\beta} - c_s^2\delta_{\alpha\beta})u^c_{eq,\beta}}{c_s^4} \right) F_\alpha^{\text{AD}}, \tag{3.12}$$

$$\sum_i F_i^{\text{int}} = 0, \tag{3.13a}$$

$$\sum_i F_i^{\text{int}} \mathbf{c}_i = \mathbf{F}^{\text{int}}. \tag{3.13b}$$

where α and β indicate the coordinates of the system. Similar to the Shan-Chen interaction force, F_α^{SC} is defined by:

$$F_\alpha^{\text{AD}}(\mathbf{x}, t) = -G^{\text{int}}\psi^c(\mathbf{x}, t) \sum_{i=1}^{8} \omega_i \psi^\sigma(\mathbf{x} + \mathbf{c}_i\Delta t, t) c_{i\alpha}, \tag{3.14}$$

where G^{int} is the coefficient of the interaction force and ψ^c and ψ^σ are the effective masses of colloidal particles and surrounding fluid, respectively, as defined in Eq. 3.7.

The macroscopic density, C, and the velocity, $\mathbf{v}$, can be recovered by their momentums:

$$\begin{aligned} \sum_i g_i^{eq} &= \sum_i g_i = C, \\ \sum_i \mathbf{c}_i g_i^{eq} &= \sum_i \mathbf{c}_i g_i = C\mathbf{v}, \end{aligned} \tag{3.15}$$

where the equilibrium distribution function of the colloid particles can be expressed as follows:

$$g_i^{eq} = \omega_i C \left(1 + \frac{\mathbf{c}_i \cdot \mathbf{v}_{eq}}{c_s^2} + \frac{(\mathbf{c}_i \cdot \mathbf{v}_{eq})^2}{2c_s^4} - \frac{\mathbf{v}_{eq} \cdot \mathbf{v}_{eq}}{2c_s^2} \right) \tag{3.16}$$

The distinctive feature of the LB method for the advection-diffusion equation compared to the Navier-Stokes equation is that $\mathbf{v}_{eq}$ is externally obtained from the velocity of the medium fluid (solvent), $\mathbf{U}_f$, in Eq. 3.10. However, we need to modify $\mathbf{v}_{eq}$ by including a force term to retain the colloidal particles in the droplet. Using the forcing scheme of Guo *et al.* [89] which is applicable to single-phase flow, $\mathbf{v}_{eq}$ can be defined as:

$$\mathbf{v}_{eq} = \mathbf{U}_f + \frac{\Delta t}{2C}\mathbf{F}^{\mathrm{SC}}. \tag{3.17}$$

Note that this LB model for the advection-diffusion equation is adopted to solve the concentration distribution of colloidal particles in a droplet.

3.2.4 Chapman-Enskog analysis

In this section, we perform the Chapman-Enskog analysis to derive the advection-diffusion equation and to obtain the macroscopic velocity from the new LB model of colloidal particles. The expansion of the distribution function of colloid, derivatives of time and space, and interaction force are expressed by:

$$g_i = g_i^{(0)} + \epsilon g_i^{(1)} + \epsilon^2 g_i^{(2)}, \tag{3.18a}$$

$$\partial_t = \epsilon\partial_t^{(1)} + \epsilon^2\partial_t^{(2)}, \tag{3.18b}$$

$$\partial_\alpha = \epsilon\partial_\alpha^{(1)}, \tag{3.18c}$$

$$F_i^{\mathrm{int}} = \epsilon F_i^{\mathrm{int},(1)}. \tag{3.18d}$$

Applying the Taylor series expansion to Eq. 3.11, and expanding each term using Eq. 3.18, we obtain the zeroth, first, and second order equations:

$$O(\epsilon^0) : -\frac{\Delta t}{\tau}(g_i^{(0)} - g_i^{eq}) = 0, \tag{3.19a}$$

$$O(\epsilon^1) : (\partial_t^{(1)} + c_{i\alpha}\partial_\alpha^{(1)})g_i^{eq} = -\frac{1}{\tau}g_i^{(1)} + \left(1 - \frac{\Delta t}{2\tau}\right)F_i^{\mathrm{int},(1)}, \tag{3.19b}$$

$$O(\epsilon^2) : \partial_t^{(2)}g_i^{eq} + (\partial_t^{(1)} + c_{i\alpha}\partial_\alpha^{(1)})\left(1 - \frac{\Delta t}{2}\tau\right)\left(g_i^{(1)} + \frac{\Delta t}{2}F_i^{\mathrm{int},(1)}\right) = -\frac{1}{\tau}g_i^{(2)}. \tag{3.19c}$$

From the zeroth moment of Eq.3.19a one can easily obtain

$$\sum_i g_i^{(k)} = 0 \ (k \geq 1). \tag{3.20}$$

By using the above equations, we obtain the zeroth moments of Eq.3.19b-c

$$\partial_t^{(1)} C + \partial_\alpha^{(1)} C U_{f,\alpha} = 0, \tag{3.21a}$$

$$\partial_t^{(2)} C + \left(1 - \frac{\Delta}{2\tau^c}\right)\left(\partial_\alpha^{(1)} \sum_i c_{i\alpha} g_i^{(1)} + \frac{\Delta t}{2} \partial_\alpha^{(1)} \sum_i c_{i\alpha} F_i^{\mathrm{int},(1)}\right) = 0. \tag{3.21b}$$

From the first moment of Eq.3.19b, we obtain

$$\sum_i c_i g_i^{(1)} = \tau\left(-\partial_t^{(1)} C U_{f,\alpha} - \partial_\alpha^{(1)}\left(C U_{f,\alpha} U_{f,\beta} + C c_s^2 \delta_{\alpha\beta}\right) + \left(1 - \frac{\Delta t}{2\tau}\right) F^{\mathrm{int},(1)}\right). \tag{3.22}$$

By substituting Eq. 3.22 into Eq. 3.21b and combining the equation with Eq. 3.21a, we obtain the following equation in vector form:

$$\partial_t C + \nabla \cdot \left(C \mathbf{U}_f + \left(\tau - \frac{\Delta t}{2}\right) \mathbf{F}^{\mathrm{int}}\right) = D^c \nabla^2 C + E, \tag{3.23}$$

where D^c is diffusion coefficient of colloid particles and E is the error term expressed by as follows [90]:

$$D^c = \left(1 - \frac{\Delta t}{2\tau^c}\right) c_s^2, \tag{3.24}$$

$$E = \left(1 - \frac{\Delta t}{2\tau^c}\right)\left[\partial_t \nabla C \mathbf{U}_f + \nabla^2 C \mathbf{U}_f \cdot \mathbf{U}_f\right]. \tag{3.25}$$

Through the Chapman-Enskog analysis, it is verified that the new LB model recovers the advection-diffusion equation. Since the external force is imposed to the colloidal particles at the interface of the medium fluid, the macroscopic velocity of the colloidal particle, $\mathbf{v}$, is supposed to be changed, and can be obtained from Eq. 3.23:

$$\mathbf{U}_c = \mathbf{U}_f + \left(\tau^c - \frac{\Delta t}{2}\right) \frac{\mathbf{F}^{\mathrm{int}}}{C}. \tag{3.26}$$

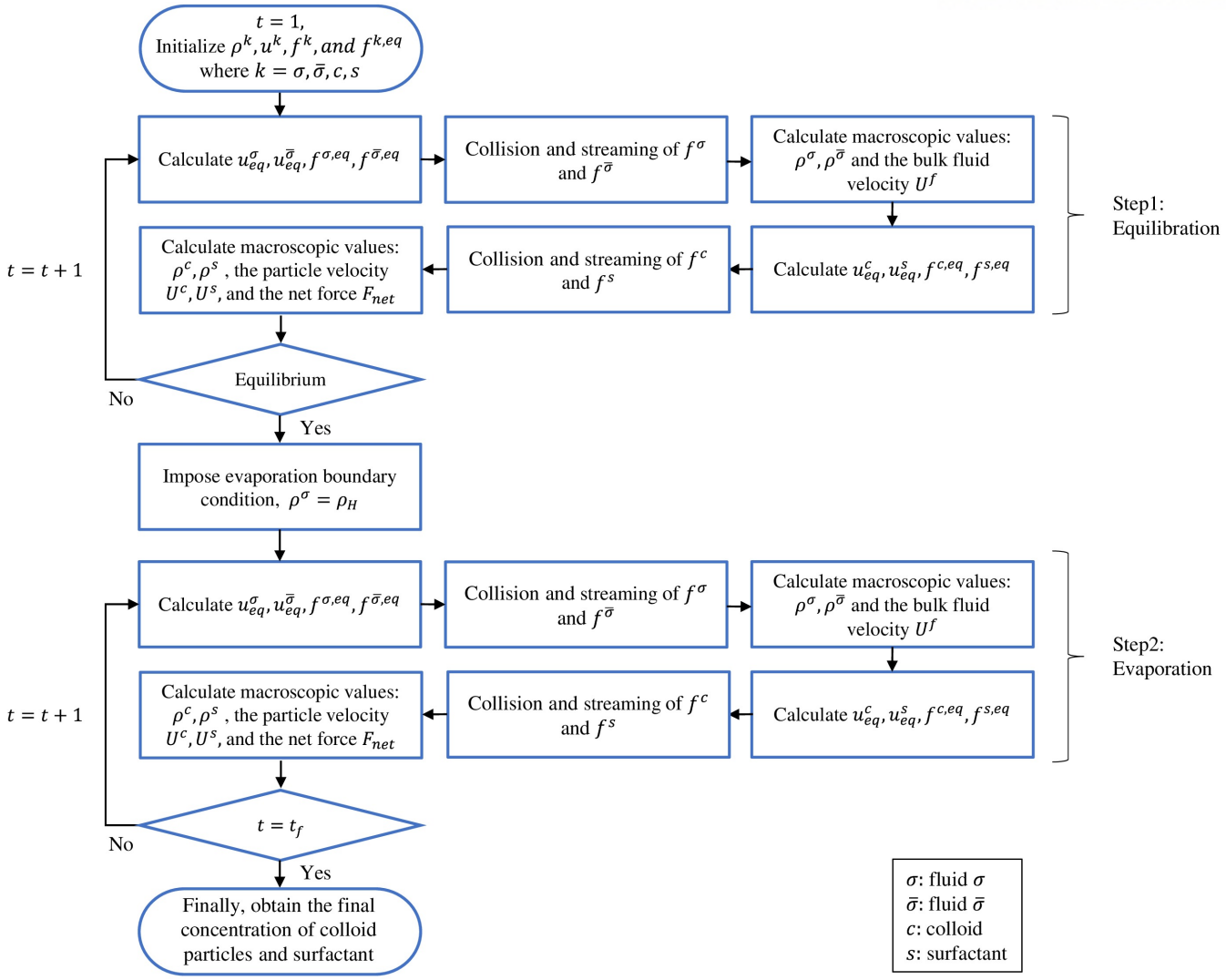

Figure 3.1: Simulation algorithm.

3.3 Results and discussions

The present LBM simulation of an evaporation of a droplet containing colloids is composed of two steps in Fig 3.1: (1) an equilibration process of a droplet so that the droplet is in an equilibrium state and (2) a simultaneous computation of the velocity field of the droplet and the advection-diffusion equation of colloidal particles. The equilibration process improves the stability of the calculation by generating appropriate interfaces and initial conditions.

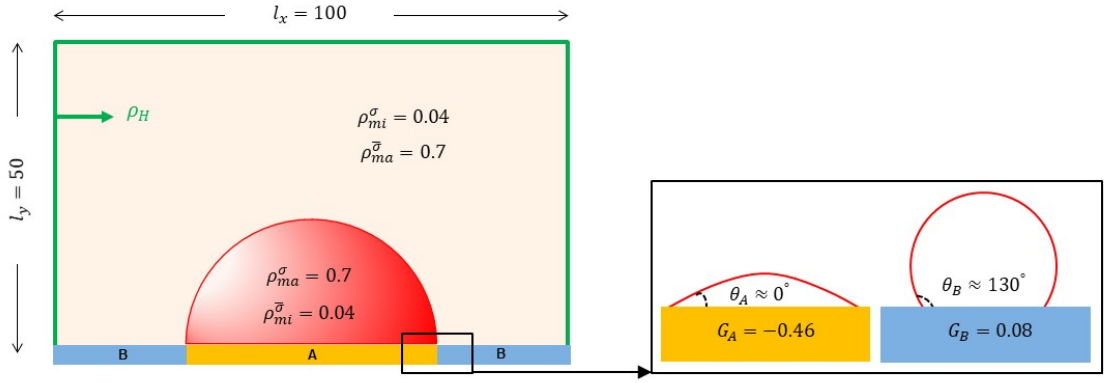

Figure 3.2: Schematic of the simulation domain.

3.3.1 Velocity field inside a pure droplet during evaporation

We first simulate the evaporation of a pure droplet with a pinned contact line to test the pseudopotential LBM. The simulation is conducted in a 3-D domain of $101 \times 101 \times 51$. For the equilibration process, we use the periodic boundary conditions for all boundaries except for the bottom substrate. The substrate is assumed to be chemically patterned such that the hydrophilic $\theta_A \simeq 0^{\circ}$ circle is imposed at the center of the simulation domain and surrounded by hydrophobic $\theta_B \simeq 130^{\circ}$ area, as illustrated in Fig. 3.2. The initial conditions of the droplet are set to be the contact radius of $R_0 = 40$ with the initial contact angle of $\theta_0 \simeq 90^{\circ}$, and the densities of $\rho^{\sigma}_{max} = \rho^{\bar{\sigma}}_{min} = 0.7$ and $\rho^{\sigma}_{min} = \rho^{\bar{\sigma}}_{max} = 0.04$. The interaction parameter in Eq. 3.6 is set to $G^{\sigma\bar{\sigma}} = 2.8$. After equilibration, we obtain the equilibrium densities of $\rho^{\sigma}_{max} \approx 0.64$ and $\rho^{\sigma}_{min} \approx 0.12$. Then we carry out the simulation for the evaporation of the droplet. For this, we imposed $\rho_H = 0$ at all boundaries of the computation domain except the bottom. At bottom, the wall boundary condition is imposed.

By assuming that the evaporation of the droplet is in a quasi-steady state and dominated by the density gradient of the surrounding fluid, the surrounding fluid density ρ^{σ} satisfies the Laplace equation,

$$\triangle \rho^{\sigma} = 0, \tag{3.27}$$

with the boundary conditions that the vapor is saturated at the constant concentration

of $\rho^\sigma = \rho_H$. Since this boundary value problem is mathematically equivalent to the electrostatic problem of a charged conductor, several researchers derived the formulas and solved for ρ^σ. Thus, an equation describing the contact angle evolution of the droplet with the constant contact radius mode can be derived as [11],

$$\frac{d\theta}{dt} = -\frac{D(\rho^\sigma_{mi} - \rho_H)}{\rho^\sigma_{ma} R_0^2} g(\theta), \tag{3.28}$$

where the function $g = g(\theta)$ is defined by:

$$g(\theta) = (1+\cos\theta)^2 \{\tan\frac{\theta}{2} + 8\int_0^\infty \frac{\cosh^2\theta\tau}{\sinh 2\pi\tau}\tanh[\tau(\pi-\theta)]d\tau\}. \tag{3.29}$$

To apply this equation to the multicomponent pseudopotential model, we use the diffusion coefficient D is given as [91]:

$$D = \left[c_s^2(\tau^\sigma - \frac{1}{2}) - \frac{c_s^2}{\rho^\sigma + \rho^{\bar{\sigma}}}(\rho^{\bar{\sigma}}\psi^\sigma G^{\sigma\bar{\sigma}}\psi'^{\bar{\sigma}} + \rho^\sigma\psi^{\bar{\sigma}}G^{\bar{\sigma}\sigma}\psi'^{\sigma})\right]. \tag{3.30}$$

To obtain the temporal evolution of θ, we integrate numerically Eq. 3.28 using the Runge-Kutta method.

Fig. 3.3 shows the comparison between the simulation result from pseudopotential model and the analytic solution from solving the Eq. 3.28. The solid line indicates the analytic solution and the symbols correspond to the results of LB simulation. In the figure, we can observe that the magnitude of the slope of the analytic solution increases as evaporation proceeds and that our simulation matches with the analytic solution until $t = 0.9t_f$. During the last 10% of the lifetime, depinning of the contact line occurs due to large surface tension at the contact line which leads small discrepancy between simulation data and the analytic solution.

Here, a typical outward velocity field in a droplet during evaporation is obtained and also compared with the analytical solutions. Fig. 3.4a and Fig. 3.4b illustrate the streamline and the outward flow of evaporative droplet, respectively.

To quantitatively compare the flow field with the analytical solution, we plot the radial and vertical velocities corresponding to the height of the droplet [35]. For the

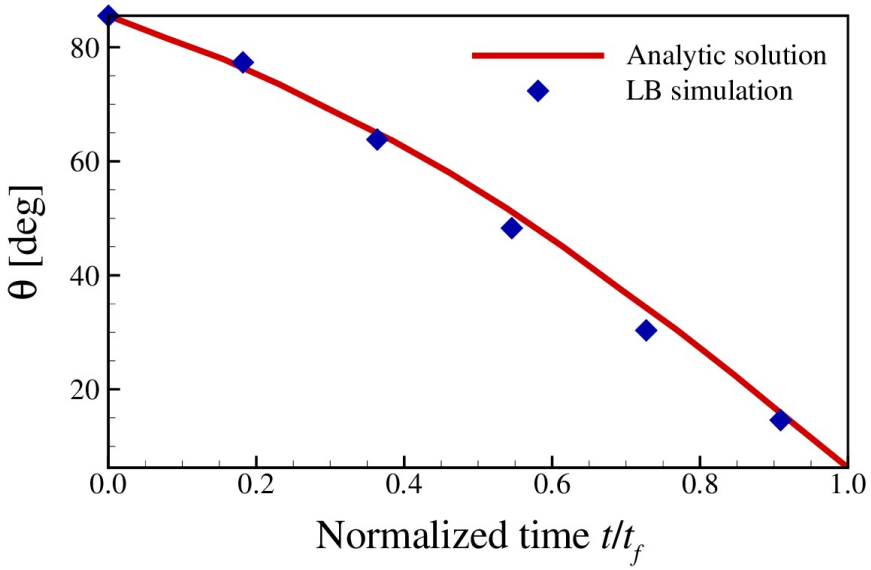

Figure 3.3: The evolution of the contact angle during evaporation in a constant contact radius mode is plotted as a function of normalized time t/t_f where t_f is the lifetime of the droplet in evaporation. The solid line indicates analytic solution obtained by Eq.3.28 and the symbols correspond to the results of LB simulation.

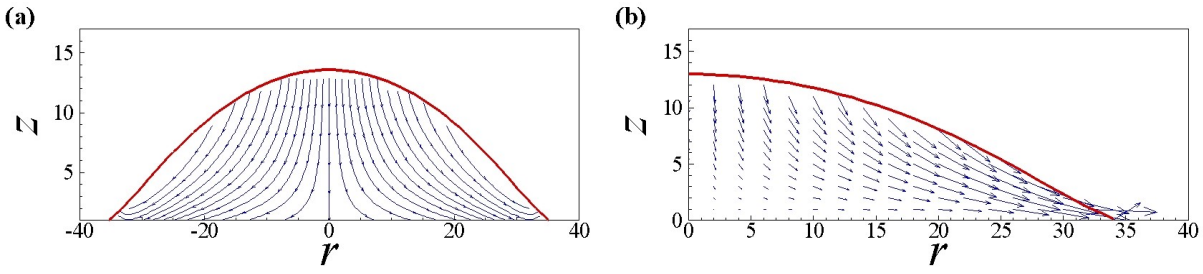

Figure 3.4: LB simulation results at the contact angle of $40°(t = 0.6t_f)$. (a)Streamline and (b)vector field of the flow field for the right half of the droplet.

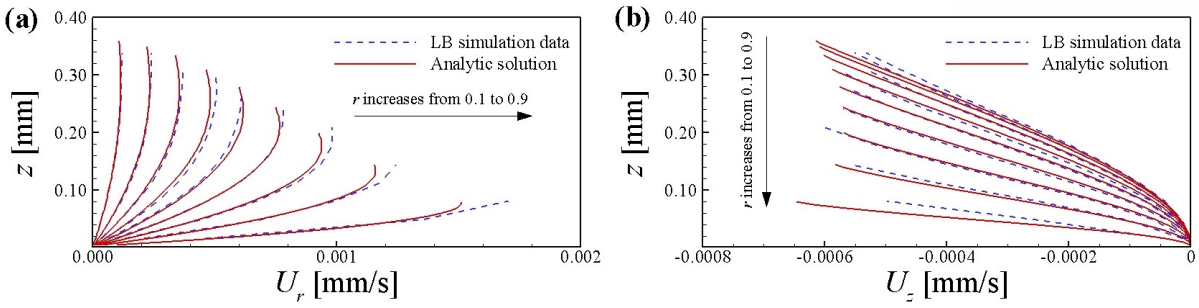

Figure 3.5: (a)Radial and (b)vertical velocity components according to the droplet height at 10 different radial positions from 0.1mm to 0.9mm at a contact angle of 40°. The solid lines correspond to the analytic solution and the dashed lines correspond to the LB solution.

comparison, we convert the LB units to the physical system units using the characteristic droplet radius of 1 mm and the time scale of evaporation, 6 min. As shown in Fig.3.5, our simulation results are consistent with the analytic solution. The simulation data of vertical velocity (Fig.3.5b) shows lower consistency with the analytic solution than that of radial velocity (Fig.3.5a). This discrepancy comes from the spurious current [92, 93] which is a small vortex generated near the interface. In our simulation, the magnitude of spurious current is approximately 1×10^{-4} mm/s near the interface which is comparable to the vertical velocity.

3.3.2 Deposition patterns of colloidal particles in an evaporating droplet

In this section, we simulate the evaporation of a droplet containing colloids with a pinned contact line. Unlike the previous result, the simulation is performed in a 2-dimensional domain, size of 301×151. During equilibration process, periodic boundary conditions are imposed at the top, left, and right boundaries and at the bottom substrate the wall boundary condition is given. The substrate is chemically patterned, where the hydrophilic ($\theta_A \simeq 0°$) substrate is imposed at the center and surrounded by hydrophobic ($\theta_B \simeq 130°$) area, similar to the schematic of Fig. 3.2. The initial conditions of the droplet are set as follows: the contact radius is $R_0 = 100$ with the contact angle $\theta_0 \simeq 90°$, and the densities

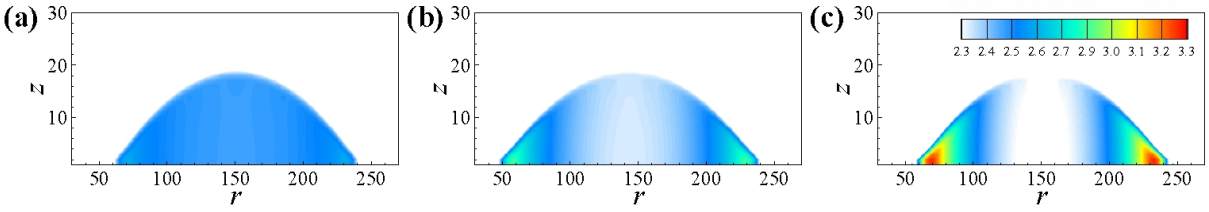

Figure 3.6: Particle density distribution for various Peclet numbers: (a)$Pe = 0.4$, (b)$Pe = 1.5$ and (c)$Pe = 3$.

of $\rho^{\sigma}_{ma} = \rho^{\bar{\sigma}}_{mi} = 0.7$ and $\rho^{\sigma}_{mi} = \rho^{\bar{\sigma}}_{ma} = 0.04$. The interaction parameter in Eq. 3.6 is set to $G^{\sigma\bar{\sigma}} = 2.8$. The initial density of the colloid particles is $C = 0.5$ within the droplet, and the density outside of the droplet is $C = 0.01$. After equilibration, we obtain the equilibrium densities of $\rho^{\sigma}_{ma} \approx 0.64$ and $\rho^{\sigma}_{mi} \approx 0.12$.

The particle density distribution corresponding to the various Peclet number (Pe) is obtained, which is the ratio of the rate of convection to diffusion of particles. That is, the Peclet number in our simulation is defined as follows

$$Pe = \frac{R_0 v_c}{D^c}, \tag{3.31}$$

where v_c is the characteristic velocity and the diffusion coefficient for the colloidal particle, D^c, is given by Eq. 3.24 in Section 3.2.3. Note that the characteristic velocity v_c depends on the evaporation rate which depends on the evaporation boundary density ρ_H. In our simulation, the characteristic velocity is varied from 0.001 to 0.003 according to the boundary density of $\rho_H = 0.07$ to 10^{-5}. In addition, we change the diffusion coefficient from 0.1 to 0.23 by changing the relaxation parameter τ from 0.8 to 1.2.

Fig. 3.6 shows the density distribution of particle at the contact angle of 25°. In the simulation, we observed the particle deposition pattern in the vicinity of the contact line for three different Peclet numbers of 0.4, 1.5, and 3.

In Fig. 3.6a of the low value Pe, density distribution is relatively homogeneous because the particle is primarily driven by the density gradient of the particle. As the Peclet number increases, however, the convective particle motion predominates, which leads particles to be accumulated near the contact line (known as the “coffee-ring” phe-

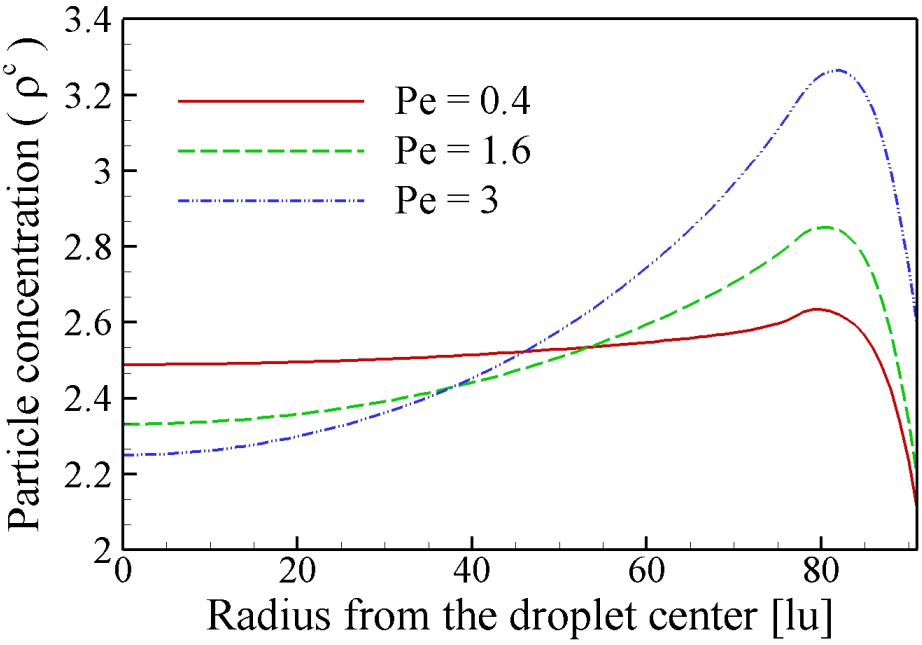

Figure 3.7: Deposition profiles for various Peclet numbers.

nomenon). From Fig. 3.6b-c, it is readily observed that particles are more accumulated at the droplet edge and the concentration at the edge increases with increasing Pe. It is also shown in Fig. 3.7, where the density distribution is plotted for a right half of the droplet.

3.4 Conclusions

In this paper, we develop the LB model to simulate the dynamics of colloids in an evaporating droplet with a fixed contact line. We implement the pseudopotential lattice Boltzmann model, which is a popular method to simulate multi-phase and multi-component fluids. The evaporation is caused by the density gradient of fluid surrounding the droplet. Since the contact line is fixed by the local force balance, we used the chemically patterned substrate to generate the unbalanced Young's force at the hydrophobic-hydrophilic boundary of the substrate. The local Young's force at the contact line maintains the contact line to be pinned. Then we propose a novel LB model to simulate the movements of colloids in a drying droplet. We consider the colloidal particles as the macroscopic

fluid model rather than a particle-based model. Using the LB model, hence, we solve the advection-diffusion equation for colloid within the droplet. To retain colloids inside the droplet, we impose the external force to the particle distribution function at the interface of the droplet with a similar formulation to the interaction force of the pseudopotential lattice Boltzmann model.

The simulation results show the applicability of the novel LB model: First, we simulate the evaporation of a droplet with the fixed contact line and compare the evolution with the analytic solutions. The flow field inside the droplet and the contact angle evolution are found to agree well with the analytical results. Second, we compare the deposition patterns in a droplet with various Peclet numbers. We show three different deposition patterns with the Peclet numbers: $Pe = 0.4, 1.5$ and 3. Since the large Pe indicates the dominance of the convective motion of particles over diffusion, we observe the high concentration of colloids near the droplet edge when $Pe = 3$. Accordingly, when $Pe = 0.4$, the concentration distribution of colloids is relatively homogenous in the droplet. Our new model can be used for simulating the intricate system of a drying droplet with colloids and surfactant in unified way in context of the lattice Boltzmann simulations.

Chapter IV

Two-dimensional characteristic boundary conditions for open boundaries in the lattice Boltzmann method

4.1 Introduction

In this chapter, the improved characteristic boundary conditions are implemented to the Lattice Boltzmann method, then applied to comprehensive test problems, including single vortex-convection and vortex shedding problem. Open boundary conditions (BC) have been an active research topic due to their importance to obtain accurate and stable solutions in the conventional computational fluid dynamics (CFD) simulations. Since open boundaries are introduced by truncating a physical domain, they may cause unrealistic solution behavior such as acoustic wave reflections at the boundaries, thereby deteriorating the accuracy and stability of interior solutions. In the CFD community, the characteristic boundary conditions (CBC) for compressible flows have been regarded as one of the most common techniques to resolve the reflections at open boundaries [33, 34, 94–98]. In general, the amplitudes of incoming waves determined from the characteristic analysis

are carefully specified such that their reflections at the open boundaries can be minimized in the CBC approaches.

Poinsot and Lele [94] developed the Navier-Stokes characteristic boundary conditions (NS-CBC), which are an extension of the CBC for the Euler equations by Thompson [95, 96] with viscous and diffusive conditions. To determine the incoming wave amplitudes at the open boundaries for the CBC, locally one-dimensional inviscid (LODI) flow is assumed by ignoring the transverse and viscous terms in the governing equations. Although the LODI assumption is adequate for many uni-directional flows, the conventional CBC based on it may become problematic when the ignored terms exhibit significant values at the boundaries: e.g. multi-dimensional flow problems. As a remedy for the conventional CBC, the improvement of the LODI relations was devised in [33, 34] by investigating the importance of the transverse and viscous terms in determining the incoming wave amplitudes and by incorporating a relaxation treatment of the transverse terms into them for outflows. The improved CBC were found to enhance the accuracy and stability of solutions by removing spurious solution behaviors at the boundaries. As a further extension, three-dimensional (3-D) CBC were proposed by Lodato et al. [98], in which the treatments of edges and corners in 3-D flows were included based on the improvement by Yoo and coworkers [33, 34].

In the lattice Boltzmann methods (LBM), most recent researches on the boundary conditions have focused on developing high-order boundary schemes for various configurations [29, 30], while little attention was paid on the treatment of spurious reflections at the open boundaries [31]. At the open boundaries, the amount of particles (populations), which may come into or reflect back to the computational domain, are pre-defined regardless of flow dynamics. In fact, the macroscopic values evaluated from the pre-defined incoming populations cannot be always compatible with those from the flow dynamics [29]. For instance, it was found from [31] that solutions with commonly-used LBM boundary conditions suffer from artificial reflections at the open boundaries. To overcome this problem, Izquierdo et al. [32] applied the conventional CBC to the LBM for non-reflecting open boundaries. Their results show better behavior than those from the conventional LBM boundary conditions [31]. However, the improvement is restricted to

the 1-D flow case; for the 2-D flow case of a vortex shedding, unphysical wave reflections are observed with the conventional CBC [32]. To resolve this problem, Heubes et al. [99] recently proposed new CBC by linearly combining the incoming wave amplitudes determined by Thompson's method and the LODI relations. Considering the recent developments of the CBC [33, 34, 97, 98] for solving compressible Navier-Stokes equation, however, there still remains a room to re-examine the accuracy of the LBM-CBC; the restricted one-dimensional assumption of the LODI can be released by recovering the ignored terms in the process of the characteristic analysis [33, 34].

It is of importance to note that the absorbing BC are another common approach for open boundaries. This method was originally developed by Berenger based on the perfectly matched layer (PML) to solve the Maxwell's equations, and applied to many other fields including the aero-acoustics [100–102]. Recently, Najafi-Yazdi and Mongeau introduced the absorbing boundary conditions to LBM simulations [103]; within the PML region, the lattice Boltzmann equations for acoustic distribution functions are modified with additional damping terms. The stability of the PML formulation is ensured based on the analysis of Becache et al. [104], and its accuracy can be improved with the thickness of the PML. It is also of interest to note that the comparison between the CBC and PML was made in the framework of the LBM [105], from which the absorbing BC based on the PML was found to perform better than the CBC. In this comparison, however, the conventional CBC were used and, as such, the recent improvement of the CBC has not been fully appreciated.

The objective of the present study is, therefore, to introduce the improved and generalized CBC to the LBM community and to discuss the importance of the CBC in the LBM simulations. In the following sections, an isothermal LBM with the D2Q9 model is introduced and the open boundary conditions are discussed in the context of two-dimensional (2-D) CBC.

4.2 Model

4.2.1 Lattice Boltzmann method

4.2.1.1 D2Q9 multi-relaxation-time lattice Boltzmann model

Instead of the lattice BGK (LBGK) model, a multi-relaxation-time (MRT) collision operator is adopted to increase the accuracy of the boundary conditions [106]. The MRT-LBM is an extension of the LBGK model, allowing multi-relaxation times of various modes after the collision step such that the MRT model can enhance the numerical stability of the solutions [106]. The evolution of the distribution function vector, $\mathbf{f}$, in the MRT-LBM is expressed as:

$$\mathbf{f}(\mathbf{x}+\mathbf{e}\Delta t, t+\Delta t) - \mathbf{f}(\mathbf{x}, t) = -\mathbf{M}^{-1}\hat{\mathbf{S}}[\mathbf{m}(\mathbf{x}, t) - \mathbf{m}^{eq}(\mathbf{x}, t)]. \tag{4.1}$$

The corresponding relaxation times, $\hat{\mathbf{S}}$, modes, $\mathbf{m}$, and equilibrium modes, $\mathbf{m}^{eq}$, are given by:

$$\begin{aligned}
\hat{\mathbf{S}} =& \text{diag}(0, s_e, s_\epsilon, 0, s_q, 0, s_q, s_\nu, s_\nu), \\
\mathbf{m} =& (\rho, e, \epsilon, \rho u, q_x, \rho v, q_y, p_{xx}, p_{yy})^T, \\
\mathbf{m}^{eq} =& (\rho, -2\rho + 3\rho_0(u^2+v^2), \rho - 3\rho_0(u^2+v^2), \\
& \rho_0 u, -\rho_0 u, \rho_0 v, -\rho_0 v, \rho_0(u^2-v^2), \rho_0 uv)^T,
\end{aligned} \tag{4.2}$$

where ρ is the mass density, ρ_0 is the initial mass density, and $\mathbf{u} = (u, v)$ is the flow velocity vector. A 9×9 transformation matrix $\mathbf{M}$ in [106] is used. The transport coefficients are related to the relaxation factors, and therefore the shear and bulk viscosity are obtained, respectively,

$$\nu = \frac{1}{3} = \left(\frac{1}{s_\nu} - \frac{1}{2}\right), \tag{4.3}$$

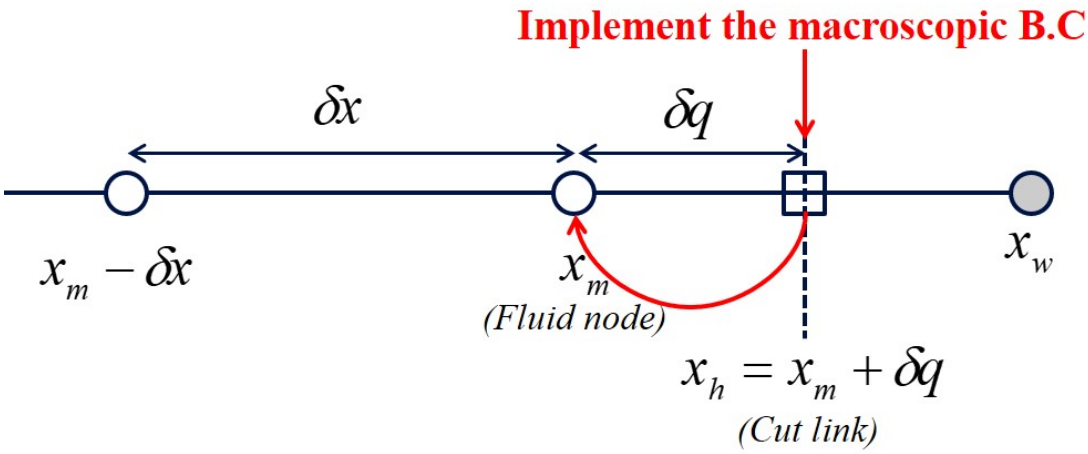

Figure 4.1: A schematic description of the multi reflection boundary condition

and

$$\xi = \frac{2-\kappa}{6} = \left(\frac{1}{s_e} - \frac{1}{2}\right). \tag{4.4}$$

4.2.1.2 Dirichlet boundary conditions of LBM

To apply the CBC to the MRT-LBM, the boundary conditions proposed by Ginzburg et al. [29] are adopted. A 2-D domain of $0 \leq x \leq l_x$ and $0 \leq y \leq l_y$ is discretized by $m \times n$ nodes in which three different types of nodes, $\mathbf{x_k} = (x_k, y_{k'})$, need to be defined: (1) fluid nodes represent the nodes inside the computation domain where $k = 2, \cdots, m-1$ and $k' = 2, \cdots, n-1$, (2) boundary nodes, $\mathbf{x_b}$, denote the nodes, at least one of which neighbor node is not a fluid node where $k = 1, m$ or $k' = 1, n$, and (3) cutlinks, $\mathbf{x_c}$, are the nodes between a boundary node and an outside one where $k = 1 - \delta q, m + \delta q$, or $k' = 1 - \delta q, n + \delta q$, and $0 < \delta q < 1$. In the present study, $\delta q = 1/2$ is adopted such that the boundary conditions have the second-order accuracy.

4.2.1.2.1 Pressure/velocity conditions at inlet/outlet

In the LBM, the Dirichlet boundary condition for pressure is often used at the outlets in which the incoming probability distribution function $f_{\bar{i}}(x_m, y_{k'}, t)$ can be determined by using the outgoing $f_i(x_m, y_{k'}, t)$. Note that $\bar{i}$ is the opposite direction of i. Using the pre-specified macroscopic variables $p(x_h, y_{k'}, t) = c_s^2 \rho(x_h, y_{k'}, t)$ at the outlet cutlink

($h = m + 1/2$, and $k' = 1, \cdots, n$), the boundary condition at $(x_m, y_{k'})$ for the next time step can be evaluated as [32]:

$$\begin{aligned} f_{\bar{i}}(x_m, y_{k'}, t+1) = &- \tilde{f}_i(x_m, y_{k'}, t) + 2f_i^{eq+}(x_h, y_{k'}, t) \\ &+ (2 - s_\nu)[f_i^+(x_m, y_{k'}, t) - f_i^{eq+}(x_m, y_{k'}, t)], \end{aligned} \tag{4.5}$$

where $\tilde{f}_i(x_m, y_{k'}, t)$ is the post-collision distribution function. f_i^+ and f_i^{eq+} are the symmetric parts of the distribution and the equilibrium distribution, respectively, calculated using the macroscopic quantities and the weights for different directions, ω_i:

$$\begin{aligned} f_i^+(x_m, y_{k'}, t) =& \frac{1}{2}(f_i(x_m, y_{k'}, t) + f_{\bar{i}}(x_m, y_{k'}, t)), \\ f_i^{eq+}(x_m, y_{k'}, t) =& \omega_i \rho(x_m, y_{k'}, t) \\ &+ \frac{9}{2}\omega_i \rho_0[(\mathbf{e}_i \cdot \mathbf{u}(x_m, y_{k'}, t))^2 - \frac{1}{3}(\mathbf{u}(x_m, y_{k'}, t) \cdot \mathbf{u}(x_m, y_{k'}, t))], \\ f_i^{eq+}(x_h, y_{k'}, t) =& \omega_i \rho(x_h, y_{k'}, t) \\ &+ \frac{9}{2}\omega_i \rho_0[(\mathbf{e}_i \cdot \mathbf{u}(x_h, y_{k'}, t))^2 - \frac{1}{3}(\mathbf{u}(x_h, y_{k'}, t) \cdot \mathbf{u}(x_h, y_{k'}, t))], \end{aligned} \tag{4.6}$$

where $\omega_0 = 4/9$, $\omega_{1\sim4} = 1/9$, and $\omega_{5\sim9} = 1/36$ in the D2Q9 model.

For the Dirichlet boundary conditions for the LBM, constant $p(x_h, y_{k'}, t) = p_0$ and/or $\mathbf{u}(x_h, y_{k'}, t) = \mathbf{u}_0$ are often applied and as such, it may cause spurious flow behavior at the open boundaries. In the present study, instead, $p(x_h, y_{k'}, t)$ and $\mathbf{u}(x_h, y_{k'}, t)$ are evaluated at each time step by solving their evolution equations derived from the 2-D CBC, which will be explained in the next section.

In the same way, the Dirichlet boundary condition for the velocity is given at the inlet $(x_1, y_{k'})$, where $k' = 1, \cdots, n$ as:

$$f_{\bar{i}}(x_1, y_{k'}, t+1) = \tilde{f}_i(x_1, y_{k'}, t) - 2f_i^{eq-}(x_h, y_{k'}, t), \tag{4.7}$$

where $h = 1/2$ at the left cutlink and $f_i^{eq-}(x_h, y_{k'}, t) = 3\omega_i \rho_0(\mathbf{e}_i \cdot \mathbf{u}(x_h, y_{k'}, t))$. The

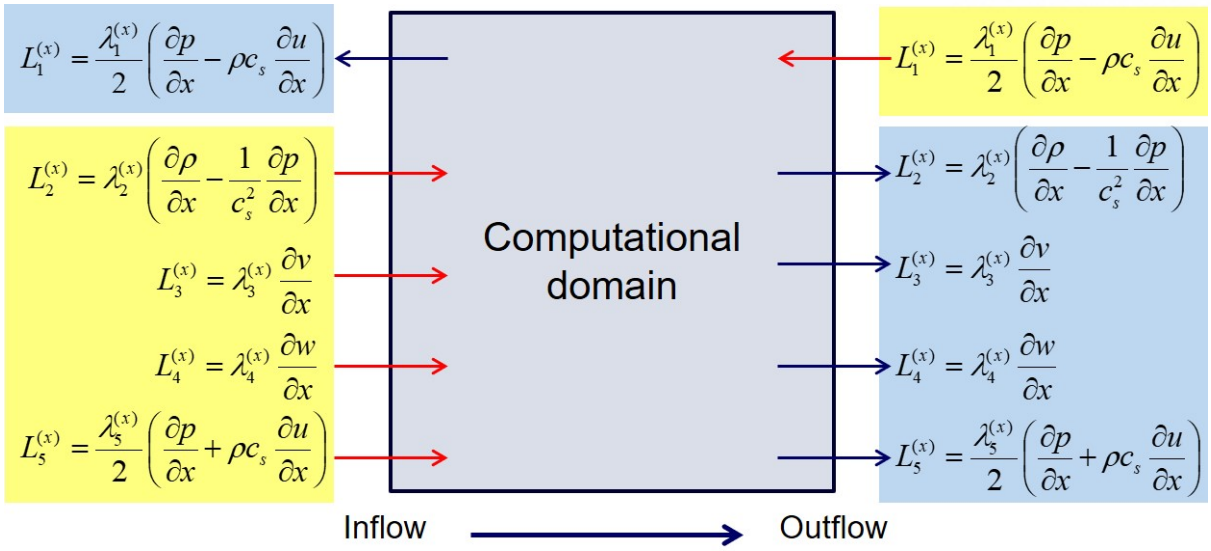

Figure 4.2: A schematic description of the wave amplitude variations for boundaries

temporal evolution of $\mathbf{u}(x_h, y_{k'}, t)$ can also be determined from their evolution equations derived from the 2-D CBC.

4.2.2 General formulation of the CBC

In this section, the improved CBC are revisited to determine the evolution equations of the macroscopic values, $p(\mathbf{x_c}, t)$ and $\mathbf{u}(\mathbf{x_c}, t)$, at the cutlinks for the D2Q9 isothermal LBM. For the general description of the improved CBC, a 3-D domain of $0 \leq x \leq l_x$, $0 \leq y \leq l_y$, and $0 \leq z \leq l_z$ is considered here. It should be noted that the characteristic inlet/outlet conditions are applied at the cutlinks ($x = 0 - \delta x$ or $x = l_x + \delta x$) to compute the microscopic boundary conditions, for example, at $x = 0$ or $x = l_x$. Based on the 1-D characteristic analysis in the $x-$direction, different waves crossing the boundaries (on the $yz-$plane) can be decomposed into 1-D characteristic waves with the amplitudes of $\mathcal{L}_i^{(x)}$. The Navier-Stokes (NS) equations is then given in non-conservative form as:

$$\frac{\partial}{\partial t}\begin{bmatrix} u \\ v \\ w \\ \rho \\ p \end{bmatrix} + \begin{bmatrix} \frac{1}{\rho c_s}(\mathcal{L}_5^{(x)} - \mathcal{L}_1^{(x)}) \\ \mathcal{L}_3^{(x)} \\ \mathcal{L}_4^{(x)} \\ \mathcal{L}_2^{(x)} + \frac{1}{c_s^2}(\mathcal{L}_5^{(x)} + \mathcal{L}_1^{(x)}) \\ \mathcal{L}_5^{(x)} + \mathcal{L}_1^{(x)} \end{bmatrix} + \begin{bmatrix} \mathbf{u}_t \cdot \bigtriangledown_t u \\ \mathbf{u}_t \cdot \bigtriangledown_t v + \frac{1}{\rho}\frac{\partial p}{\partial y} \\ \mathbf{u}_t \cdot \bigtriangledown_t w + \frac{1}{\rho}\frac{\partial p}{\partial z} \\ \bigtriangledown_t \cdot (\rho \mathbf{u}_t) \\ \mathbf{u}_t \cdot \bigtriangledown_t p + \gamma p \bigtriangledown_t \cdot \mathbf{u}_t \end{bmatrix} = \begin{bmatrix} d_u \\ d_v \\ d_w \\ d_\rho \\ d_p \end{bmatrix}, \tag{4.8}$$

where t represents tangential ($y-$ and $z-$) directions, $c_s = \sqrt{\gamma RT}$ is the speed of sound, $\gamma = 1$ is the specific heat ratio in the D2Q9 model, and $\mathbf{u} = (u, v, w)$ is the velocity vector. The wave amplitudes $\mathcal{L}_i^{(x)}$ are defined as [33, 34, 94]:

$$\begin{bmatrix} \mathcal{L}_1^{(x)} \\ \mathcal{L}_2^{(x)} \\ \mathcal{L}_3^{(x)} \\ \mathcal{L}_4^{(x)} \\ \mathcal{L}_5^{(x)} \end{bmatrix} = \begin{bmatrix} \frac{\lambda_1^{(x)}}{2}\left(\frac{\partial p}{\partial x} - \rho c_s \frac{\partial u}{\partial x}\right) \\ \lambda_2^{(x)}\left(\frac{\partial \rho}{\partial x} - \frac{1}{c_s^2}\frac{\partial p}{\partial x}\right) \\ \lambda_3^{(x)}\frac{\partial v}{\partial x} \\ \lambda_4^{(x)}\frac{\partial w}{\partial x} \\ \frac{\lambda_5^{(x)}}{2}\left(\frac{\partial p}{\partial x} + \rho c_s \frac{\partial u}{\partial x}\right) \end{bmatrix}, \tag{4.9}$$

where $\lambda_k^{(x)}$ are the characteristic velocities:

$$\lambda_1^{(x)} = u - c_s, \quad \lambda_2^{(x)} = \lambda_3^{(x)} = \lambda_4^{(x)} = u, \quad \lambda_5^{(x)} = u + c_s. \tag{4.10}$$

The viscous terms are given by:

$$\begin{bmatrix} d_u \\ d_v \\ d_w \\ d_\rho \\ d_p \end{bmatrix} = \begin{bmatrix} (1/\rho)\nabla_j \cdot \tau_{j1} \\ (1/\rho)\nabla_j \cdot \tau_{j2} \\ (1/\rho)\nabla_j \cdot \tau_{j3} \\ 0 \\ (\gamma - 1)\tau_{jk} : \nabla_j u_k \end{bmatrix}, \tag{4.11}$$

where τ_{ji} is the stress tensor defined by:

$$\tau_{ji} = \mu \left(\frac{\partial u_j}{\partial x_i} + \frac{\partial u_i}{\partial x_j} - \frac{2}{3}\delta_{ji}\frac{\partial u_k}{\partial x_k} \right), \tag{4.12}$$

and μ is the dynamic viscosity, and the lower indices are the indices of coordinates: e.g. (x_1, x_2, x_3) is equivalent to (x, y, z).

In the CBC, it is more convenient to define the incoming wave variations in characteristic form. At the $x-$direction boundaries, Eq. 4.8 can be transformed as:

$$\begin{bmatrix} \frac{1}{2}\left(\frac{\partial p}{\partial t} - \rho c_s \frac{\partial u}{\partial t}\right) \\ \frac{\partial \rho}{\partial t} - \frac{1}{c_s^2}\frac{\partial p}{\partial t} \\ \frac{\partial v}{\partial t} \\ \frac{\partial w}{\partial t} \\ \frac{1}{2}\left(\frac{\partial p}{\partial t} + \rho c_s \frac{\partial u}{\partial t}\right) \end{bmatrix} + \begin{bmatrix} \mathcal{L}_1^{(x)} \\ \mathcal{L}_2^{(x)} \\ \mathcal{L}_3^{(x)} \\ \mathcal{L}_4^{(x)} \\ \mathcal{L}_5^{(x)} \end{bmatrix} = \begin{bmatrix} \mathcal{T}_1^{(x)} \\ \mathcal{T}_2^{(x)} \\ \mathcal{T}_3^{(x)} \\ \mathcal{T}_4^{(x)} \\ \mathcal{T}_5^{(x)} \end{bmatrix} + \begin{bmatrix} \mathcal{V}_1^{(x)} \\ \mathcal{V}_2^{(x)} \\ \mathcal{V}_3^{(x)} \\ \mathcal{V}_4^{(x)} \\ \mathcal{V}_5^{(x)} \end{bmatrix}, \tag{4.13}$$

where $\mathcal{T}_i^{(x)}$ and $\mathcal{V}_i^{(x)}$ are the transverse and viscous terms, respectively, defined by:

$$\begin{bmatrix} \mathcal{T}_1^{(x)} \\ \mathcal{T}_2^{(x)} \\ \mathcal{T}_3^{(x)} \\ \mathcal{T}_4^{(x)} \\ \mathcal{T}_5^{(x)} \end{bmatrix} = \begin{bmatrix} -\frac{1}{2}\left(\mathbf{u}_t \cdot \bigtriangledown_t p + \gamma p \bigtriangledown_t \cdot \mathbf{u}_t - \rho c_s \mathbf{u}_t \cdot \bigtriangledown_t u\right) \\ -\bigtriangledown_t \cdot (\rho \mathbf{u}_t) + \frac{1}{c_s^2}(\mathbf{u}_t \cdot \bigtriangledown_t p + \gamma p \bigtriangledown_t \cdot \mathbf{u}_t) \\ -\left(\mathbf{u}_t \cdot \bigtriangledown_t v + \frac{1}{\rho}\frac{\partial p}{\partial y}\right) \\ -\left(\mathbf{u}_t \cdot \bigtriangledown_t w + \frac{1}{\rho}\frac{\partial p}{\partial z}\right) \\ -\frac{1}{2}\left(\mathbf{u}_t \cdot \bigtriangledown_t p + \gamma p \bigtriangledown_t \cdot \mathbf{u}_t + \rho c_s \mathbf{u}_t \cdot \bigtriangledown_t u\right) \end{bmatrix}, \tag{4.14}$$

and

$$\begin{bmatrix} \mathcal{V}_1^{(x)} \\ \mathcal{V}_2^{(x)} \\ \mathcal{V}_3^{(x)} \\ \mathcal{V}_4^{(x)} \\ \mathcal{V}_5^{(x)} \end{bmatrix} = \begin{bmatrix} \frac{1}{2}\left(d_p - \rho c_s d_u\right) \\ d_\rho - \frac{1}{c_s^2} d_p \\ d_v \\ d_w \\ \frac{1}{2}\left(d_p + \rho c_s d_u\right) \end{bmatrix}. \tag{4.15}$$

For subsonic flows with $0 \leq u < c_s$, the wave corresponding to $\mathcal{L}_1^{(x)}$ comes into the computational domain and the other waves represented by $\mathcal{L}_2^{(x)} \sim \mathcal{L}_5^{(x)}$ are outgoing at the outflow cutlink ($x = l_x + \delta x$). As such, $\mathcal{L}_i^{(x)}$ of the outgoing waves can be simply calculated using one-sided differences of Eq. 4.9 with the interior information. However, additional physical information must be provided to determine $\mathcal{L}_1^{(x)}$ of the incoming wave. The physical boundary condition such as far-field pressure (p_∞) condition can be properly used for this purpose.

For example, a simple-relaxation boundary condition for pressure has been used to determine $\mathcal{L}_1^{(x)}$ in the conventional CBC [94]. At $x = l_x + \delta x$, the incoming wave amplitude $\mathcal{L}_1^{(x)}$ is approximated by:

$$\mathcal{L}_1^{(x)} = \alpha_1(p - p_\infty), \tag{4.16}$$

where p_∞ is the target pressure at $x = l_x + \delta x$ and α_1 is the relaxation coefficient for pressure, which is given as $\alpha_1 = \sigma_1(1 - Ma^2)c_s/2l_x$. Ma is the maximum Mach number at the boundary and σ_1 is a relaxation constant. When $\sigma_1 = 0$, it becomes a perfectly non-reflecting boundary condition but the boundary pressure may drift because the pressure relaxation term cannot maintain it at p_∞. On the contrary, it approaches asymptotically the Dirichlet pressure condition, $p = p_\infty$, as σ_1 increases from zero to infinity. The proper choices of the relaxation coefficients are essential for the successful control of the wave reflection [33]. In summary, all of the wave amplitudes at the outflow boundary ($x = l_x + \delta x$) are determined by:

$$\begin{cases} \mathcal{L}_1^{(x)} = \alpha_1(p - p_\infty), \\ \\ \mathcal{L}_{2,\cdots,5}^{(x)} = \text{from Eq. (4.9)}. \end{cases} \tag{4.17}$$

In the same way, $\mathcal{L}_2^{(x)}$, $\cdots$, $\mathcal{L}_5^{(x)}$ of the incoming waves are specified using prescribed macroscopic variables at the inflow boundary ($x = -\delta x$) which are given by [33, 94]:

$$\begin{cases} \mathcal{L}_1^{(x)} = \text{from Eq. (4.9)}, \\ \\ \mathcal{L}_2^{(x)} = \beta_2(T - T_0), \\ \\ \mathcal{L}_3^{(x)} = \beta_3(v - v_0), \\ \\ \mathcal{L}_4^{(x)} = \beta_4(w - w_0), \\ \\ \mathcal{L}_5^{(x)} = \beta_5(u - u_0), \end{cases} \tag{4.18}$$

where β_i are the relaxation coefficients and the subscript 0 represents their corresponding target values [33]. The wave amplitudes in the other directions can also be determined in the same manner. Once all of $\mathcal{L}_i$ are determined at all of the boundaries, the boundary

solutions of the primitive variables ($\mathbf{u}$, ρ, and p) are advanced in time using Eq. 4.8 to determine their values at the next time step, which are eventually used to solve their interior solution.

In the conventional CBC [94], the transverse and viscous terms are ignored based on the LODI assumption at the open boundaries. As such, the relaxation terms in Eqs. 4.17 and 4.18 are supposed to render the boundary solutions to converge into desired target values in the steady limit of the flow, especially when the LODI assumption is valid at the boundaries. However, when the flows are strongly multi-directional as in the counterflow configuration or strong turbulence passes through the open boundaries, the conventional CBC with simple relaxations can cause spurious and unstable solution behaviors due to nonzero transverse and viscous terms at the boundaries [33,34,97,98]. To properly account for transverse and viscous terms in the boundary conditions, therefore, the original characteristic form of the NS equations must be considered:

$$\frac{\partial}{\partial t}\begin{bmatrix} u \\ v \\ w \\ \rho \\ p \end{bmatrix} + \begin{bmatrix} \frac{1}{\rho c_s}(\mathcal{L}_5^{(x)} - \mathcal{L}_1^{(x)}) \\ \mathcal{L}_3^{(x)} \\ \mathcal{L}_4^{(x)} \\ \mathcal{L}_2^{(x)} + \frac{1}{c_s^2}(\mathcal{L}_5^{(x)} + \mathcal{L}_1^{(x)}) \\ \mathcal{L}_5^{(x)} + \mathcal{L}_1^{(x)} \end{bmatrix} = \begin{bmatrix} \frac{1}{\rho c_s}(\mathcal{T}_5^{(x)} - \mathcal{T}_1^{(x)}) \\ \mathcal{T}_3^{(x)} \\ \mathcal{T}_4^{(x)} \\ \mathcal{T}_2^{(x)} + \frac{1}{c_s^2}(\mathcal{T}_5^{(x)} + \mathcal{T}_1^{(x)}) \\ \mathcal{T}_5^{(x)} + \mathcal{T}_1^{(x)} \end{bmatrix} + \begin{bmatrix} \frac{1}{\rho c_s}(\mathcal{V}_5^{(x)} - \mathcal{V}_1^{(x)}) \\ \mathcal{V}_3^{(x)} \\ \mathcal{V}_4^{(x)} \\ \mathcal{V}_2^{(x)} + \frac{1}{c_s^2}(\mathcal{V}_5^{(x)} + \mathcal{V}_1^{(x)}) \\ \mathcal{V}_5^{(x)} + \mathcal{V}_1^{(x)} \end{bmatrix} \tag{4.19}$$

At the inflow boundaries, the effects of transverse and viscous terms can effectively be removed from the boundary solutions by including $\mathcal{T}_i^{(x)}$ and $\mathcal{V}_i^{(x)}$ in $\mathcal{L}_i^{(x)}$ of the incoming waves:

$$\begin{cases} \mathcal{L}_2^{(x)} = \beta_2(T - T_0) + \mathcal{T}_2^{(x)} + \mathcal{V}_2^{(x)}, \\ \mathcal{L}_3^{(x)} = \beta_3(v - v_0) + \mathcal{T}_3^{(x)} + \mathcal{V}_3^{(x)}, \\ \mathcal{L}_4^{(x)} = \beta_4(w - w_0) + \mathcal{T}_4^{(x)} + \mathcal{V}_4^{(x)}, \\ \mathcal{L}_5^{(x)} = \beta_5(u - u_0) + \mathcal{T}_5^{(x)} + \mathcal{V}_5^{(x)}, \end{cases} \tag{4.20}$$

and then, the effective inflow boundary conditions based on Eq. 4.19 become [33]:

$$\begin{cases} \dfrac{\partial \rho}{\partial t} - \dfrac{1}{c_s^2}\dfrac{\partial p}{\partial t} = -\beta_2(T - T_0), \\ \dfrac{\partial v}{\partial t} = -\beta_3(v - v_0), \\ \dfrac{\partial w}{\partial t} = -\beta_4(w - w_0), \\ \dfrac{1}{2}\left(\dfrac{\partial p}{\partial t} + \rho c_s \dfrac{\partial u}{\partial t}\right) = -\beta_5(u - u_0). \end{cases} \tag{4.21}$$

It is now clear from Eq. 4.21 that $\mathcal{T}_i^{(x)}$ and $\mathcal{V}_i^{(x)}$ are removed from the effective boundary conditions not by just ignoring them as in the conventional CBC but by including them in $\mathcal{L}_i^{(x)}$ and as such, the primitive variables can follow their target values regardless of $\mathcal{T}_i^{(x)}$ and $\mathcal{V}_i^{(x)}$. For evaluating $\mathcal{L}_1^{(x)}$ of the outgoing wave in Eq. 4.9 at the inlet, the derivatives are computed using a second-order forward difference approximation:

$$\frac{\partial \mathbf{u}}{\partial x}(x_h, y_{k'}, t) \approx \frac{1}{3}\left(-8\mathbf{u}(x_h, y_{k'}, t) + 9\mathbf{u}(\mathbf{x}_1, y_{k'}, t) - \mathbf{u}(\mathbf{x}_2, y_{k'}, t)\right). \tag{4.22}$$

At the outflow boundaries, a proper account of $\mathcal{T}_1^{(x)}$ and $\mathcal{V}_1^{(x)}$ in $\mathcal{L}_1^{(x)}$ with a relaxation treatment of $\mathcal{T}_1^{(x)}$ is needed to guarantee accurate and stable solution behavior at the outflow boundary such that $\mathcal{L}_1^{(x)}$ is given by [34]:

$$\mathcal{L}_1^{(x)} = \alpha_1^{(x)}(p - p_\infty) - a_1^{(x)}(\mathcal{T}_1^{(x)} - \mathcal{T}_{1,exact}^{(x)}) + \mathcal{T}_1^{(x)} + \mathcal{V}_1^{(x)}, \tag{4.23}$$

which leads to an effective outflow boundary condition:

$$\frac{1}{2}\left(\frac{\partial p}{\partial t} - \rho c_s \frac{\partial u}{\partial t}\right) = -\mathcal{L}_1^{(x)} + \mathcal{T}_1^{(x)} + \mathcal{V}_1^{(x)} = -\alpha_1^{(x)}(p - p_\infty) + a_1^{(x)}(\mathcal{T}_1^{(x)} - \mathcal{T}_{1,exact}^{(x)}), \quad (4.24)$$

where $\mathcal{T}_{1,exact}^{(x)}$ is the steady value of $\mathcal{T}_1^{(x)}$ and $a_1^{(x)}$ is the relaxation coefficient for the transverse term. It was found from the low-Mach number asymptotic analysis [34] that $a_1^{(x)}$ should be equal to the Mach number of the mean flow. For evaluating $\mathcal{L}_{2\sim5}^{(x)}$ of the outgoing waves in Eq. 4.9 at the outlet, the derivatives are computed using a second-order backward difference approximation:

$$\frac{\partial \mathbf{u}}{\partial x}(x_h, y_{k'}, t) \approx \frac{1}{3}\left(8\mathbf{u}(x_h, y_{k'}, t) - 9\mathbf{u}(\mathbf{x}_m, y_{k'}, t) + \mathbf{u}(\mathbf{x}_{m-1}, y_{k'}, t)\right). \quad (4.25)$$

It is of importance to note that for LBM, Eq. 4.19 is numerically advanced in time to obtain the primitive variables, $p(\mathbf{x_c}, t)$ and $\mathbf{u}(\mathbf{x_c}, t)$, in Eqs. 4.6 and 4.7 at the cutlinks (say, at $x = x_h$ in the $x-$direction). In addition, $\mathcal{L}_i^{(x)}$ in Eq. 4.19 should be determined by Eqs. 4.20 and 4.23.

4.3 Result and Discussion

4.3.1 Vortex convection problem

In this section, the importance of the inclusion of the transverse terms in $\mathcal{L}_1^{(x)}$ and their relaxation treatment at the outflow boundary is demonstrated by simulating a single-vortex convection problem with three different CBC for LBM. Note that at the inlet, flow distortion problem due to the transverse terms is not so critical especially in a uni-directional flow because most of the variables are specified as in Eq. 4.20. As such, we mainly focus on the interactions of the vortex convection with outflow boundary conditions. The initial velocity conditions for the single-vortex convection problem are specified as:

$$\begin{pmatrix} u \\ \\ v \end{pmatrix} = \begin{pmatrix} u_\infty \\ \\ 0 \end{pmatrix} + \begin{pmatrix} \dfrac{C}{\rho_\infty} \exp\left(-\dfrac{(x-x_0)^2+(y-y_0)^2}{2R_c^2}\right)\left(\dfrac{-(y-y_0)}{R_c^2}\right) \\ -\dfrac{C}{\rho_\infty} \exp\left(-\dfrac{(x-x_0)^2+(y-y_0)^2}{2R_c^2}\right)\left(\dfrac{-(x-x_0)}{R_c^2}\right) \end{pmatrix}, \tag{4.26}$$

such that the vortex is convected by a uniform free stream, where the subscript ∞ represents the free stream values. $C = 25c_s l_x/10^4$ is the vortex strength, $c_s = \sqrt{\gamma RT} = \sqrt{1/3}$ with $\gamma = 1$, and $R_c = l_x/10$ is the vortex radius. The free stream density is $\rho_\infty = c_s^2 p_\infty = 1/3$, and $(x_0, y_0) = (l_x/2, l_y/2)$ is the location of vortex center [34]. The domain consists of $m = 200$ and $n = 200$ grid points in the $x-$ and $y-$directions, respectively. The domain has dimensionless coordinates, $\widetilde{x} = x/m$ and $\widetilde{y} = y/n$, and a dimensionless time, $\widetilde{t} = t(c_s/m)$. The flow is characterized by a Mach number, $Ma = u_\infty/c_s = 0.05$, where u_∞ is the velocity of the uni-directional free stream. The relaxation times are specified as: $s_\nu = 1.8$, $s_e = s_\nu$, $s_\epsilon = s_\nu$, and $s_q = 8(2 - s_\nu)/(8 - s_\nu)$.

Since the isothermal D2Q9 MRT-LBM is adopted in this study, only u, v, and ρ are needed to be solved at the boundaries. As such, the evolution equations of Eq. 4.19 are restated as:

$$\frac{\partial}{\partial t}\begin{bmatrix} u \\ v \\ \rho \end{bmatrix} + \begin{bmatrix} \frac{1}{\rho c_s}(\mathcal{L}_5^{(x)} - \mathcal{L}_1^{(x)}) \\ \mathcal{L}_3^{(x)} \\ \frac{1}{c_s^2}(\mathcal{L}_5^{(x)} + \mathcal{L}_1^{(x)}) \end{bmatrix} = \begin{bmatrix} \frac{1}{\rho c_s}(\mathcal{T}_5^{(x)} - \mathcal{T}_1^{(x)}) \\ \mathcal{T}_3^{(x)} \\ \frac{1}{c_s^2}(\mathcal{T}_5^{(x)} + \mathcal{T}_1^{(x)}) \end{bmatrix} + \begin{bmatrix} \frac{1}{\rho c_s}(\mathcal{V}_5^{(x)} - \mathcal{V}_1^{(x)}) \\ \mathcal{V}_3^{(x)} \\ \frac{1}{c_s^2}(\mathcal{V}_5^{(x)} + \mathcal{V}_1^{(x)}) \end{bmatrix}. \quad (4.27)$$

At the outflow, $\mathcal{L}_1^{(x)}$ should be evaluated in different ways depending on three CBC:

- Case 1: $\mathcal{L}_1^{(x)} = \alpha_1^{(x)}(p - p_\infty)$, which corresponds to the outflow boundary condition of the conventional CBC [94]. The corresponding effective boundary condition is:

$$\frac{1}{2}\left(\frac{\partial p}{\partial t} - \rho c \frac{\partial u}{\partial t}\right) = -\mathcal{L}_1^{(x)} + \mathcal{T}_1^{(x)} + \mathcal{V}_1^{(x)} = -\alpha_1^{(x)}(p - p_\infty) + \mathcal{T}_1^{(x)} + \mathcal{V}_1^{(x)}. \quad (4.28)$$

- Case 2: $\mathcal{L}_1^{(x)} = \alpha_1^{(x)}(p - p_\infty) + \mathcal{T}_1^{(x)} + \mathcal{V}_1^{(x)}$, which is the CBC adopted in [32]. The corresponding effective outflow boundary condition becomes:

$$\frac{1}{2}\left(\frac{\partial p}{\partial t} - \rho c \frac{\partial u}{\partial t}\right) = -\mathcal{L}_1^{(x)} + \mathcal{T}_1^{(x)} + \mathcal{V}_1^{(x)} = -\alpha_1^{(x)}(p - p_\infty). \quad (4.29)$$

- Case 3: $\mathcal{L}_1^{(x)} = \alpha_1^{(x)}(p - p_\infty) - a_1^{(x)}(\mathcal{T}_1 - \mathcal{T}_{1,exact}^{(x)}) + \mathcal{T}_1^{(x)} + \mathcal{V}_1^{(x)}$, which corresponds to the outflow condition of the improved CBC [34]. The corresponding effective boundary condition is:

$$\frac{1}{2}\left(\frac{\partial p}{\partial t} - \rho c \frac{\partial u}{\partial t}\right) = -\mathcal{L}_1^{(x)} + \mathcal{T}_1^{(x)} + \mathcal{V}_1^{(x)} = -\alpha_1^{(x)}(p - p_\infty) + a_1^{(x)}(\mathcal{T}_1 - \mathcal{T}_{1,exact}). \quad (4.30)$$

For all of the three cases, $\sigma_1^{(x)} = 0.2$ is specified for $\alpha_1^{(x)} = \sigma_1^{(x)}(1 - Ma^2)c_s/2l_x$ and $a_1^{(x)} = Ma$ is used based on the low-Mach number asymptotic analysis [34]. For case 3, $\mathcal{T}_{1,exact}$ is zero by definition. The simple extrapolations are used for boundaries at

$y = 0 - \delta y$ and $y = l_y + \delta y$ to focus on the convection downstream by the mean flow in the $x-$direction. Note that the implementation of the treatments for edges and corners for 3-D CBC in [98] is straightforward such that it is not included here.

Fig .4.3 shows the isocontours of the $y-$directional velocities for Cases $1 \sim 3$ at four different times. From Case 1 where the conventional CBC is used, it is readily observed that the vortex is distorted while passing through the outlet due to the wave reflections generated by neglected transverse term. Even though the recovery of the ignored transverse terms in Case 2 improves the behavior by retaining the vortex shape longer, the flow distortion cannot be avoided at later times. However, in Case 3 where the relaxation of the transverse term is also included, the vortex can pass through the outflow boundary without any flow distortion. These results are consistent with those found in the conventional CFD simulations [34], verifying that the 2-D CBC can effectively enhance the accuracy and stability of the solution in the LBM simulations.

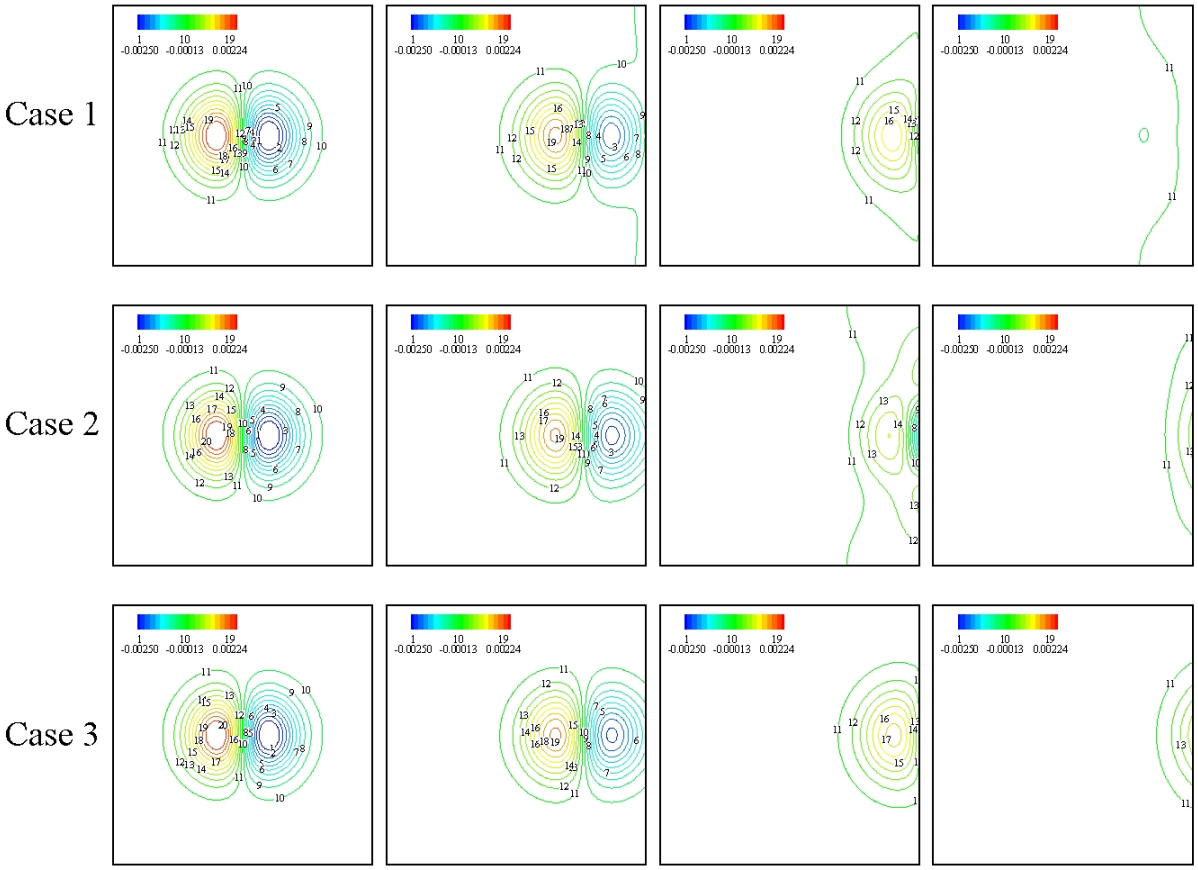

Figure 4.3: Isocontours of $y-$directional velocity v for Cases $1 \sim 3$ (from top to bottom) at $\widetilde{t} = 1$, 1801, 3601, and 4801 (from left to right).

4.3.2 Vortex shedding problem

The superiority of the improved CBC over the conventional CBC is also demonstrated by simulating a more complex flow induced by a vortex shedding around a square block. Three different cases with the three different CBC are investigated as in the previous test problem: Case 1 is the conventional LODI, Case 2 is the inclusion of the transverse term only, and Case 3 is the improved CBC with the relaxation of the transverse terms. Initially, a constant uniform flow u_∞ is imposed on the computational domain of $m = 200$ and $n = 200$. The square block is located at $\widetilde{x}_0 = 60$ and $\widetilde{y}_0 = 100$ with the side length of $R_c = 10$. The bounce back conditions are used at the solid boundaries. The specific parameters for the flow are chosen as a Mach number of $Ma = u_\infty/c_s = 0.087$, $c_s = \sqrt{\gamma RT} = \sqrt{1/3}$, and a Reynolds number of Re =100. As in the vortex-convection problem, $\sigma_1^{(x)} = 0.2$ and $a_1^{(x)} = Ma$ are used.

Fig. 4.4 shows the pressure isocontours of the flow around the square block for Cases $1 \sim 3$. It is readily observed from the figure that for Cases 1 and 2, significant pressure drift occurs whenever the vortices pass through the outflow boundary, which is similar to the results of the vortex-convection problem. For Case 3, however, the vortices can pass through the outflow boundary without spurious pressure change, verifying that the improved CBC with transverse relaxation should be adopted in the LBM to accurately simulate complex flows including turbulent flows as in the compressible CFD simulations [33, 34, 98, 107–109].

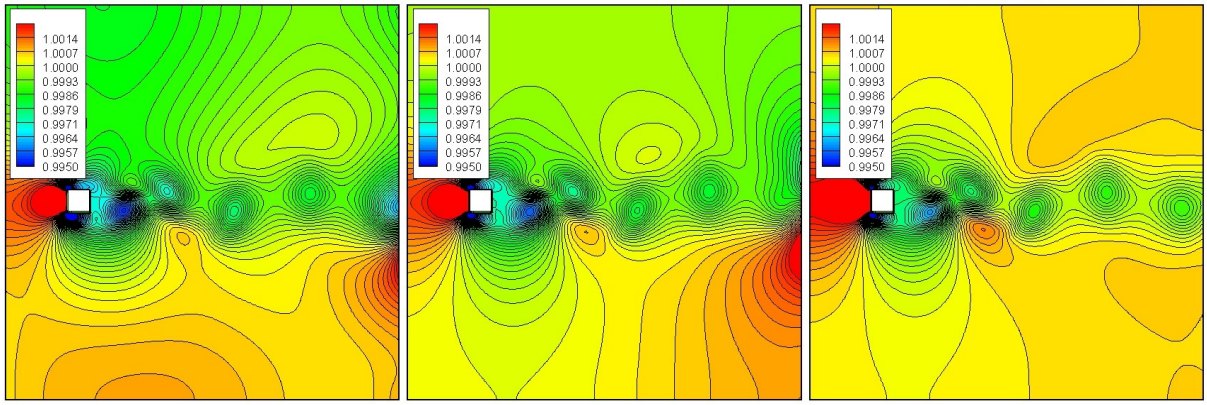

Figure 4.4: Isocontours of pressure p for Cases $1 \sim 3$ (from left to right) at $\widetilde{t} = 39001$.

4.4 Conclusion

The 2-D CBC with the proper relaxation of the transverse terms are formulated for the isothermal MRT–LBM and tested by simulating the vortex convection and vortex shedding problems. The test results show that the ignored transverse terms in the conventional CBC can deteriorate the solution behavior at the outflow boundary and the relaxation treatment of the transverse terms can resolve the problem. This verifies that the improved CBC should be applied to the LBM simulations with open boundaries.

Chapter V

Conclusions

In this study, three main objective have been accomplished: (a) to directly study Marangoni effects of surfactant through the interplay between the hydrodynamics potential and the adsorption by diffusion, (b) to propose a new approach for LBM maintaining colloidal particles within the drying droplet and (c) to verify the improved CBC applicable to the LBM simulations with open boundaries.

By studying the surfactant-induced Marangoni effect on droplet dynamics, we have successfully investigated deposition pattern forming process that occurs in the competition between evaporation induced 'coffee-ring' flows and surfactant-induced Marangoni flows. In this study, we develop a new lattice gas model, which is used a Monte Carlo method to find coupled dynamics of colloidal behavior and surfactant. The following is the summary of the important findings in the study of the surfactant-induced Marangoni effects on droplet dynamics.

- We divide the evolution of evaporation into several time regime during either Marangoni or coffee-ring effect is in turn dominant; (a) At the early time, the coffee ring effect is dominant. (b) At the later time, the Marangoni effect starts to influence particle motions.

- Colloidal particles similarly follow surfactant particle dynamics when it transport is mainly via convection (at slow adsorption rate for surfactant)

- Fast adsorption makes particle deposits more distributed, and high concentration

creates multi-ring patterns

- The oscillatory motion of particles is successfully captured under the certain condition of a droplet in evaporation; low contact angle and low surfactant concentration
- We explain the difference in the mechanism of the oscillatory and swirling motion, which has been roughly described in previous studies.

Using the pseudopotential LB model, we simulate the evaporation process of droplet with pinned contact line by setting the chemically patterned boundary condition of the substrate. We also propose an advection-diffusion equation to compute the behavior of colloidal particles within droplet. The conclusion of the study is summarized as follows.

- We propose the new LB model that recovers the advection-diffusion equation for colloidal particles, which is verified by Chapman-Enskog analysis.
- The force applied to the particles of the new LB model is treated in the same way as the force of the pseudopotential LB model.
- Since we consider the colloidal particles as the macroscopic fluid model, we solve the advection-diffusion equation for colloidal particles.

We have investigated the application of the improved characteristic boundary conditions to the Boltzmann lattice method. The following summarizes the conclusions of the studies.

- The ignored transverse terms in the conventional CBC can deteriorate the solution behavior at the outflow boundary. The relaxation treatment of the transverse terms that is in improved CBC can resolve this problem.
- Improved CBC can be applied to the multi-reflection boundary condition of LBM.
- This verified that the improved CBC should be applied to the LBM simulations with open boundaries; to validate by simulation of vortex convection and vortex shedding problem.

5.1 Future work

In this study, the velocity field inside the evaporating droplet was obtained by solving the Navier-Stokes equation from the previous study. This is a result obtained using the boundary conditions that fix the contact line, thus making it difficult to simulate the droplet with constant contact angle. Therefore, we are ultimately willing to simulate the particle behavior in a evaporating droplet by using both of the lattice Boltzmann method for velocity field, and the Monte-Carlo method for particle dynamics. It will make it possible to simulate the evaporating droplet under various conditions.

In addition, we perform the Monte-Carlo simulations in this study using axisymmetric assumptions in 2D schematics. This shows the limitation that it is difficult to accurately simulate the self-assembly of particles with axial variation. Therefore, we will extend the 2D coarse-grained lattice model to 3D in subsequent study. We will try to simulate the non-axisymmetric patterns such as unstable deposition patterns [20] and to provide a detailed insight about process of deposition patterns.

Moreover, we will improve the Langmuir's isotherm model to consider the particle-particle interaction. In present study, only advection and diffusion (particularly for surfactant) were considered when calculating Hamiltonian for particle behavior. However, in case of 'real' self-assembly of particles, the repulsive force between particles is inversely proportional to the their distance. At present, only the isotherm model including the solute-solvent interaction, such as the Frumkin's isotherm model [68], has been developed. In the future work, hence, we will develop an isotherm model including solvent-solvent interaction and use it to investigate the movement of particles.

References

[1] W. Han and Z. Lin, "Learning from "coffee rings": Ordered structures enabled by controlled evaporative self-assembly," *Angewandte Chemie International Edition*, vol. 51, no. 7, pp. 1534–1546, 2012.

[2] M. Singh, H. M. Haverinen, P. Dhagat, and G. E. Jabbour, "Inkjet printing-process and its applications," *Adv Mater*, vol. 22, pp. 673–85, 2010.

[3] T. Kawase, T. Shimoda, C. Newsome, H. STrringhaus, and R. H. Friend, "Inkjet printing of polymer thin film transistors," *Thin Solid Films*, vol. 438-439, pp. 279 – 287, 2003, the 5th International Conference on Nano-Molecular Electronics.

[4] D. B. Wolfe, J. C. Love, K. E. Paul, M. L. Chabinyc, and G. M. Whitesides, "Fabrication of palladium-based microelectronic devices by microcontact printing," *Applied Physics Letters*, vol. 80, no. 12, pp. 2222–2224, 2002.

[5] Y. Liu, T. Cui, and K. Varahramyan, "All-polymer capacitor fabricated with inkjet printing technique," *Solid-State Electronics*, vol. 47, no. 9, pp. 1543 – 1548, 2003.

[6] R. Nohria, R. K. Khillan, Y. Su, R. Dikshit, Y. Lvov, and K. Varahramyan, "Humidity sensor based on ultrathin polyaniline film deposited using layer-by-layer nano-assembly," *Sensors and Actuators B: Chemical*, vol. 114, no. 1, pp. 218 – 222, 2006.

[7] M. J. Heller, "Dna microarray technology: Devices, systems, and applications," *Annual Review of Biomedical Engineering*, vol. 4, no. 1, pp. 129–153, 2002, pMID: 12117754.

[8] R. D. Deegan, O. Bakajin, T. F. Dupont, G. Huber, S. R. Nagel, and T. A. Witten, "Capillary flow as the cause of ring stains from dried liquid drops," *Nature*, vol. 389, pp. 827–829, 1997.

[9] H. Hu and R. G. Larson, "Marangoni effect reverses coffee-ring depositions," *The Journal of Physical Chemistry B*, vol. 110, no. 14, pp. 7090–7094, 2006, pMID: 16599468.

[10] J. M. Stauber, S. K. Wilson, B. R. Duffy, and K. Sefiane, "On the lifetimes of evaporating droplets with related initial and receding contact angles," *Physics of Fluids*, vol. 27, no. 12, p. 122101, 2015.

[11] ——, "Evaporation of droplets on strongly hydrophobic substrates," *Langmuir*, vol. 31, no. 12, pp. 3653–3660, 2015, pMID: 25747121.

[12] J. Stauber, S. Wilson, B. Duffy, and K. Sefiane, "On the lifetimes of evaporating droplets," *Journal of Fluid Mechanics*, vol. 744, p. R2, 2014.

[13] P. J. Sáenz, A. W. Wray, Z. Che, O. K. Matar, P. Valluri, J. Kim, and K. Sefiane, "Dynamics and universal scaling law in geometrically-controlled sessile drop evaporation," *Nature Communications*, January 2017.

[14] T. Still, P. J. Yunker, and A. G. Yodh, "Surfactant-induced marangoni eddies alter the coffee-rings of evaporating colloidal drops," *Langmuir*, vol. 28, no. 11, pp. 4984–4988, 2012, pMID: 22369657.

[15] W.Sempels, R. dier, H.Mizuno, J.Hofkens, and J.Vermant, "Auto-production of biosurfactants reverses the coffee ring effect in a bacterial system," *Nature Communications*, vol. 4, p. 1757, 2013.

[16] W. Lenz, "Beiträge zum verständnis der magnetischen eigenschaften in festen körpern," *Physikalische Zeitschrift*, vol. 21, pp. 613 – 615, 1920.

[17] E. Ising, "Beitrag zur theorie des ferromagnetismus," *Zeitschrift für Physik*, vol. 31, no. 1, pp. 253–258, Feb 1925.

[18] L. Onsager, "Crystal statistics. i. a two-dimensional model with an order-disorder transition," *Phys. Rev.*, vol. 65, pp. 117–149, Feb 1944.

[19] E. Rabani, D. R. Reichman, P. L. Geissler, and L. E. Brus, "Drying-mediated self-assembly of nanoparticles," *Nature*, vol. 426, pp. 271–274, 2003.

[20] N. Jung, C. S. Yoo, and P. H. Leo, "Instability deposit patterns in an evaporating droplet," *The Journal of Physical Chemistry B*, vol. 118, no. 9, pp. 2535–2543, 2014, pMID: 24517080.

[21] C.-T. Hsu, C.-H. Chang, and S.-Y. Lin, "Comments on the adsorption isotherm and determination of adsorption kinetics," *Langmuir*, vol. 13, no. 23, pp. 6204–6210, 1997.

[22] Z. Guo, B. Shi, and N. Wang, "Lattice bgk model for incompressible navier–stokes equation," *Journal of Computational Physics*, vol. 165, no. 1, pp. 288 – 306, 2000.

[23] X. Shan and H. Chen, "Lattice boltzmann model for simulating flows with multiple phases and components," *Physical Review E*, vol. 47, pp. 1815–1819, 1993.

[24] A. Kupershtokh, D. Medvedev, and D. Karpov, "On equations of state in a lattice boltzmann method," *Computers and Mathematics with Applications*, vol. 58, no. 5, pp. 965 – 974, 2009, mesoscopic Methods in Engineering and Science.

[25] J. Zhang, "Lattice boltzmann method for microfluidics: models and applications," *Microfluidics and Nanofluidics*, vol. 10, no. 1, pp. 1–28, Jan 2011.

[26] R. Benzi, L. Biferale, M. Sbragaglia, S. Succi, and F. Toschi, "Mesoscopic modeling of a two-phase flow in the presence of boundaries: The contact angle," *Phys. Rev. E*, vol. 74, p. 021509, Aug 2006.

[27] C. K. Aidun and J. R. Clausen, "Lattice-boltzmann method for complex flows," *Annual Review of Fluid Mechanics*, vol. 42, no. 1, pp. 439–472, 2010.

[28] R. Ledesma-Aguilar, D. Vella, and J. M. Yeomans, "Lattice-boltzmann simulations of droplet evaporation," *Soft Matter*, vol. 10, pp. 8267–8275, 2014.

[29] I. Ginzburg and D. dHumières, "Multireflection boundary conditions for lattice Boltzmann models," *Phys. Rev. E*, vol. 68, no. 6, p. 066614, 2003.

[30] M. Junk and Z. Yang, "Asymptotic analysis of lattice Boltzmann boundary conditions," *J. Stat. Phys.*, vol. 121, no. 1-2, pp. 3–35, 2005.

[31] S. Izquierdo, P. Martínez-Lera, and N. Fueyo, "Analysis of open boundary effects in unsteady lattice Boltzmann simulations," *Comput. Math. Appl.*, vol. 58, no. 5, pp. 914–921, 2009.

[32] S. Izquierdo and N. Fueyo, "Characteristic nonreflecting boundary conditions for open boundaries in lattice Boltzmann methods," *Phys. Rev. E*, vol. 78, no. 4, p. 046707, 2008.

[33] C. S. Yoo, Y. Wang, A. Trouvé, and H. G. Im, "Characteristic boundary conditions for direct simulations of turbulent counterflow flames," *Combust. Theory Model.*, vol. 9, no. 4, pp. 617–646, 2005.

[34] C. S. Yoo and H. G. Im, "Characteristic boundary conditions for simulations of compressible reacting flows with multi-dimensional, viscous and reaction effects," *Combust. Theory Model.*, vol. 11, no. 2, pp. 259–286, 2007.

[35] H. Hu and R. G. Larson, "Analysis of the microfluid flow in an evaporating sessile droplet," *Langmuir*, vol. 21, no. 9, pp. 3963–3971, 2005, pMID: 15835962.

[36] ——, "Analysis of the effects of marangoni stresses on the microflow in an evaporating sessile droplet," *Langmuir*, vol. 21, no. 9, pp. 3972–3980, 2005, pMID: 15835963.

[37] K. Zhang, L. Ma, X. Xu, J. Luo, and D. Guo, "Temperature distribution along the surface of evaporating droplets," *Phys. Rev. E*, vol. 89, p. 032404, Mar 2014.

[38] X. Xu, J. Luo, and D. Guo, "Radial-velocity profile along the surface of evaporating liquid droplets," *Soft Matter*, vol. 8, pp. 5797–5803, 2012.

[39] ——, "Criterion for reversal of thermal marangoni flow in drying drops," *Langmuir*, vol. 26, no. 3, pp. 1918–1922, 2010, pMID: 19761263.

[40] X. Xu and J. Luo, "Marangoni flow in an evaporating water droplet," *Applied Physics Letters*, vol. 91, no. 12, p. 124102, 2007.

[41] T. Kajiya, W. Kobayashi, T. Okuzono, and M. Doi, "Controlling the drying and film formation processes of polymer solution droplets with addition of small amount of surfactants," *The Journal of Physical Chemistry B*, vol. 113, no. 47, pp. 15 460–15 466, 2009, pMID: 19921951.

[42] S. Parsa, M. Gupta, F. Loizeau, and K. C. Cheung, "Effects of surfactant and gentle agitation on inkjet dispensing of living cells," *Biofabrication*, vol. 2, no. 2, p. 025003, 2010.

[43] P. J. Yunker, T. Still, M. A. Lohr, and A. G. Yodh, "Suppression of the coffee-ring effect by shape-dependent capillary interactions," *Nature*, vol. 476, pp. 308–311, 2011.

[44] M. Anyfantakis, Z. Geng, M. Morel, S. Rudiuk, and D. Baigl, "Modulation of the coffee-ring effect in particle/surfactant mixtures: the importance of particle–interface interactions," *Langmuir*, vol. 31, no. 14, pp. 4113–4120, 2015, pMID: 25797472.

[45] R. D. Deegan, "Pattern formation in drying drops," *Phys. Rev. E*, vol. 61, pp. 475–485, Jan 2000.

[46] I. U. Vakarelski, D. Y. C. Chan, T. Nonoguchi, H. Shinto, and K. Higashitani, "Assembly of gold nanoparticles into microwire networks induced by drying liquid bridges," *Phys. Rev. Lett.*, vol. 102, p. 058303, Feb 2009.

[47] C.-H. Liu and X. Yu, "Silver nanowire-based transparent, flexible, and conductive thin film," *Nanoscale Research Letters*, vol. 6, no. 1, p. 75, Jan 2011.

[48] C. Girotto, D. Moia, B. P. Rand, and P. Heremans, "High-performance organic solar cells with spray-coated hole-transport and active layers," *Advanced Functional Materials*, vol. 21, no. 1, pp. 64–72, 2011.

[49] A. Crivoi and F. Duan, "Elimination of the coffee-ring effect by promoting particle adsorption and long-range interaction," *Langmuir*, vol. 29, no. 39, pp. 12 067–12 074, 2013, pMID: 24015843.

[50] N. Jung, H. W. Seo, P. H. Leo, J. Kim, P. Kim, and C. S. Yoo, "Surfactant effects on droplet dynamics and deposition patterns: a lattice gas model," *Soft Matter*, vol. 13, pp. 6529–6541, 2017.

[51] C. Seo, D. Jang, J. Chae, and S. Shin, "Altering the coffee-ring effect by adding a surfactant-like viscous polymer solution," *Sci. Rep.*, vol. 7, p. 500, 2017.

[52] A. Askounis, K. Sefiane, V. Koutsos, and M. E. Shanahan, "The effect of evaporation kinetics on nanoparticle structuring within contact line deposits of volatile drops," *Colloids and Surfaces A: Physicochemical and Engineering Aspects*, vol. 441, pp. 855 – 866, 2014.

[53] J. Huang and G. Liu, "Monte Carlo Simulation on the Assembly of Nanorods with Anisotropic Interactions," *The Journal of Physical Chemistry C*, vol. 115, no. 13, pp. 5385–5391, 2011.

[54] V. X. Nguyen and K. J. Stebe, "Patterning of small particles by a surfactant-enhanced Marangoni-Bénard instability," *Physical Review Letters*, vol. 88, no. 16, p. 164501, 2002.

[55] A. Marin, R. Liepelt, M. Rossi, and C. J. Kähler, "Surfactant-driven flow transitions in evaporating droplets," *Soft Matter*, vol. 12, no. 5, pp. 1593–1600, 2016.

[56] A. Crivoi and F. Duan, "Three-dimensional monte carlo model of the coffee-ring effect in evaporating colloidal droplets," *Scientific Reports*, vol. 4, p. 4310, 2014.

[57] N. I. Lebovka, N. V. Vygornitskii, V. A. Gigiberiya, and Y. Y. Tarasevich, "Monte carlo simulation of evaporation-driven self-assembly in suspensions of colloidal rods," *Physical Review E*, vol. 94, no. 6, p. 062803, 2016.

[58] Y. J. Carreón, J. González-Gutiérrez, M. Pérez-Camacho, and H. Mercado-Uribe, "Patterns produced by dried droplets of protein binary mixtures suspended in water," *Colloids and Surfaces B: Biointerfaces*, vol. 161, pp. 103 – 110, 2018.

[59] O. Kletenik-Edelman, E. Ploshnik, A. Salant, R. Shenhar, U. Banin, and E. Rabani, "Drying-mediated hierarchical self-assembly of nanoparticles: A dynamical coarse-grained approach," *The Journal of Physical Chemistry C*, vol. 112, no. 12, pp. 4498–4506, 2008.

[60] Á. G. Marín, H. Gelderblom, D. Lohse, and J. H. Snoeijer, "Rush-hour in evaporating coffee drops," *Physics of Fluids*, vol. 23, no. 9, p. 091111, 2011.

[61] J. R. Trantum, Z. E. Eagleton, C. A. Patil, J. M. Tucker-Schwartz, M. L. Baglia, M. C. Skala, and F. R. Haselton, "Cross-sectional tracking of particle motion in evaporating drops: Flow fields and interfacial accumulation," *Langmuir*, vol. 29, no. 21, pp. 6221–6231, 2013.

[62] J. R. Trantum, M. L. Baglia, Z. E. Eagleton, R. L. Mernaugh, and F. R. Haselton, "Biosensor design based on Marangoni flow in an evaporating drop," *Lab on a Chip*, vol. 14, no. 2, pp. 315–324, 2014.

[63] N. Anantharaju, M. Panchagnula, and S. Neti, "Evaporating drops on patterned surfaces: Transition from pinned to moving triple line," *Journal of Colloid and Interface Science*, vol. 337, no. 1, pp. 176–182, 2009.

[64] P. De Gennes, "Wetting: Statics and dynamics," *Reviews of Modern Physics*, vol. 57, no. 3, pp. 827–863, 1985, cited By 4280.

[65] G. Nadkarni and S. Garoff, "An investigation of microscopic aspects of contact angle hysteresis: Pinning of the contact line on a single defect," *EPL (Europhysics Letters)*, vol. 20, no. 6, p. 523, 1992.

[66] R. E. Johnson Jr and R. H. Dettre, "Contact angle hysteresis. III. Study of an idealized heterogeneous surface," *The Journal of Physical Chemistry*, vol. 68, no. 7, pp. 1744–1750, 1964.

[67] J. Eastoe and J. Dalton, "Dynamic surface tension and adsorption mechanisms of surfactants at the air–water interface," *Advances in Colloid and Interface Science*, vol. 85, no. 2, pp. 103 – 144, 2000.

[68] V. L. Kolev, K. D. Danov, P. A. Kralchevsky, G. Broze, and A. Mehreteab, "Comparison of the van der waals and frumkin adsorption isotherms for sodium dodecyl sulfate at various salt concentrations," *Langmuir*, vol. 18, no. 23, pp. 9106–9109, 2002.

[69] Y. O. Popov, "Remobilizing surfactant retarded fluid particle interfaces. i. stress-free conditions at the interfaces of micellar solutions of surfactants with fast sorption kinetics," *Physical Review E*, vol. 71, p. 036313, 2005.

[70] H. Hu and R. G. Larson, "Evaporation of a sessile droplet on a substrate," *The Journal of Physical Chemistry B*, vol. 106, no. 6, pp. 1334–1344, 2002.

[71] A. Bonfillon, F. Sicoli, and D. Langevin, "Dynamic surface tension of ionic surfactant solutions," *Journal of Colloid and Interface Science*, vol. 168, no. 2, pp. 497 – 504, 1994.

[72] N. J. Alvarez, D. R. Vogus, L. M. Walker, and S. L. Anna, "Using bulk convection in a microtensiometer to approach kinetic-limited surfactant dynamics at fluid-fluid interfaces," *Journal of colloid and interface science*, vol. 372, no. 1, p. 183—191, April 2012.

[73] A. F. H. Ward and L. Tordai, "Time-dependence of boundary tensions of solutions i. the role of diffusion in time-effects," *The Journal of Chemical Physics*, vol. 14, no. 7, pp. 453–461, 1946.

[74] A. J. Prosser and E. I. Franses, "Modeling of equilibrium adsorption and surface tension of cationic gemini surfactants," *Journal of Colloid and Interface Science*, vol. 240, no. 2, pp. 590 – 600, 2001.

[75] H. Diamant and D. Andelman, "Kinetics of surfactant adsorption at fluid-fluid interfaces," *The Journal of Physical Chemistry*, vol. 100, no. 32, pp. 13 732–13 742, 1996.

[76] H. Diamant, G. Ariel, and D. Andelman, "Kinetics of surfactant adsorption: the free energy approach," *Colloids and Surfaces A: Physicochemical and Engineering Aspects*, vol. 183-185, pp. 259 – 276, 2001.

[77] Y. Hamamoto, J. R. E. Christy, and K. Sefiane, "Order-of-magnitude increase in flow velocity driven by mass conservation during the evaporation of sessile drops," *Phys. Rev. E*, vol. 83, p. 051602, May 2011.

[78] J. R. E. Christy, Y. Hamamoto, and K. Sefiane, "Flow transition within an evaporating binary mixture sessile drop," *Phys. Rev. Lett.*, vol. 106, p. 205701, May 2011.

[79] V. N. Truskett and K. J. Stebe, "Influence of surfactants on an evaporating drop: fluorescence images and particle deposition patterns," *Langmuir*, vol. 19, no. 20, pp. 8271–8279, 2003.

[80] T. Furuta, M. Sakai, T. Isobe, and A. Nakajima, "Evaporation behavior of microliter- and sub-nanoliter-scale water droplets on two different fluoroalkylsilane coatings," *Langmuir*, vol. 25, pp. 11 998–2001, 2009.

[81] J. Chen, W. S. Liao, X. Chen, T. Yang, S. E. Wark, D. H. Son, J. D. Batteas, and P. S. Cremer, "Evaporation-induced assembly of quantum dots into nanorings," *ACS Nano*, vol. 3, pp. 173–80, 2009.

[82] T. P. Bigioni, X. M. Lin, T. T. Nguyen, E. I. Corwin, T. A. Witten, and H. M. Jaeger, "Kinetically driven self assembly of highly ordered nanoparticle monolayers," *Nat Mater*, vol. 5, pp. 265–70, 2006.

[83] K. L. Maki and S. Kumar, "Fast evaporation of spreading droplets of colloidal suspensions," *Langmuir*, vol. 27, pp. 11 347–63, 2011.

[84] M. Zhao and X. Yong, "Modeling evaporation and particle assembly in colloidal droplets," *Langmuir*, vol. 33, pp. 5734–5744, 2017.

[85] S. Frijters, F. Günther, and J. Harting, "Effects of nanoparticles and surfactant on droplets in shear flow," *Soft Matter*, vol. 8, 2012.

[86] X. Shan and G. Doolen, "Multicomponent lattice-boltzmann model with interparticle interaction," *Journal of Statistical Physics*, vol. 81, pp. 379–393, 1995.

[87] V. K. Michalis, A. N. Kalarakis, E. D. Skouras, and V. N. Burganos, "Mesoscopic modeling of flow and dispersion phenomena in fractured solids," *Computers and Mathematics With Applications*, vol. 55, pp. 1525–1540, 2008.

[88] Kruger, *The Lattice Boltzmann Method*. Springer, 2017.

[89] Z. Guo, C. Zheng, and B. Shi, "Discrete lattice effects on the forcing term in the lattice boltzmann method," *Phys. Rev. E*, vol. 65, p. 046308, Apr 2002.

[90] B. Chopard, J. L. Falcone, and J. Latt, "The lattice boltzmann advection-diffusion model revisited," *The European Physical Journal Special Topics*, vol. 171, no. 1, pp. 245–249, Apr 2009.

[91] D. Hessling, Q. Q. Xie, J. J. Harting, and J. J. Harting, "Diffusion dominated evaporation in multicomponent lattice boltzmann simulations," *Journal of Chemical Physics*, vol. 146, p. 054111, 2017.

[92] X. Shan, "Analysis and reduction of the spurious current in a class of multiphase lattice boltzmann models," *Phys Rev E Stat Nonlin Soft Matter Phys*, vol. 73, p. 047701, 2006.

[93] K. Connington and T. Lee, "A review of spurious currents in the lattice boltzmann method for multiphase flows," *Journal of Mechanical Science and Technology*, vol. 26, pp. 3857–3863, 2013.

[94] T. J. Poinsot and S. K. Lele, "Boundary conditions for direct simulations of compressible viscous flows," *J. Comput. Phys.*, vol. 101, no. 1, pp. 104–129, 1992.

[95] K. W. Thompson, "Time dependent boundary conditions for hyperbolic systems," *J. Comput. Phys.*, vol. 68, no. 1, pp. 1–24, 1987.

[96] ——, "Time-dependent boundary conditions for hyperbolic systems, II," *J. Comput. Phys.*, vol. 89, no. 2, pp. 439–461, 1990.

[97] J. C. Sutherland and C. A. Kennedy, "Improved boundary conditions for viscous, reacting, compressible flows," *J. Comput. Phys.*, vol. 191, no. 2, pp. 502–524, 2003.

[98] G. Lodato, P. Domingo, and L. Vervisch, "Three-dimensional boundary conditions for direct and large-eddy simulation of compressible viscous flows," *J. Comput. Phys.*, vol. 227, no. 10, pp. 5105–5143, 2008.

[99] D. Heubes, A. Bartel, and M. Ehrhardt, "Characteristic boundary conditions in the lattice Boltzmann method for fluid and gas dynamics," *J. Comput. Appl. Math.*, vol. 262, pp. 51–61, 2014.

[100] J.-P. Berenger, "A perfectly matched layer for the absorption of electromagnetic waves," *J. Comput. Phys.*, vol. 114, no. 2, pp. 185–200, 1994.

[101] F. Q. Hu, X. Li, and D. Lin, "Absorbing boundary conditions for nonlinear Euler and Navier–Stokes equations based on the perfectly matched layer technique," *J. Comput. Phys.*, vol. 227, no. 9, pp. 4398–4424, 2008.

[102] F. Q. Hu, "Development of PML absorbing boundary conditions for computational aeroacoustics: A progress review," *Comput. Fluids*, vol. 37, no. 4, pp. 336–348, 2008.

[103] A. Najafi-Yazdi and L. Mongeau, "An absorbing boundary condition for the lattice Boltzmann method based on the perfectly matched layer," *Comput. Fluids*, vol. 68, pp. 203–218, 2012.

[104] E. Bécache, S. Fauqueux, and P. Joly, "Stability of perfectly matched layers, group velocities and anisotropic waves," *J. Comput. Phys.*, vol. 188, no. 2, pp. 399–433, 2003.

[105] S. J. B. Stoll, "Lattice Boltzmann Simulation of Acoustic Fields with Special Attention to Non-reflecting Boundary Conditions," Master's thesis, Institutt for elektronikk og telekommunikasjon, 2014.

[106] P. Lallemand and L.-S. Luo, "Theory of the lattice Boltzmann method: Dispersion, dissipation, isotropy, Galilean invariance, and stability," *Phys. Rev. E*, vol. 61, no. 6, p. 6546, 2000.

[107] C. S. Yoo, R. Sankarna, and J. H. Chen, "Three-dimensional direct numerical simulation of a turbulent lifted hydrogen jet flame: flame stabilization and structure," *J. Fluid Mech.*, vol. 640, pp. 453–481, 2009.

[108] C. S. Yoo, E. S. Richardson, R. Sankaran, and J. H. Chen, "A DNS study on the stabilization mechanism of a turbulent lifted ethylene jet flame in highly-heated coflow," *Proc. Combust. Inst.*, vol. 33, pp. 1619–1627, 2011.

[109] R. W. Grout, A. Gruber, C. S. Yoo, and J. H. Chen, "Direct numerical simulation of flame stabilization downstream of a transverse fuel jet," *Proc. Combust. Inst.*, vol. 33, pp. 1629–1637, 2011.

Acknowledgements

I would like to express my special thanks to Dr. Chun Sang Yoo, an advisor, for valuable counsel and inspiration in my doctoral program. I sincerely respected to the his insightful advices on my research and tried to be an independent researcher as like him. I also thank to my doctoral committee members - Sung Youb Kim, Taesung Kim, Jaesung Jang and Pilwon Kim, for their valuable comments on my thesis.

I am always grateful to my family for believing and supporting me and also appreciate to my group members at the Combustion and Propulsion Laboratory for their ongoing support and valuable discussion. I am motivated by the enthusiasm of group member toward research, which was a great help in successfully completing the ph.D course.

This work was supported by BK21Plus funded by the Ministry of Education and by Basic Science Research Program through the National Research Foundation of Korea (NRF) funded by the Ministry of Science.